UNIVERSITÀ DELLA CALABRIA

UNIVERSITA' DELLA CALABRIA

Dipartimento di FISICA

Scuola di Dottorato

"ARCHIMEDE" in SCIENZE, COMUNICAZIONE E TECNOLOGIE

Indirizzo

FISICA E TECNOLOGIE QUANTISTICHE

CICLO

XXV

TITOLO TESI

A phenomenological model for the DVCS process

Settore Scientifico Disciplinare FIS/04

Direttore: Ch.mo Prof. Pietro Pantano

Firma Pietro Pantano

Supervisore: Ch.mo Prof. Roberto Fiore

Firma Roberto Fiore

Dottorando: Dott. Giacinto Ciappetta

Firma Giacinto Ciappetta

Università degli Studi della Calabria

facoltà di scienze matematiche, fisiche e naturali

Dottorato di Ricerca in
Fisica e Tecnologie Quantistiche

A phenomenological model for the DVCS process

Supervisore
Prof. Roberto Fiore

Candidato
Giacinto Ciappetta

Direttore della Scuola
Prof. Pietro Pantano

Scuola Archimede - XXV Ciclo

to my parents . . .

and to streets to pursue . . .

Contents

Introduction

Over the past two decades, the high-energy scattering processes have attracted the attention of the scientific community, due to the fact that their study may be useful to investigate the nature of strong interactions, examined by the experimental data collected at the collider HERA (located in Hamburg, Germany, in the DESY, Deutsches Elektronen Synchrotron, laboratory) and Tevraton (located in Batavia, United States of America, at the Fermi National Accelerator Laboratory). In particular, the study of the processes of diffraction allows to investigate the transition between the 'soft' regime, characterized by an energy scale of the order of magnitude hadronic $R_B\,(\sim 1\,\mathrm{fm})$, and the 'hard' regime, characterized also by one or more energy scales 'hard' that allow the application of the 'perturbative Quantum Chromodynamics' (pQCD), used in the study of strong interactions.

The distinction between soft and hard processes is not completely unambiguous and it is not easy to say whether a given process is soft or hard. However, it is thought that such diversification is necessary because it is believed that characterize a well-defined type of phenomena in the context of one of the two schemes give the possibility to apply the correct theoretical framework. But the physics behind the diffractive processes should be the same; by this basic principle, the present work was performed.

Among the scattering phenomena, there are processes of electron-proton (ep) scattering where the exchange of a virtual photon γ^* takes place between the colliding electron and the proton. The virtual photon is characterized by the so-called virtuality Q^2, equal to opposite of the square of four-momentum transferred to the lepton vertex. The diffractive scattering is a particular process by which particles in the final state have spread to very small angles. The processes

of production of vector mesons (VMP), which can generally be distinguished in photoproduction ($Q^2 \approx 0$) and in electroproduction ($Q^2 > 0$), belong to the category of diffractive events. A process of particular interest is the Deeply Virtual Compton scattering (DVCS), $ep \longrightarrow e\gamma p$.

Assumed the Parton Model for the hadrons, according to pQCD, for the DVCS the partons, making up the proton, interact with the incoming (virtual) and outgoing (real) photons; these partons have different longitudinal four-momentum and transverse, as a consequence of the difference in mass between the virtual photon and the real. This difference may be interpreted in the context of Distributions Generalized Parton (GPD) or of Colour Dipole Models. The Parton distribution functions (PDF), extracted from deeply inelastic (DIS) processes, do not contain any information about the correlation between partons and about their motion transverse to the direction along which the collision occur; conversely, the GPD functions provide this information. Therefore, the analysis of the DVCS process may be used to investigate the formalism of the GPDs, since the amplitude of $\gamma^* p \longrightarrow \gamma p$ is proportional to the GPDs.

The purpose of this work is the study of the DVCS. In particular, we will perform an analysis of much of the collected data and we will suggest a new phenomenological model describing the examined process.

The work is organized into four Chapters.

- In the first chapter we describe the diffractive processes in their generality and we present some of the most interesting features of the DVCS process.
- In the second chapter we report various data collected by the H1 and ZEUS Collaborations in their experiments. We show the techniques used for the data 'rescaling'. In particular, we suggest a new procedure to rescale the experimental data by which we infer a form 'normal' of the DVCS cross section.
- In the third chapter, starting from the analysis conducted in the previous, we lay the foundations to build a new phenomenological model for the DVCS process.

- In the fourth chapter we present, in its essential form, the new model and we compare it with the experimental data.

In order to facilitate the understanding of the issues raised, we have included three Appendices, which facilitate the description of the physical aspects treated.

Chapter 1

The DVCS process

In this chapter we briefly show some of the features more interesting of the *Deeply Virtual Compton Scattering* (*DVCS*). We give certain details also for the so-called 'Diffractive Scattering', traditionally studied in interactions hadron-hadron and well described in framework of the Regge Theory [1]. The diffractive scattering may also be studied in the virtual photon-hadron processes. Indeed, for low values of the square of the four-momentum transferred and high energies in CM (center mass) of virtual photon-proton system, i.e. for low values of x, the virtual photon behaves like a hadron which fluctuates in a $q\bar{q}$ couple; therefore the interaction $\gamma^* p$ may be seen as between two hadrons (see Figure 1.4).

The investigation of the diffractive scattering is connected with the study of structure functions of the proton in the kinematic region of small values of Bjorken variable[1] x and may shed light on the theory of strong interactions in the transition region between perturbative and non-perturbative regime.

1.1 Diffractive Scattering

The hadronic processes may be divided into two distinct classes of phenomena: *soft* and *hard*. Although for the latter the high value of the transferred four-momentum permits to use the pQCD, part of the process have no perturbative origin. This component is inherent in the functions of distribution of quarks and gluons into hadrons, the so-called Parton Distribution Functions (*PDF*).

[1] See Appendix B.

However, the 'factorization theorem' [2, 3] provides that, in scattering amplitude, the short-range effects, calculable in pQCD, can be separated from the non-perturbative effects at large radius, which are expressed by the PDF, i.e. the perturbative part of scattering amplitude may be separated from that non-perturbative. The latter is universal and can be extracted by analyzing a hadronic scattering process and used to study other processes.

The *soft* processes are characterized by a scale of energies of the order of magnitude hadronic R_B ($\sim 1\,\text{fm}$). The square of the four-momentum transferred to the proton vertex, t, is generally small, $|t| \sim 1/R_B^2 \sim$ (a few hundred MeV)^2, and the cross section shows an exponential dependence on t, $d\sigma/dt \sim e^{-R_B^2|t|}$, while the events at large $|t|$ are highly suppressed. A great value for the size of hadronic R_B makes these phenomena intrinsically non-perturbative, so the pQCD is not adequate to describe them. Since the '60s the approach used to describe the soft processes is the Regge theory. According to this theory [2, pag. 1], the hadronic soft phenomena at high energies are generally dominated by the exchange of an enigmatic object, the Pomeron, that we will discuss in section 1.3.

The hadronic diffraction belongs to class of soft processes. In the last few years, diffractive processes, with soft and hard properties at the same time, have been investigated. The Deeply Diffractive Inelastic Scattering ($DDIS$) is a characteristic process of this type. It is a deeply inelastic scattering which in the final state is characterized by a large rapidity $\tilde{\eta}$ between the outgoing proton and the particles produced in the hadronization of photon[2].

1.2 Short digression on diffraction

The term 'diffraction' in classical physics indicates the optical phenomenon that we observe when a light beam encounters an obstacle, or passes through a hole, whose dimensions are comparable to the wavelength of the beam. When light of wavelength λ invests an opaque disc of radius R_B on a far screen, it is produced a diffraction pattern characterized by interference fringes (see Figure 1.1): it is observed a peak intensity of the diffused beam in the *forward* direction, i.e. at an angle of diffusion $\theta = 0$, called 'diffractive peak', and a series, symmetrical with

[2]For a definition of $\tilde{\eta}$, see the section 1.3.

respect to the diffractive peak, of secondary peaks which alternate with intensity minima; the first minimum is found at an angle of diffusion $\theta_{min} \simeq \pm\,\lambda/(2R_B)$.

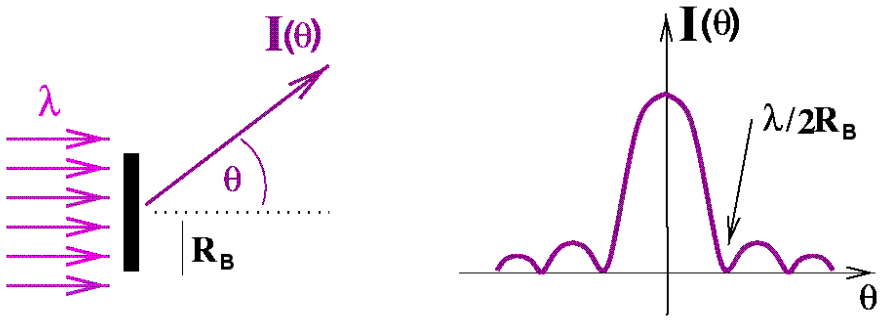

Figure 1.1: The intensity distribution I of a light beam having a wavelength λ, in case of diffraction by an opaque disc of radius R_B.

The intensity of the diffracted light, as function on the angle of diffusion, at small angles and large wave numbers $k = (2\pi)/\lambda$ is given by

$$\frac{I(\theta)}{I(\theta=0)} = \frac{\left[2J_1(\zeta)\right]^2}{\zeta^2} \simeq 1 - \frac{R_B^2}{4}\,(k\theta)^2\,, \tag{1.1}$$

where J_1 is the first order Bessel function, $\zeta = kR_B \sin\theta \simeq qR_B$, $q \simeq k\theta$ is the transferred four-momentun and R_B is the radius of target.

Since the 50s of the last century, the term 'diffraction' is used for the hadronic processes which exhibit similar behavior to the optical diffraction described above; these processes are then called 'diffractive'. The differential cross section $d\sigma/dt$ for the proton-proton elastic scattering, $pp \longrightarrow pp$, decreasing for small values of $|t|$, presents a trend similar to the diffraction pattern described above, as shown by Figure 1.2, extracted from reference [5]. The figure shows experimental values of $d\sigma/dt$ obtained at different values of four-momentum of the incoming proton in various fixed-target experiments.

At low values of $|t|$ the differential cross section, as a function of θ, may be written as [2, 6]

$$\frac{d\sigma}{dt} = \left.\frac{d\sigma}{dt}\right|_{t=0} e^{-B|t|} \simeq \left.\frac{d\sigma}{dt}\right|_{t=0} \left[1 - B(p\theta)^2\right]\,, \tag{1.2}$$

where the absolute value of the square of the four-momentum transferred from incident hadron to scattered hadron is $|t| \simeq (p\theta)^2$; p is the four-momentum of the

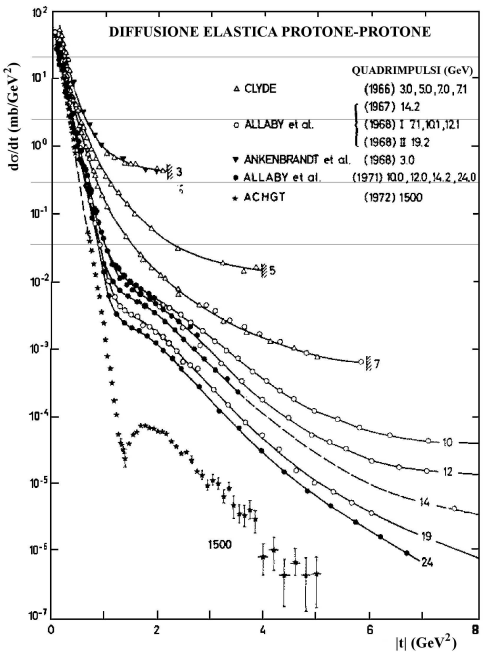

Figure 1.2: Differential cross section for elastic scattering pp as a function of the square of transferred four-momentum . The four-momentum of the incoming proton (fixed-target experiment) is reported for each curve. With the growth of the energy, a classical diffraction pattern appears, as for the optical diffraction. The Figure is extracted from reference [5].

incident proton. The parameter B is proportional to the square of the radius of the target,$B = R_B^2/4$, where R_B is to be understood more precisely the transverse distance between projectile and target. Other secondary maxima appear for higher values of $|t|$. Therefore, by making a comparison between the Eq. (3.1) and Eq. (1.1), as also between the Figure 1.2 and Figure 1.1, it is clear why we use the term 'diffraction' for the elastic scattering pp. Similar distributions of $d\sigma/dt$ were also observed for other processes (such as protons and pions incident on helium [7, page 5]), and this justifies the use of the diffraction term for this type of processes. Despite this similarity is evident, in the case of hadronic diffraction, by increasing the energy, it is observed a *forward shrinkage of the peak diffractive* (see Figure 1.2), which does not result in the case of optical diffraction [2, page 4].

Although the hadron physics and optics are applied on fields that might seem very far apart, it is clear that in both cases we are dealing with high wave numbers and that in both cases the wavelike character of the process determines what we observe experimentally.

1.3 Hadronic Diffraction

In the hadron-hadron scattering, a good fraction of the total cross section is due to diffractive processes; in particular the DDIS processes, first observed at $HERA$, account for about 10% of the total events of DIS processes[3].

Diffractive interactions were first observed in the elastic scattering between hadrons [13], as $A + B \longrightarrow A + B$ (see Figure 1.3 "a")), by starting from the proton-proton elastic scattering. Then the diffractive phenomena were also examined in other processes where at least one dissociation occurred [8, 10]. In the 'single diffractive dissociation', one of the incident particles is located in the final state practically intact while the second gives rise to a group of particles, indicated by X, or a resonance (Figure 1.3 "b"); in the 'doubly diffractive dissociation', both incident particles give rise to a group of particles, indicated by X and Y (Figure 1.3 "c"). The states of the final particles have the same quantum numbers of the initial hadrons which generate them. In all cases, the energy of the outgoing hadrons A and B, or of the states X and Y, is approximately equal to that of the incident particle beam.

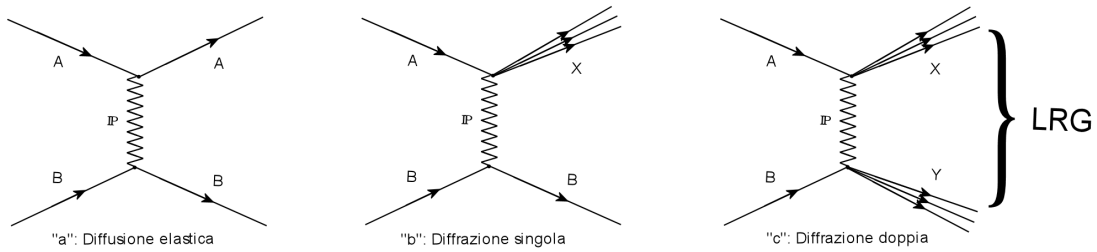

Figure 1.3: Elastic scattering, single diffractive dissociation and double diffractive dissociation, in the collision of two hadrons A and B. The two groups of particles in the final state are separated by a large gap in rapidity (LRG). The zigzag lines denote the exchange of a Pomeron ($I\!P$) in the t channel.

A doubly diffractive reaction is characterized[4] by a 'Large Rapidity Gap' (LRG) between the two groups of particles X and Y, i.e. these groups are well

[3] In general, at HERA the hard diffraction accounted for a fraction of the order 10% on the total cross section; at the Tevatron collider the hard diffraction accounted only about 1% [8, 9, 10, 11, 12]

[4] The rapidity of a particle with energy E and longitudinal four-momentum $p_\parallel$ is defined as $\tilde{\eta} = \frac{1}{2} \ln \frac{E+p_\parallel}{E-p_\parallel}$ and it may be approximated by the pseudorapidity $\eta = -\ln \tan \frac{\theta}{2}$, when the mass of particle is small and $\cos\theta = p_\parallel / E$. The rapidity is a measure of the velocity of particle along the direction of the incoming proton.

separated according to the polar angle θ, measured with respect to the direction of the incoming proton, which is the 'forward' direction. The LRG is the result of a small transverse four-momentum exchange between the incoming particles; so, in the final state, the particles move with four-momenta very similar to those of the initial states. Despite this, phenomena can occur which are not diffractive, although showing a significant LRG. It is expected that the number $N_{\rm nd}$ of these events, compared to those properly diffractive $N_{\rm d}$, is exponentially suppressed [2], i.e. the distribution of not diffractive events is

$$\frac{dN_{\rm nd}}{d\Delta\tilde{\eta}} \sim e^{-\Delta\tilde{\eta}}\,, \tag{1.3}$$

while that of diffractive events is

$$\frac{dN_{\rm d}}{d\Delta\tilde{\eta}} \sim \text{constant}\,, \tag{1.4}$$

where $\Delta\tilde{\eta}$ denotes the gap in rapidity in the final state. Therefore the diffractive processes can be distinguished from those not properly diffractive only asymptotically, because the latters decrease in number with the energy, as determined by Eq. (1.3).

So far there is no model that correctly describes all aspects of diffractive processes. These reactions, as we have already mentioned, belong to the class of processes, called soft, which are mainly described only by phenomenological models. One of these models is based on the phenomenological Regge theory [1] and it is widely used for comparing its predictions with measurements in diffractive physics.

The Regge Theory[5] describes the high energy diffractive scattering in terms of exchange of 'objects' (not particles), called *Reggeons*. The *Reggeon* is equivalent to a superposition of particles (mesons and baryons) with the same quantum numbers, except the spin. By plotting the spin of the particles as a function of the square of mass, the particles corresponding to a specific Reggeon lie on a line called 'Regge trajectory' [14]. This theory has allowed to obtain reliable predictions for the elastic cross section, which initially decreases with the increase of energy $\sqrt{s}$ of the center of mass, whereas, after a flat phase, it slightly increases. The initial decrease may be described by the trajectory of a Reggeon, while growth

[5]Overview of the Regge Theory is in Appendix C.

may be described by a new trajectory, said *Pomeron* ($I\!P$) [15]. The growth of the cross section was predicted by Pomeranchuk [16] and the trajectory was named in his honor. The Pomeron has the quantum numbers of the vacuum and is generally thought of as the mediator in the diffractive scattering.

In case of a single diffraction process, when the energy $\sqrt{s}$ in the CM is bigger than the invariant mass M_X (as defined in subsection 1.5) of the final system X, the particle B shows the longitudinal four-momentum almost unchanged and its rapidity gap by the system X is large, resulting $\Delta\tilde{\eta} \sim \ln(s/M_X^2)$. The Regge Theory describes this process as being due to the exchange of a Pomeron between the particles A and B, for which there is no exchange of numbers quantum in the reaction. As s decreases, the contribution of other Reggeons becomes decisive and non-diffractive contamination becomes greater.

It is clear that the exchange in the t channel, which produces a LRG in the final state, should not lead to non-zero color charges. In fact, if it had mistaken the color, the color field would lead to the production of more particles capable to fill the gap in rapidity. In QCD the exchange of a Pomeron is described through the exchange of two gluons interacting with the quantum numbers of the vacuum.

1.4 Introduction to DDIS

Significant advances in understanding of the diffraction have been made using the electron-proton HERA 'collider', located in the DESY laboratory in Hamburg. This may seem strange because the diffraction typically is a process between hadrons while the *ep* scattering is an electroweak reaction, where the electron radiates a virtual photon (or Z^0 or $W^{\pm}$ boson), which then interacts with the proton. In fact, by considering the *ep* scattering in a reference system in which the virtual photon γ^* moves very quickly[6], as in the case of the reference system in which the proton is stationary, γ^* may fluctuate in a quark-antiquark pair (see Figure 1.4). Because of the Lorentz 'boost', this virtual pair has a much longer half-life than that typical of the strong interaction; thus the photon fluctuates in a pair long before the collision and it is the pair that interacts with the proton.

[6] At HERA, the impulse of the photon has reached the 50 TeV (see, for example, the reference [6]).

The pair is a small colour dipole.

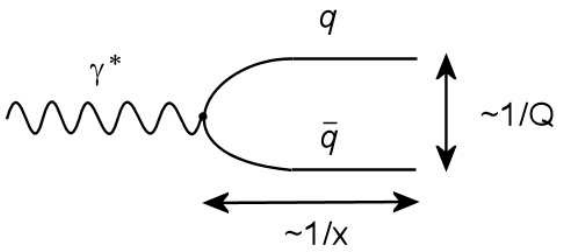

Figure 1.4: A virtual photon fluctuates into a $q\bar{q}$ pair, in the reference frame where the target proton is at rest.

Simple arguments of quantum mechanics can be used to show that the life time of the $q\bar{q}$ pairs is proportional to $1/x$ and that the transverse dimension of the pair is proportional to $1/Q$ [17, page 22]. Therefore it is possible to speak of diffractive dissociation of the photon in analogy with the diffractive dissociation of hadrons.

Increasing sufficiently the Q^2 virtuality of the photon, the transverse dimensions, typical of the dipole, become small compared to the hadron amplitude. This is an advantage in studying the diffraction in *ep* collisions, because it allows the transition from a regime of 'photoproduction' to that of 'electroproduction in the DIS' [7]. Therefore, the interaction between quark and antiquark, as well as the interaction of the $q\bar{q}$ pair with the proton, may be treated perturbatively and it is then interesting to understand if, with decreasing transverse dimension, i.e. with the increase of Q^2, it is observed a transition between the 'soft' regime and a 'hard' regime, for which the diffraction may be studied perturbatively. In fact, decreasing Q^2, the colour dipole becomes larger and, at very low values of Q^2, the interactions become so strong that a description in terms of quarks and gluons is no longer justified; therefore we can think that the photon fluctuates in a *vector meson* and we expect to detect diffractive reactions similar to those that occur in the case of hadron-hadron scattering. In this context, the hadronic

[7] The 'photoproduction' refers to processes where the lepton is widespread at small angles, emitting a photon near real, with $Q^2 \approx 0$, which interacts with the proton, while the 'electroproduction' denotes processes with exchange of a virtual photon, with $Q^2 \gg 0$. At HERA, the diffractive events were observed under the regimes of photoproduction [10, 18] and electroproduction in the DIS [8].

properties of the photon are described by the 'Vector Dominance Model' (*VDM*) [19], in which the production of vector mesons is dominant.

A different physical picture is obtained in a reference system where the incident proton is very fast. In this case the diffractive reaction may be considered as the deeply inelastic scattering, DIS, of a virtual photon on a target proton, with a very fast proton in the final state .

For the interaction with the $q\bar{q}$ pair, the struck quark spreads at wide-angle and may evolve into a jet in an attempt to leave the confinement region; for processes with small four-momentum transverse, the quark of incident proton may be little affected by the interaction with the photon and it recombines into the same initial hadron. So we find one of the final hadronic states below listed by which the diffractive events may be classified.

1. The proton is scattered with four-momentum substantially unchanged and it is produced a V resonance, constituted by a meson vector (or a real photon):

$$\gamma^* p \longrightarrow V p \,.$$

2. At least one of the incoming particles is dissociated in a state of great mass:

$$\begin{aligned} \gamma^* p &\longrightarrow V X \qquad \text{(proton dissociation)}\,, \\ \gamma^* p &\longrightarrow X p \qquad \text{(proton dissociation)}\,, \\ \gamma^* p &\longrightarrow X Y \qquad \text{(double dissociation)}\,. \end{aligned}$$

The results obtained regard inclusive and exclusive diffractive processes and they pass by the regime of photoproduction to electroproduction in the DIS [2, 20].

1.5 The kinematic variables in DDIS

For a complete description of the diffractive events, such as the one inclusive, $ep \longrightarrow eXp$, shown in Figure 1.5, it is necessary to introduce, in addition to variables kinematics defined in Appendix B.1, the following kinematic invariants.

1. The Mandelstam variable t, given by square of the four-momentum transferred in the proton vertex:

$$t = (p - p')^2 \ . \tag{1.5}$$

2. The squared mass of the hadronic system X, produced by dissociation of the photon:

$$M_X^2 = (q + p - p')^2 \ . \tag{1.6}$$

3. The fraction of the four-momentum lost by the incident proton, i.e. the fraction of the proton four-momentum carried by the object (the Pomeron $I\!P$ exchanged between the virtual photon and proton:

$$x_{I\!P} = \frac{(p - p') \cdot q}{p \cdot q} = \frac{Q^2 + M_X^2 - t}{Q^2 + W^2 - M_p^2} \, . \tag{1.7}$$

4. The variable β, which has the form of Bjorken variable x, defined with respect to the four-momentum $p - p'$ lost from the initial proton, rather than to the four-momentum p of the initial proton:

$$\beta = \frac{Q^2}{2\,(p - p')^2 \cdot q} = \frac{Q^2}{Q^2 + M_X^2 - t} \, ; \tag{1.8}$$

   β represents the fraction of the four-momentum of 'struck' quark carried by the Pomeron and its kinematic range is between 0 and 1.

$x_{I\!P}$ and β are related to the Bjorken variable $x = Q^2/(2p \cdot q)$ by the following equation:

$$x_{I\!P}\beta = x \, . \tag{1.9}$$

1.6 The diffractive scattering in ep collisions

The main features of inclusive processes in DDIS (see Figure 1.5)) are below listed.

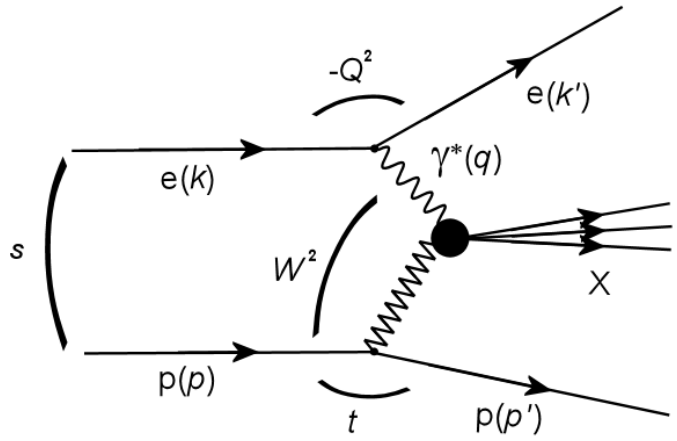

Figure 1.5: Diagram of an inclusive process $ep \longrightarrow eXp$ in DDIS. The four-momenta are shown in parentheses.

- The outgoing proton carries a large fraction x_L of four-momentum of the incoming proton. The diffractive events have so a peak (so-called 'diffraction peak') at $x_L \approx 1$. At HERA, the peak is roughly in the region $0.98 < x_L < 1$, as shown in Figure 1.6 "a" [21]. In addition, similarly to the case of elastic pp scattering discussed in subsection 1.2 (see Figure 1.2), the differential cross section $d\sigma/dt$ shows a marked exponential decrease presented in the form of Eq. (3.1), i.e. the events are highly suppressed at large $|t|$ (see Figure 1.6 "b" [22]). For processes $\gamma^* p \longrightarrow Vp$ (production of vector mesons), we observe that the B-parameter, which appears in Eq. (3.1), decreases with Q^2 for the light vector mesons and it is constant for the heavier vector mesons (see Figure 1.10).

- The collision of the virtual photon with proton produces a final hadronic state X which has invariant mass M_X and the quantum numbers of the photon. A large rapidity gap (or pseudorapidity) is present between X and proton of the final state. So the ep scattering combines features of the soft and hard processes. The electron receives a large transferred four-momentum, so Q^2 may be equal to hundreds of GeV^2. On the other hand the proton emerges with a four-momentum just changed.

In the context of DDIS, a particular process is the elastic photoproduction of a vector meson, represented in Figure 1.7.
It is generally assumed that the cross sections of the processes $\gamma p \longrightarrow Vp$ ($Q^2 \approx 0$)

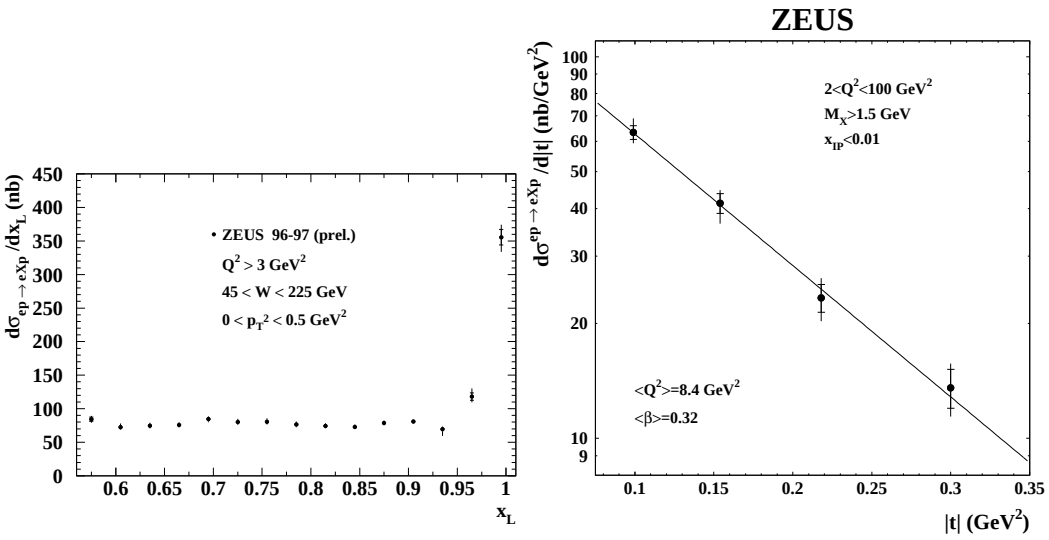

Figure 1.6: "a": The differential cross section $d\sigma/dx_L$ for $ep \longrightarrow eXp$ process; it is clearly visible the peak diffraction in $x_L \approx 1$ [21]. "b": The differential cross section $d\sigma/dt$ for $ep \longrightarrow eXp$ process when $x_L > 0.99$ [22].

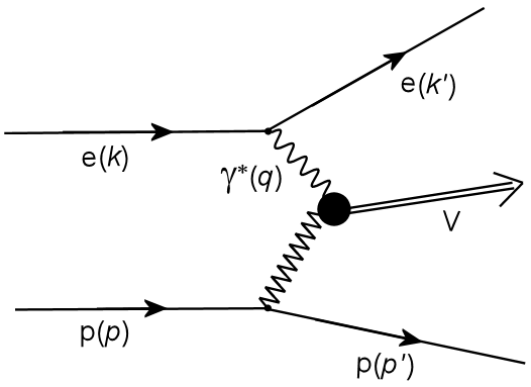

Figure 1.7: Diagram of a typical process where a vector meson V is in the final state.

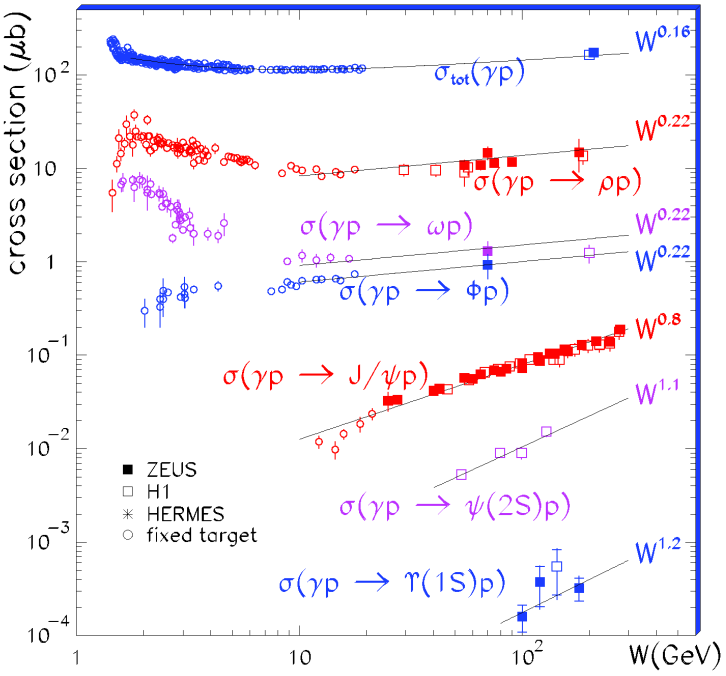

Figure 1.8: Cross section of the photoproduction ($Q^2 \approx 0$) of the vector mesons $\gamma p \longrightarrow Vp$, where $V = \rho, \omega, \varphi, J/\Psi, \psi(2S), \Upsilon$, with dependence on the energy W of the photon-proton center of mass. The graph shows the total cross section of the process γp. The linees are fitting curves by adopting the function W^{δ} on data at high energy [23].

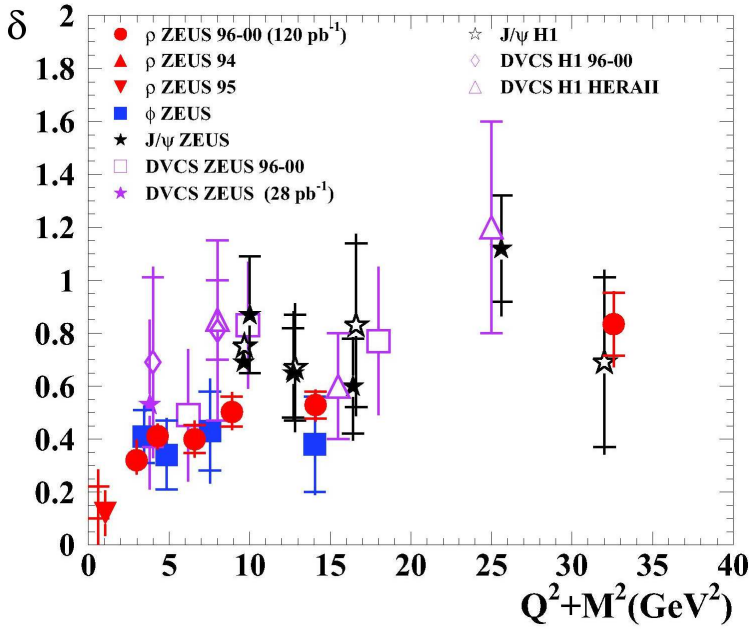

Figure 1.9: The dependence of δ-parameter on the hard scale $Q^2 + M^2$. The values of δ are extracted from fits on experimental data [23], by adopting the function W^{δ}.

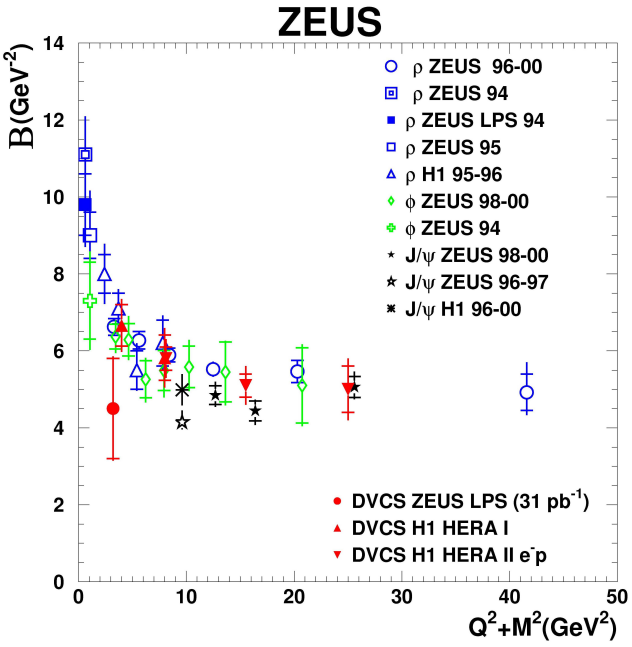

Figure 1.10: The dependence of B-parameter on the hard scale $Q^2 + M^2$. The values of B are extracted from fits on experimental data [23], by adopting the function $d\sigma/dt \propto e^{-B|t|}$. As shown, the parameter B decreases by increasing the scale, Q^2 for the DVCS and $Q^2 + M_V^2$ for photoproduction of vector mesons (in this case, at high energy, it seems that B becomes independent from vector meson).

have the form

$$\sigma \propto W^{\delta}\,, \tag{1.10}$$

where W is the energy of the photon-proton center of mass; δ-parameter increases from 0.2, for soft processes, to higher values, for hard processes (see Figure 1.9). The Figure 1.8 [23] shows the total cross section of the $\gamma p \longrightarrow Vp$ process, as a function of W; the experimental data ranging from the lightest vector meson, ρ, to heaviest meson, Υ. The experimental values of δ are shown in Figure 1.9 [23] as a function of $Q^2 + M^2$, where, in the case of photoproduction of vector mesons, $M = M_V$ and M_V indicates the mass of the vector meson. The minimum value for δ is approximately 0.2. The growth of cross section for the production of light vector mesons (ρ, ω, φ) may be described in the context of Regge Theory by exchange of the trajectory of a Pomeron. In the case of photoproduction of J/ψ and Υ, the growth of the cross section is steeper than that predicted by the Regge formalism. For the lightweight vector mesons, this steeper growth may be reached at high values of Q^2.

Chapter 2

The experimental data

In this chapter we analyze the procedure used to rescale the DVCS cross section data. We suggest a method which makes the rescaling more functional to conduct statistical analysis on overall data. The study can be applied to rescale data collected with different photon virtuality Q^2. We determine for the parameter n, used to describe the cross section as a function of Q^2, a different value compared to that adopted. We also show a dependence on Q^2 for the δ parameter used to describe the cross section as a function of W.

2.1 The *rescaling* procedure

The models used to interpret the Deeply Virtual Compton Scattering (DVCS) process are compared with an overall set of experimental results. This is obtained from several data sets collected at different energies. As shown in Figure 2.1, the DVCS is the diffractive scattering of a virtual photon (γ^*) off a proton (p), i.e. $\gamma^*\mathrm{p} \longrightarrow \gamma\mathrm{p}$ where γ denotes the outgoing photon. The integrated cross section can be reported [25] as a simple function:

$$\sigma(Q^2, W) \propto W^{\delta} \times \left(\frac{1}{Q^2}\right)^{n}, \tag{2.1}$$

where W is the invariant mass of the γ^*p system and Q^2 is the virtuality of the photon. δ and n are parameters obtained from fits to experimental data, by keeping fixed respectively the Q^2-value or the W-value. The cross section as a function of Q^2, or W, is measured by H1 and ZEUS experiments [25, 24, 26,

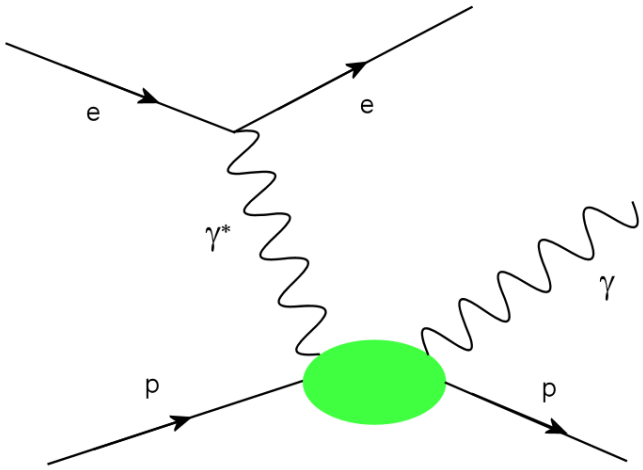

Figure 2.1: Diagram illustrating the DVCS. The process is accessed through the reaction ep $\longrightarrow$ eγp [25, 24, 26, 27, 28].

27, 28]. The overall set of experimental results is determined by a procedure consisting in rescaling the values of the raw data measured at different energies. This is possible by applying some factors that are used also for the error analysis. As example, the ZEUS Collaboration [24] data, taken at $W = 89\,\mathrm{GeV}$ and $Q^2 = 9.6\,\mathrm{GeV}^2$ (Table 2.1), were rescaled to the H1 Collaboration [25] data, taken at $W = 82\,\mathrm{GeV}$ and $Q^2 = 8\,\mathrm{GeV}^2$ (Table 2.2), with δ and n respectively fixed to values 0.75 and 1.54 [29]. In this case, the procedure for rescaling depends on

$\sigma(\gamma^* p \longrightarrow \gamma p)$(nb)			
Q^2	$W_{ZEUS} = 89\,\mathrm{GeV}$	W	$Q^2_{ZEUS} = 9.6\,\mathrm{GeV}^2$
7.5	$5.42 \pm 0.33^{+0.29}_{-0.34}$	45	$2.19 \pm 0.24^{+0.11}_{-0.14}$
12.5	$2.64 \pm 0.22^{+0.22}_{-0.23}$	55	$2.96 \pm 0.28^{+0.13}_{-0.18}$
20	$1.23 \pm 0.14^{+0.05}_{-0.07}$	65	$3.62 \pm 0.36^{+0.18}_{-0.23}$
32.5	$0.59 \pm 0.12^{+0.04}_{-0.04}$	75	$3.88 \pm 0.42^{+0.18}_{-0.26}$
55	$0.20 \pm 0.08^{+0.03}_{-0.02}$	85	$3.59 \pm 0.45^{+0.18}_{-0.25}$
85	$0.16 \pm 0.09^{+0.02}_{-0.03}$	95	$3.29 \pm 0.55^{+0.31}_{-0.49}$
		105	$6.24 \pm 0.77^{+0.31}_{-0.49}$
		115	$4.86 \pm 0.76^{+0.39}_{-0.44}$
		125	$4.69 \pm 0.82^{+0.32}_{-0.36}$
		135	$5.55 \pm 0.99^{+0.91}_{-0.30}$

Table 2.1: Values of the cross sections [24] for the $\gamma^* p \longrightarrow \gamma p$ DVCS process as a function of Q^2 ($W = 89\,\mathrm{GeV}$ fixed) and W ($Q^2 = 9.6\,\mathrm{GeV}^2$ fixed). The first uncertainty is statistical and the second systematic. The systematic uncertainty due to the luminosity determination is not included.

$\sigma(\gamma^* p \longrightarrow \gamma p)$(nb)			
Q^2	$W_{H1} = 82\,\mathrm{GeV}$	W	$Q^2_{H1} = 8\,\mathrm{GeV}^2$
3.0	$15.7 \pm 2.5 \pm 3.4$	45	$2.28 \pm 0.21 \pm 0.34$
5.25	$5.7 \pm 1.1 \pm 1.4$	70	$2.91 \pm 0.21 \pm 0.51$
8.75	$3.20 \pm 0.49 \pm 0.69$	90	$3.97 \pm 0.54 \pm 0.85$
15.5	$1.20 \pm 0.22 \pm 0.32$	110	$4.4 \pm 1.0 \pm 1.5$
25	$0.70 \pm 0.19 \pm 0.19$	130	$6.4 \pm 2.5 \pm 2.7$
55	$0.15 \pm 0.05 \pm 0.05$		
$\delta = 0.77 \pm 0.23 \pm 0.19$		$n = 1.54 \pm 0.09 \pm 0.04$	

Table 2.2: Values of the cross sections [25] for the $\gamma^* p \longrightarrow \gamma p$ DVCS process as a function of Q^2 ($W = 82\,\mathrm{GeV}$ fixed) and W ($Q^2 = 8\,\mathrm{GeV}^2$ fixed) for $|t| < 1\,\mathrm{GeV}^2$. The first uncertainty is statistical and the second systematic. Here we have reported the values of δ and n calculated by H1 Collaboration for $|t| < 1\,\mathrm{GeV}^2$. The value of n is calculated at $W = 82\,\mathrm{GeV}$; the value of δ for the combined sample of all data at $Q^2 = 8\,\mathrm{GeV}^2$.

the definition of appropriate normalization factors[1], which are indicated hereafter with ε. In particular, $\varepsilon_{_{Q^2}}$ represents the normalization factor when we consider the cross section, $\sigma(W)$, as a function of W with fixed Q^2; $\varepsilon_{_W}$ represents the normalization factor when considering the cross section, $\sigma(Q^2)$, as a function of Q^2 with fixed W. Using the Eq. (2.1) we have

$$\sigma_r(W) = \frac{\sigma_s(Q^2_s, W)}{\sigma_{dr}(Q^2_{dr}, W)}\,\sigma_{dr}(W) = \frac{(Q^2_{dr})^{n_{dr}}}{(Q^2_s)^{n_s}}\sigma_{dr}(W)\,, \tag{2.2}$$

$$\sigma_r(Q^2) = \frac{\sigma_s(Q^2, W_s)}{\sigma_{dr}(Q^2, W_{dr})}\,\sigma_{dr}(Q^2) = \frac{(W_s)^{\delta_s}}{(W_{dr})^{\delta_{dr}}}\,\sigma_{dr}(Q^2)\,, \tag{2.3}$$

where the subscripts "dr", "s" and "r" respectively denote the data to be rescaled, those considered in scale and the rescaled data. The previous relations allow us to obtain the following formulas:

$$\varepsilon_{_{Q^2}} = \frac{(Q^2_{dr})^{n_{dr}}}{(Q^2_s)^{n_s}}\,, \tag{2.4}$$

$$\varepsilon_{_W} = \frac{(W_s)^{\delta_s}}{(W_{dr})^{\delta_{dr}}}\,. \tag{2.5}$$

In the "standard" procedure the equalities $\delta_{dr} = \delta_s = \delta$ and $n_{dr} = n_s = n$ are considered valid [29], hereby the normalization factor $\varepsilon_{_{Q^2}}$, for $\sigma_{dr}(W) \to \sigma_r(W)$, is given by the ratio between $(Q^2_{dr})^n$ and $(Q^2_s)^n$ and the normalization factor

[1] If we multiply or divide the data by a constant, the mean and the standard deviation will be multiplied or divided by the value of the constant [30].

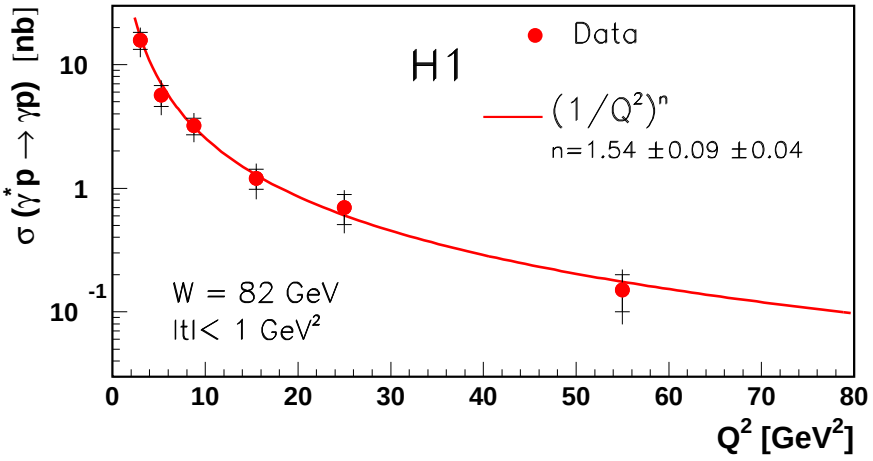

Figure 2.2: The $\gamma^* p \longrightarrow \gamma p$ cross section [25] as a function of Q^2 for $W = 82\,\text{GeV}$ and $|t| < 1\,\text{GeV}$. The inner error bars represent the statistical and the full error bars the quadratic sum of the statistical and systematic uncertainties. The curve is the result of a fit to the form $(1/Q^2)^n$, giving the value of n shown in the figure (see Table 2.2).

ε_W, for $\sigma_{dr}(Q^2) \rightarrow \sigma_r(Q^2)$, is given by the ratio between $(W_s)^\delta$ and $(W_{dr})^\delta$. Considering $\delta = 0.77$ and $n = 1.54$ [25] (see Table 2.2 and Figure 2.2 [25]), the ZEUS measurements are rescaled to the Q^2 and W values of the H1 measurements through following expressions:

$$\sigma_r(W) = \varepsilon_{_{Q^2}}\, \sigma_{dr}(W) \simeq 1.3242\, \sigma_{dr}(W)\,, \tag{2.6}$$

$$\sigma_r(Q^2) = \varepsilon_{_W}\, \sigma_{dr}(Q^2) \simeq 0.9389\, \sigma_{dr}(Q^2)\,. \tag{2.7}$$

As shown in Figure 2.3, where we illustrate the effect of the procedure for rescaling the cross section as function of Q^2, the rescaled ZEUS data are roughly moved over the H1 data. To highlight this feature, we fit lines to data in order to catch the general trend of the two data series which allows us to compare the trends of two data sets.

2.2 New procedure of rescaling

The analysis of the two fits shown in Figure 2.3 evidences that the rescaled ZEUS data tend to remain higher than those of H1; therefore it seems that the "standard" procedure described above does not rescale the ZEUS experimental data to

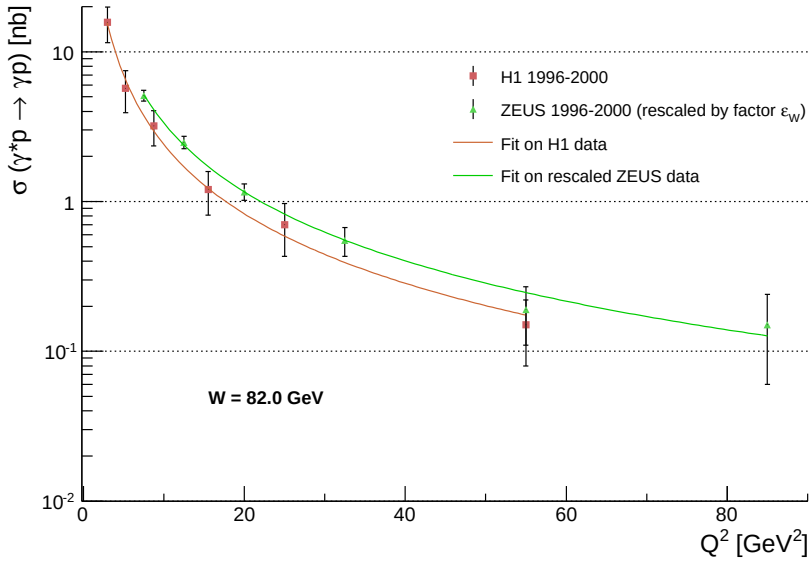

Figure 2.3: DVCS cross section $\sigma(\gamma^* p \longrightarrow \gamma p)$ as function of Q^2 for $W = 82\,\mathrm{GeV}$ ($|t| < 1.0\,\mathrm{GeV}^2$, where t is the four momentum transfer squared at the proton vertex). The error bars represent the statistical and systematic uncertainties added in quadrature. The experimental data collected by the ZEUS Collaboration [24] have been rescaled to those collected by the H1 Collaboration [25] using Eq. (2.7), where $\varepsilon_W \simeq 0.9389$.

those of H1. In particular, data points for $Q^2 = 55\,\mathrm{GeV}^2$ are not superimposed, although they are consistent within the error bars. Indeed, we would expect that, after rescaling, the data will be superimposed when they refer to the same value of Q^2. In this regard, we might consider an alternative rescaling procedure by normalizing the ZEUS data to those of H1 and using the following normalization factor:

$$\varsigma_W = \frac{\sigma_s(Q^2 = 55\,\mathrm{GeV}^2)}{\sigma_{dr}(Q^2 = 55\,\mathrm{GeV}^2)} = \frac{0.15}{0.20} = \frac{3}{4}\,, \tag{2.8}$$

where 0.15 and 0.20 are the cross section values measured by ZEUS and H1 experiments at the same value of Q^2. Figure 2.4 shows the ZEUS data rescaled according to Eq. (2.8). As the previous figures show, the changing of normalization factor has given a better approximation of rescaled ZEUS data to those of H1. However, Figure 2.4 shows clearly that it is not possible to conduct statistical analysis on overall data. In the current study we consider [31] that the rescaling procedure should be based on a a comparison of the trend determined by fit to the rescaled ZEUS data with the trend determined by fit to the H1 data, i.e. the characteristic parameters of both fits must have similar values since the fitting

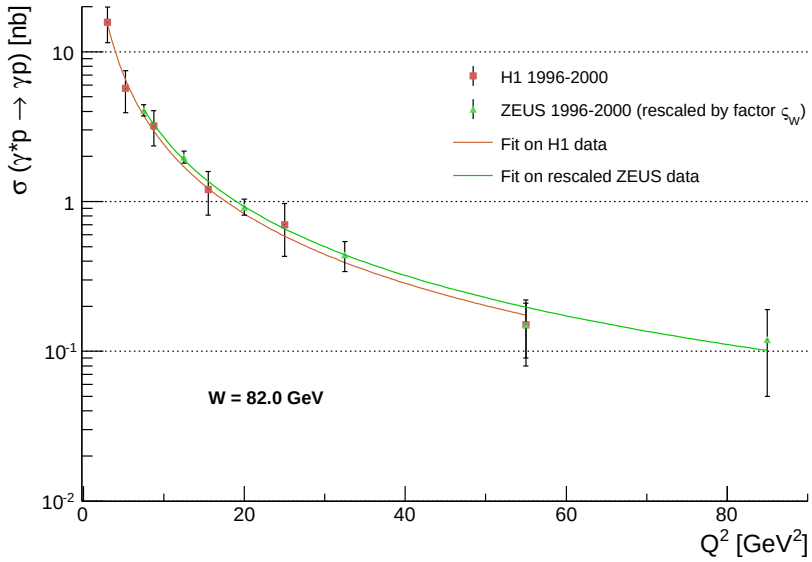

Figure 2.4: DVCS cross section $\sigma(\gamma^* p \longrightarrow \gamma p)$ as function of Q^2 for $W = 82\,\text{GeV}$ ($|t| < 1.0\,\text{GeV}^2$). The error bars represent the statistical and systematic uncertainties added in quadrature. The experimental data collected by the ZEUS Collaboration [24] have been rescaled to those collected by the H1 Collaboration [25] using the normalization factor $\varsigma_W = 3/4 = 0.75$ determined by Eq. (2.8) [31].

curves must be proximate. This observation is physically correct because the process is the same for both Collaborations, although the data are collected at different Q^2 and W values. In effect, if the ZEUS and H1 data were taken at the same energies, we would expect similar values for the characteristic parameters of the fits. This consideration is the basis of any rescaling procedure. Also to avoid experimenter's bias, we suggest to consider the trend of the fits to the data rather than data points itself. Therefore it is necessary to redefine another normalization factor, which we indicate with ζ_W. The latter can be determined by varying the value of ς_W until there is sound agreement on characteristic parameters of fits, as previously highlighted. So we find $\zeta_W = 0.67$, value for which the parameters of fits describe the same curve as the Figure 2.5 shows. In this case, the fit on overall data gives a n-value compatible with that obtained by the H1 Collaboration, i.e. $n = 1.54 \pm 0.09 \pm 0.04$ [25], where the first error is statistical, the second systematic.

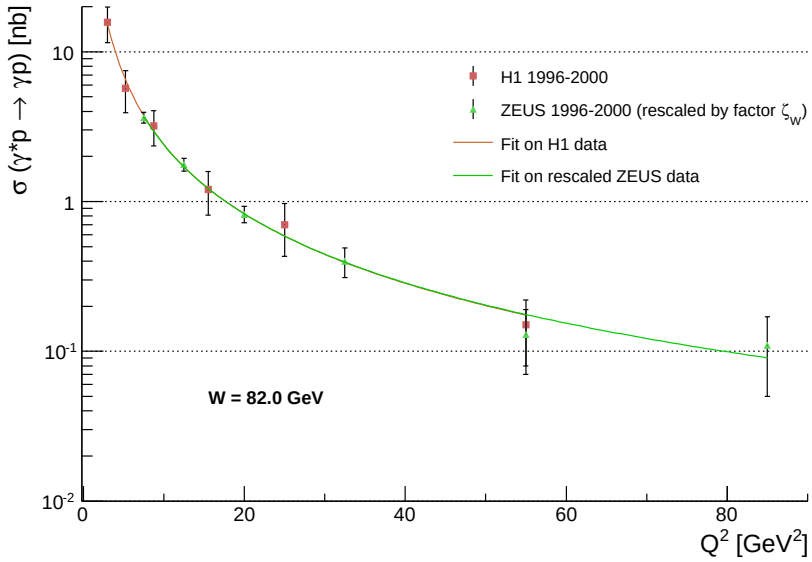

Figure 2.5: DVCS cross section $\sigma(\gamma^* p \longrightarrow \gamma p)$ as function of Q^2 for $W = 82\,\text{GeV}$ ($|t| < 1.0\,\text{GeV}^2$). The error bars represent the statistical and systematic uncertainties added in quadrature. The experimental data collected by the ZEUS Collaboration [24] have been rescaled to those collected by the H1 Collaboration [25] using the normalization factor $\zeta_W = 0.67$ determined in Section. 2.2 [31].

2.2.1 New normalization factor for fixed W

Adopting the following power-type function

$$\sigma(Q^2) = a \times \left[1/Q^2\right]^n \tag{2.9}$$

and by performing a fit on H1 data, we have[2] $a_s = 83.47 \pm 10.96$ and $n_s = 1.54 \pm 0.06$, with reduced chi-square $\chi^2/\text{d.o.f.} = 0.15$; these parameters are compatible with those calculated by performing a fit on the rescaled ZEUS data using ζ_W factor: $a_{\zeta_W} = 80.99 \pm 8.71$ and $n_r = 1.53 \pm 0.04$, with $\chi^2/\text{d.o.f.} = 0.26$. Furthermore, if we use the factor ε_W for the rescaling procedure, the fit on rescaled ZEUS data gives $a_{\varepsilon_W} = 113.50 \pm 12.21$, which is inconsistent with a_s. Hence we must introduce the factor ζ_W and reject the standard procedure. It's possible to move from ε_W to ζ_W by applying the following formula:

$$\zeta_W = \frac{a_{\zeta_W}}{a_{\varepsilon_W}}\,\varepsilon_W \equiv \Xi_W\,\varepsilon_W\,, \tag{2.10}$$

where we introduce the factor Ξ_W. This one may show a W dependence which could not be considered taking only the factor ε_W. The value of Ξ_W is found from

[2]The statistical analyses conducted here were performed using the program *OriginPro* [32].

Eq. (2.10):

$$\Xi_{_W} = \frac{\zeta_{_W}}{\varepsilon_{_W}} \simeq 0.71\,. \tag{2.11}$$

We might ask if $\Xi_{_W}$ can be determined using the ratio between the W energies with which the H1 and ZEUS Collaborations have performed their measurements. Actually this event happens when we raise the ratio to the fourth power:

$$\Xi_W \simeq \left(\frac{W_s}{W_{dr}}\right)^4 = \left(\frac{82}{89}\right)^4 = 0.72\,. \tag{2.12}$$

Hence, in order to make the rescaling procedure more efficient in statistical terms, it is necessary to replace $\varepsilon_{_W}$ with the following normalization factor [31]:

$$\varepsilon_{_W}^{'} \simeq \left(\frac{W_s}{W_{dr}}\right)^{4+\delta} = \left(\frac{82}{89}\right)^{4+\delta} = 0.6766\,, \tag{2.13}$$

where we use $\delta = 0.77$ [25]. Since the $\varepsilon_{_W}^{'}$ value is approximately equal to $\zeta_{_W}$, the curve in Figure 2.5 represents approximately the fit of the power function to ZEUS data rescaled by the $\varepsilon_{_W}^{'}$ factor. If we fit the overall data using the function of Eq. 2.9, we obtain $a = 84.21 \pm 9.06$ and $n = 1.54 \pm 0.04$, with $\chi^2/\text{d.o.f.} = 0.26$; these parameters are clearly compatible with those obtained by the fit to the H1 data.

2.3 Method for rescaling the DVCS data

Introducing the following function [31]

$$\mathcal{P}(Q, W) = W^{4+\delta} \times \left(\frac{1}{Q^2}\right)^n\,, \tag{2.14}$$

Eq. (2.1) can be written as

$$\sigma(Q^2, W) \propto \frac{1}{W^4}\,\mathcal{P}(Q, W)\,, \tag{2.15}$$

whereby, according the rescaling procedure here proposed, we have to carry out the ratio between the quantities $\mathcal{P}_s$ and $\mathcal{P}_{dr}$:

$$\sigma_r(W) = \frac{\mathcal{P}_s(Q_s, W)}{\mathcal{P}_{dr}(Q_{dr}, W)}\,\sigma_{dr}(W)\,, \tag{2.16}$$

$$\sigma_r(Q^2) = \frac{\mathcal{P}_s(Q, W_s)}{\mathcal{P}_{dr}(Q, W_{dr})}\, \sigma_{dr}(Q^2)\,. \tag{2.17}$$

In general, the differential cross section for the DVCS process, $d\sigma/dt$, can be expressed at high energies[3] [2] as

$$\frac{d\sigma}{dt} = \frac{1}{16\,\pi\,s^2}\,|\mathcal{M}|^2\,, \tag{2.18}$$

where the variable t is the square of the four-momentum transferred at the proton vertex, s is the squared centre-of-mass energy of the incoming system, i.e. $s = W^2$, and $\mathcal{M}$ is the DVCS amplitude. If the W dependence of the integrated cross section $\int (d\sigma/dt)\, dt$ is the same, over the relevant W domain, as the W dependence of the differential cross section[4] $d\sigma/dt$ for $t = \langle t \rangle$, then the cross section can be expressed, as indicated in Eq. 2.15, in terms of W^{-4}. These considerations suggest that the function $\mathcal{P}$ is proportional to the integrated squared modulus of the DVCS amplitude. Therefore, according the Eq. 2.16 and Eq. 2.17, the ZEUS measurements can be rescaled to the values of the H1 measurements by performing the ratio between the integrated squared modula of scattering amplitudes of the process studied in H1 and ZEUS experiments. In this manner it is interesting to note that the rescaling procedure depends essentially on the scattering amplitudes and that these latter contain all the information about the dynamics of the process.

2.4 Dependence of δ-parameter on Q^2

In Table 2.3 we have collected the δ-values calculated by ZEUS and H1 experiments [25, 24, 27, 28]. Taking into account that several values are not within the error bars of other values, we consider the possibility of treating the δ-parameter as function of Q^2, contrary to indications in literature which state that δ is independent of Q^2 within the errors [28]. All the functions used to fit data of Table 2.3 exhibit a similar trend[5] especially for low values of Q^2. In Figure 2.6 two fits are

[3] See Eq. A.45 in Appendix A.2.

[4] See footnote 14 of Ref. [33].

[5] Through *OriginPro 8* [32] we identified 23 functions able to fit the experimental data of Table 2.3 with a reduced chi-square value ranging from ~ 0.2 to ~ 0.6. The idea is to show that δ is dependent on Q^2; nevertheless, it is not the main interest to statistically analyze the data, but to check, even watching, whether the dependence is actual.

Q^2 [GeV^2]	δ	Reference
2.4	0.44 ± 0.19	ZEUS 1999-2000 [27]
3.2	0.52 ± 0.09	ZEUS 1999-2000 [27]
4	$0.69 \pm 0.32 \pm 0.17$	H1 1996-1997 [25]
6.2	0.75 ± 0.17	ZEUS 1996-2000 [27]
8	$0.81 \pm 0.34 \pm 0.22$	H1 1999-2000 [25]
8	$0.61 \pm 0.10 \pm 0.15$	H1 2004-2007 [28]
9.6	$0.75 \pm 0.15^{+0.08}_{-0.06}$	ZEUS 1996-2000 [24]
9.9	0.84 ± 0.18	ZEUS 1996-2000 [27]
15.5	$0.61 \pm 0.13 \pm 0.13$	H1 2004-2007 [28]
18	0.76 ± 0.22	ZEUS 1996-2000 [27]
25	$0.90 \pm 0.36 \pm 0.27$	H1 2004-2007 [28]

Table 2.3: δ-values collected by various Collaborations. Only some measurements present two kinds of errors; in these cases, the first are statistical errors and the second ones are systematic.

shown: one is logarithmic-type, another one is power-type. The logarithmic-type curve is given by the following equation [31]:

$$\delta(Q^2) = \delta_0 - \delta_1 \ln(Q^2 + \delta_2)\,, \tag{2.19}$$

where $\delta_0 = 0.5421 \pm 0.0768$, $\delta_1 = -0.0857 \pm 0.0389$ and $\delta_2 = -2.1511 \pm 0.5414$, with χ^2/d.o.f. $= 0.2497$; the power-type curve is given by the following equation [31]:

$$\delta(Q^2) = \delta' \left[1 - (Q^2)^{-\delta_p}\right]\,, \tag{2.20}$$

where $\delta' = 0.8232 \pm 0.0887$ and $\delta_p = 0.9137 \pm 0.2455$, with χ^2/d.o.f. $= 0.2051$. Since δ is treated as a function of Q^2, we have that the factor $\varepsilon_W^{'}$ depends on Q^2 [31]:

$$\varepsilon_W^{'} = \left(\frac{W_s}{W_{dr}}\right)^{4+\delta(Q^2)}\,. \tag{2.21}$$

Figure 2.7 shows the trend determined by fit to the ZEUS data, which are rescaled by using Eq. (2.21) and Eq. (2.19). This trend is superimposed to that determined by fit to the H1 data. In effect, by performing a fit to the rescaled ZEUS data, we have $a_r = 83.74 \pm 8.99$ and $n_r = 1.54 \pm 0.04$, with χ^2/d.o.f. $= 0.26$; these parameters are compatible with a_s and n_s obtained by performing a fit to the

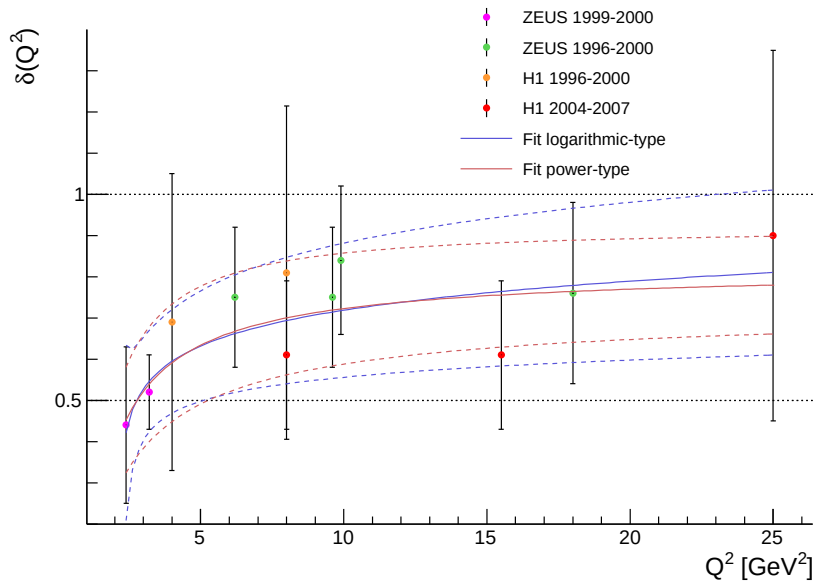

Figure 2.6: δ parameter as a function of Q^2. The experimental values are given in Table 2.3. Two fits are shown. The dotted lines indicate the error bands.

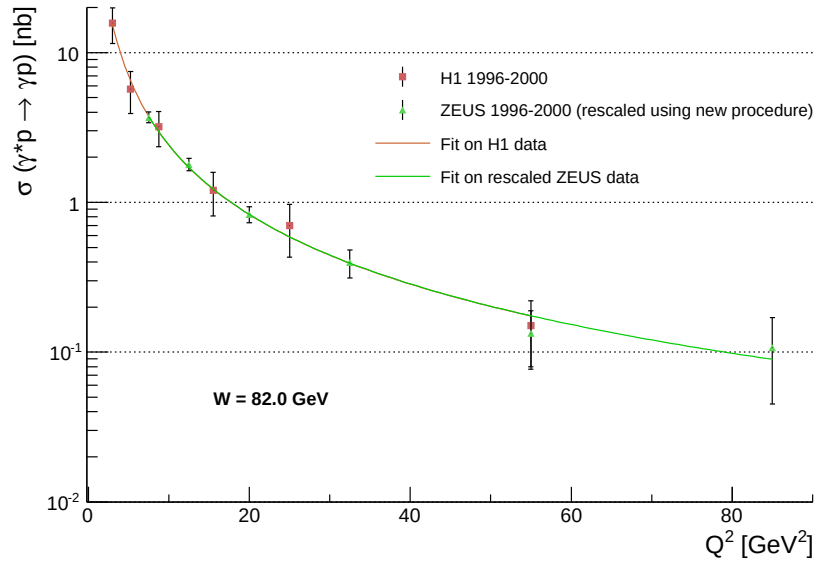

Figure 2.7: DVCS cross section $\sigma(\gamma^* p \longrightarrow \gamma p)$ as function of Q^2 for $W = 82\,\mathrm{GeV}$ ($|t| < 1.0\,\mathrm{GeV}^2$). The error bars represent the statistical and systematic uncertainties added in quadrature. The experimental data collected by the ZEUS Collaboration [24] have been rescaled to those collected by the H1 Collaboration [25] using Equations (2.21) and (2.19) [31].

H1 data. It is interesting to note that the trends overlap although the visible dependence of δ on Q^2 has introduced a dependence of ε'_W on Q^2 in an independent manner with respect to the rescaling analysis conducted in Section. 2.2.1. Clearly, the growth, at low Q^2, and the flattening, at high Q^2, of δ do not fundamentally modify the rescaling procedure here proposed.

2.5 Rescaling for Q^2 fixed

In the case of the data of H1 Collaboration [25] (see Table 2.4, we can compare the "standard" procedure, expressed by Eq. (2.2), with the proposed rescaling, expressed by Eq. (2.16), by using the experimental values of $\sigma(W)$ collected at $Q^2 = 8\,\mathrm{GeV}^2$ and $Q^2 = 4\,\mathrm{GeV}^2$. Following the indications given in [31], Section 2.2, we consider the trends determined by fits to the data by adopting the following power-type function derived by Eq. (2.15):

$$\sigma(W) = c \times W^{\delta(Q^2)}\,. \tag{2.22}$$

As shown in Fig. 2.8, two fits are performed on each data set: the first one

$\sigma(\gamma^* p \longrightarrow \gamma p)$ (nb)		
W (GeV)	$Q^2 = 4\,\mathrm{GeV}^2$	$Q^2 = 8\,\mathrm{GeV}^2$
45	$6.5 \pm 0.8 \pm 1.1$	$2.56 \pm 0.36 \pm 0.32$
70	$8.9 \pm 1.3 \pm 1.6$	$2.93 \pm 0.63 \pm 0.46$
90	$11.1 \pm 2.2 \pm 2.7$	$4.45 \pm 0.83 \pm 0.82$
110	$10.1 \pm 4.7 \pm 4.6$	$5.30 \pm 1.40 \pm 1.40$
130	—	$6.40 \pm 2.50 \pm 2.70$
δ	$0.69 \pm 0.32 \pm 0.17$	$0.81 \pm 0.34 \pm 0.22$

Table 2.4: Values of the cross sections [25] for the $\gamma^* p \longrightarrow \gamma p$ DVCS process as a function of W ($Q^2 = 4\,\mathrm{GeV}^2$ fixed and $Q^2 = 8\,\mathrm{GeV}^2$ fixed, for $|t| < 1\,\mathrm{GeV}^2$). The first uncertainty is statistical and the second systematic. Here we have reported also the values of δ.

leaving free all parameters, the second by setting the δ-parameter at well-defined values. The latter are obtained by the Eq. (2.19). We assume to rescale the data collected at $Q^2_{dr} = 4\,\mathrm{GeV}^2$ to the data collected at $Q^2_s = 8\,\mathrm{GeV}^2$. The associated values[6] of δ are respectively $\delta_{dr} = 0.5948$ and $\delta_r = \delta_s = 0.6935$. Considering

[6] As it is done in the literature, here we omit the analysis of the errors on δ when we rescale data.

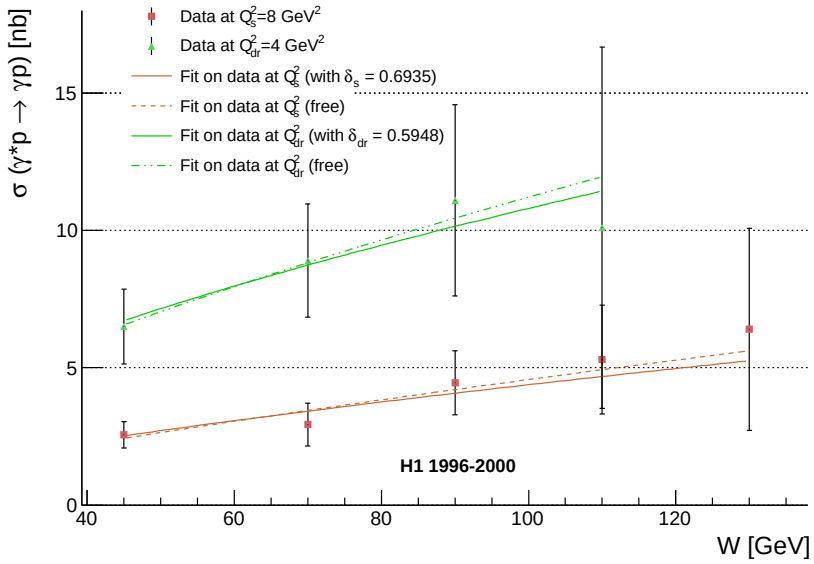

Figure 2.8: DVCS cross section $\sigma(\gamma^* p \longrightarrow \gamma p)$ as function of W for fixed values of Q^2 ($|t| < 1.0\,\mathrm{GeV}^2$). The error bars represent the statistical and systematic uncertainties added in quadrature. The experimental data are collected by the H1 Collaboration [25].

$n_{dr} = n_s = n = 1.54$ [25, 24], the standard normalization factor is

$$\varepsilon_{_{Q^2}} = \frac{(Q^2_{dr})^{n_{dr}}}{(Q^2_s)^{n_s}} = \frac{(4)^{1.54}}{(8)^{1.54}} = 0.3439\,, \tag{2.23}$$

which leads to the rescaled data of Fig. 2.9. As stated in Section 2.2 [31], after rescaling the fitting curves of the rescaled data and those in scale must be proximate, i.e. the characteristic parameters of both fits must have similar values. Therefore, we compare the trend determined by fit to rescaled data, leaving free all parameters, with the trend determined by fit to data in scale, by setting $\delta = \delta_s$. As shown in Fig. 2.9, the fitting curves are sufficiently far apart, for which the rescaling procedure should be reviewed. By performing a fit on the data to rescale and by setting $\delta = \delta_{dr}$, we have $c^*_{dr} = 0.6980 \pm 0.0211$ (χ^2/d.o.f. $= 0.0493$); the ratio

$$\frac{c_s}{c^*_{dr}} = \frac{0.1797}{0.6980} \simeq 0.2575 \tag{2.24}$$

differs significantly from $\varepsilon_{_{Q^2}} = 0.3439$. This difference may depend on the variations of δ by changing Q^2. In effect, the Eq. (2.16) may be written as

$$\sigma_r(W) = \varepsilon_{_{Q^2}}\, W^{(\delta_s - \delta_{dr})}\, \sigma_{dr}(W)\,, \tag{2.25}$$

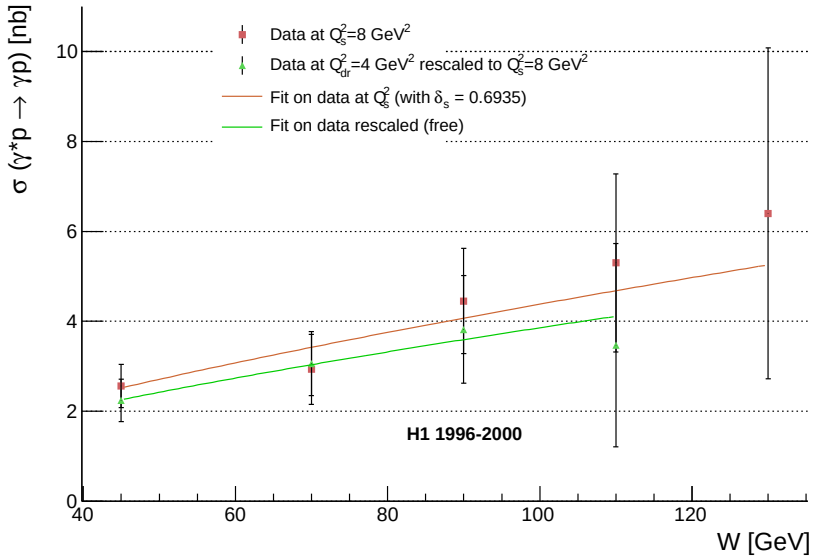

Figure 2.9: DVCS cross section $\sigma(\gamma^* p \longrightarrow \gamma p)$ as function of W for $Q^2 = 8\,\mathrm{GeV}^2$ ($|t| < 1.0\,\mathrm{GeV}^2$). The error bars represent the statistical and systematic uncertainties added in quadrature. The experimental data [25] collected at $Q^2 = 4\,\mathrm{GeV}^2$ have been rescaled to those collected at $Q^2 = 8\,\mathrm{GeV}^2$ using the standard rescaling procedure, i.e. the normalization factor $\varepsilon_{_{Q^2}}$ determined by Eq. (2.23).

where the non-unitary value of $W^{(\delta_s - \delta_{dr})}$ causes the difference between c_s/c_{dr} and $\varepsilon_{_{Q^2}}$. Therefore, it is necessary considering possible changes to the $\delta(Q^2)$-trend, which are able to improve the rescaling as stated in Section 2.2.

2.5.1 About n parameter

Eq. (2.23) shows a dependence of the normalization factor on n parameter. The difference between c_s/c_{dr} and $\varepsilon_{_{Q^2}}$ may be given by a different value of n compared with what reported in literature [25, 24], $n = 1.54$. Adopting the power-type function of Eq. (2.9) and by performing a fit on ZEUS [27] and H1 [28] data (see Table 2.5), we have respectively $n = 1.5278 \pm 0.0549$ and $n = 1.7670 \pm 0.0584$; the latter value is not compatible with those determined by performing a fit on ZEUS [24] and H1 [25] data (see previous Tables 2.1 and 2.2). As indicated Table 2.6, we perform several fits on H1 [28] data by varying n-parameter until the value 1.54 and we evaluate the reduced chi-square (χ^2/d.o.f.) to check adaptation of the curve with the experimental points. Clearly, the value $n = 1.54$ may not be acceptable for the data examined in Part (a) of Table 2.6 (see also Figure 2.10).

$\sigma(\gamma^* p \longrightarrow \gamma p)$ (nb)			
ZEUS 1999-2000 [27]		H1 2004-2007 [28]	
Q^2 [GeV^2]	$W = 104\,\text{GeV}$	Q^2 [GeV^2]	$W = 82\,\text{GeV}$
3.25	$21.28 \pm 0.92^{+1.02}_{-1.34}$	8.75	$3.87 \pm 0.15 \pm 0.41$
7, 50	$5.87 \pm 0.42^{+0.14}_{-0.30}$	15.50	$1.46 \pm 0.07 \pm 0.18$
12.50	$3.27 \pm 0.33^{+0.07}_{-0.16}$	25.00	$0.55 \pm 0.07 \pm 0.08$
20.00	$1.23 \pm 0.21^{+0.05}_{-0.08}$	55.00	$0.16 \pm 0.02 \pm 0.03$
32.50	$0.55 \pm 0.18^{+0.04}_{-0.04}$	—	—
70.00	$0.16 \pm 0.07^{+0.02}_{-0.02}$	—	—

Table 2.5: Values of the cross sections [27, 28] for the $\gamma^* p \longrightarrow \gamma p$ DVCS process as a function of Q^2 (W fixed). The first uncertainty is statistical and the second systematic.

By varying n in the range from $\sim$ 1.54 to 1.77, the fits on ZEUS [24] and H1 [25, 28] data become acceptable for $n = 1.65$, conversely the fit on ZEUS [27] data is good only for n values close to 1.528, as shown in Table 2.6 (see also Figures 2.11, 2.12 and 2.13).

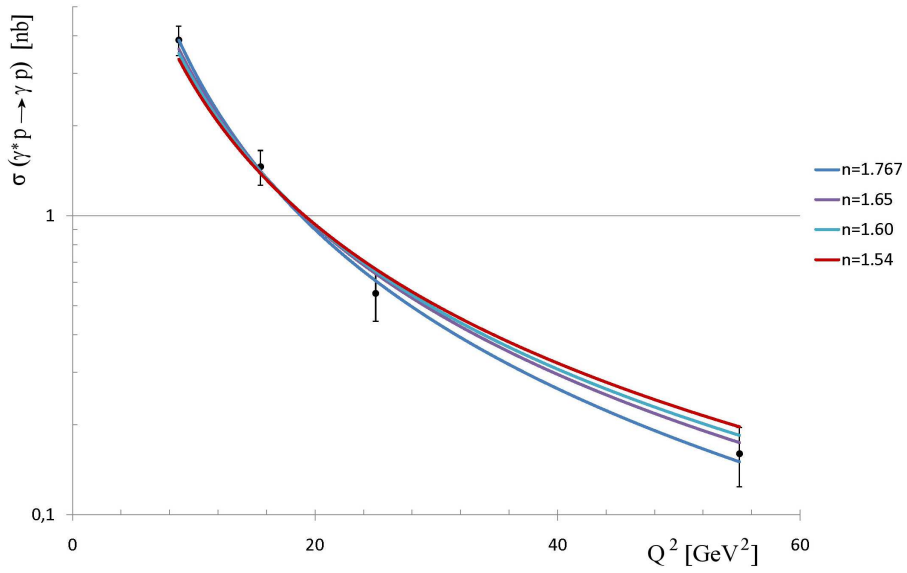

Figure 2.10: DVCS cross section $\sigma(\gamma^* p \longrightarrow \gamma p)$ as function of Q^2 for $W = 82\,\text{GeV}$ ($|t| < 1.0\,\text{GeV}^2$). The error bars represent the statistical and systematic uncertainties added in quadrature. The experimental data have been collected by the H1 2004-2007 [28].

We note that the ZEUS [27] data set has a high value of reduced chi-square even for the best fit performed. Therefore we must consider how the data are

	H1 2004-2007 [28], $W = 82\,\mathrm{GeV}$ $(m = 4)$			
Part (a)	n	a	r_0^2	χ^2/d.o.f.
	1.7670 ± 0.0584	178.8174 ± 28.8188	0.9949	0.2069
	1.65 (fixed)	129.455 ± 6.280	0.9895	0.4257
	1.60 (fixed)	112.241 ± 7.181	0.9819	0.7367
	1.54 (fixed)	94.207 ± 7.946	0.9688	1.2691
	H1 1996-2000 [25], $W = 82\,\mathrm{GeV}$ $(m = 6)$			
Part (b)	n	a	r_0^2	χ^2/d.o.f.
	1.77 (fixed)	129.2297 ± 12.6228	0.9410	0.5393
	1.65 (fixed)	103.8508 ± 6.3692	0.9761	0.2187
	1.5437 ± 0.0558	83.4663 ± 10.9586	0.9841	0.1455
	ZEUS 1996-2000 [24], $W = 89\,\mathrm{GeV}$ $(m = 6)$			
Part (c)	n	a	r_0^2	χ^2/d.o.f.
	1.77 (fixed)	214.7389 ± 12.2329	0.9767	1.1691
	1.65 (fixed)	161.7201 ± 5.4968	0.9916	0.4205
	1.5324 ± 0.0456	123.0941 ± 14.3137	0.9957	0.2146
	ZEUS 1999-2000 [27], $W = 104\,\mathrm{GeV}$ $(m = 6)$			
Part (d)	n	a	r_0^2	χ^2/d.o.f.
	1.77 (fixed)	195.3776 ± 15.6387	0.9637	3.4514
	1.65 (fixed)	161.2586 ± 8.2323	0.9850	1.4303
	1.5278 ± 0.0549	130.2238 ± 14.0497	0.9914	0.8162

Table 2.6: Values of the parameters determined by a fit, according the Eq. (2.9), on H1 [25, 28] and ZEUS [24, 27] data for different n. r_0^2 is the coefficient of linear correlation. m is the number of experimental points collected by the H1 and ZEUS Collaborations.

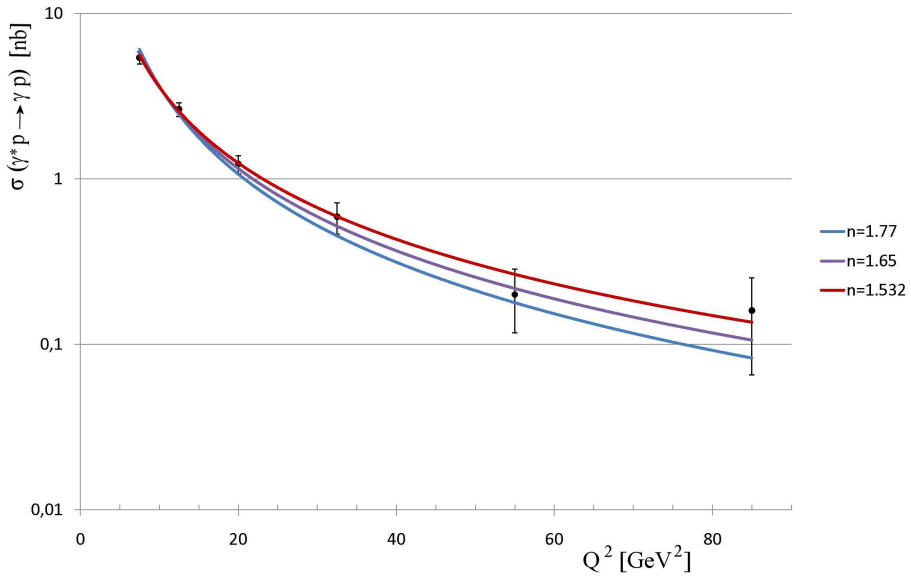

Figure 2.11: DVCS cross section $\sigma(\gamma^* p \longrightarrow \gamma p)$ as function of Q^2 for $W = 89\,\text{GeV}$ ($|t| < 1.0\,\text{GeV}^2$). The error bars represent the statistical and systematic uncertainties added in quadrature. The experimental data have been collected by the ZEUS 1996-2000 [24].

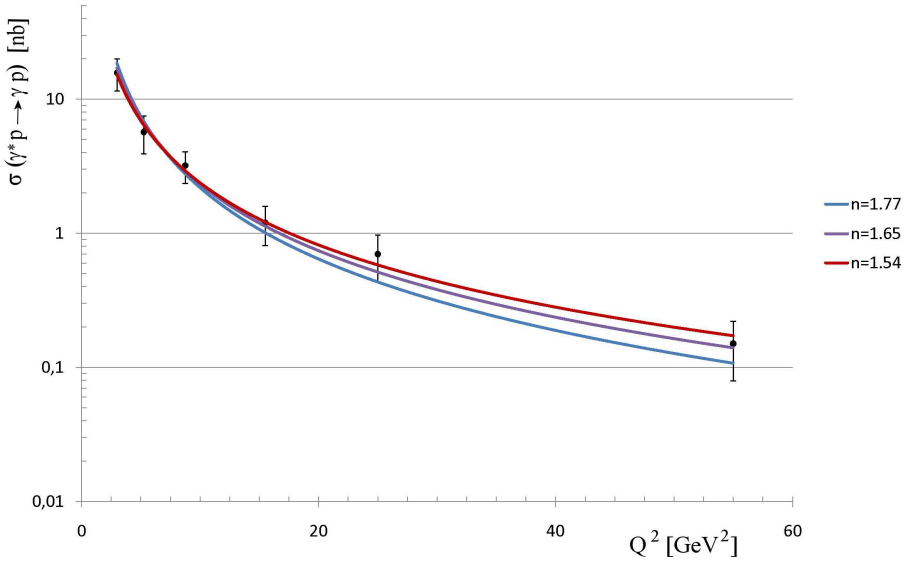

Figure 2.12: DVCS cross section $\sigma(\gamma^* p \longrightarrow \gamma p)$ as function of Q^2 for $W = 89\,\text{GeV}$ ($|t| < 1.0\,\text{GeV}^2$). The error bars represent the statistical and systematic uncertainties added in quadrature. The experimental data have been collected by the H1 1996-2000 [25].

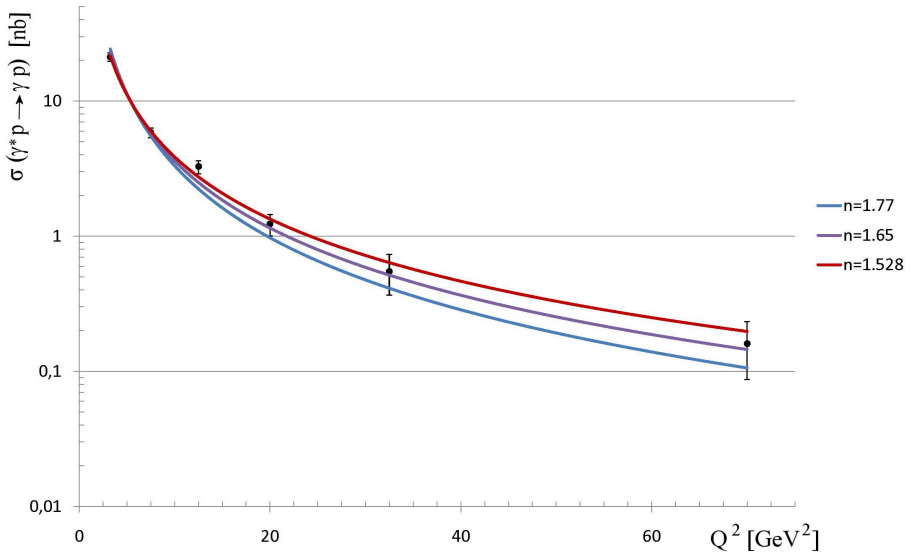

Figure 2.13: DVCS cross section $\sigma(\gamma^* p \longrightarrow \gamma p)$ as function of Q^2 for $W = 89\,\text{GeV}$ ($|t| < 1.0\,\text{GeV}^2$). The error bars represent the statistical and systematic uncertainties added in quadrature. The experimental data have been collected by the ZEUS 1999-2000 [27].

distributed. In Fig. 2.13 we represent the ZEUS [27] data and the fitting curve determined by the parameters reported in Part (d) of the Table 2.6. As Fig. 2.13 shows, in the series of measurements the third value, corresponding to $Q^2 = 12.50\,\text{GeV}^2$, is in disagreement with the others. Because this value is a suspect result, we can apply the Chauvenet's criterion [30]. Indicated with ξ the standard deviation, we find the number ν_{sus} of standard deviations by which the suspected value v_{sus} differs from that calculated by fit v_{fit}:

$$\nu_{sus} = \frac{|v_{sus} - v_{fit}|}{\xi} = \frac{|3.27 - 2.74|}{0.3013} \simeq 1.76\,. \tag{2.26}$$

The probability that a legitimate measurement would differ from v_{fit} by ν_{sus}, or more standard deviations, is[7]:

$$\begin{aligned} Prob(\text{outside } \nu_{sus}\,\xi) &= 1 - Prob(\text{within } \nu_{sus}\,\xi) \\ &= 1 - 0.9216 \\ &= 0.0784\,; \end{aligned} \tag{2.27}$$

[7] See Appendix A of [30].

multiplying by m, the total number of measurements, we have κ, the expected number as deviant as v_{sus}:

$$\begin{aligned} \kappa &= m \times Prob(\text{outside } \nu_{sus}\,\xi) \\ &= 6 \times 0.0784 \\ &\simeq 0.47\,. \end{aligned} \tag{2.28}$$

According to Chauvenet's criterion, we may reject the value $v_{sus} = 3.27\,\text{nb}$, corresponding to $Q^2 = 12.50\,\text{GeV}^2$, because κ is less than one-half. In this case, we repeat the analysis using just the remaining data and we report the results of the fits performed in Table 2.7, where we have denoted with ZEUS* the ZEUS [27] data without the point collected at $Q^2 = 12.50\,\text{GeV}^2$. As shown in the Table 2.7,

ZEUS* 1999-2000 [27], $W = 104\,\text{GeV}$ $(m^* = 5)$			
n	a	r_0^2	χ^2/d.o.f.
1.77	187.3526 ± 11.6322	0.9829	1.7539
1.65	155.7273 ± 4.1920	0.9967	0.3338
1.5278	126.8425 ± 2.1513	0.9987	0.1328
1.5711	136.7205 ± 3.4937	0.9996	0.0402

Table 2.7: Values of the parameters determined by a fit, according the Eq. (2.9), on ZEUS* data, obtained by the ZEUS [27] data without the point collected at $Q^2 = 12.50\,\text{GeV}^2$. r_0^2 is the coefficient of linear correlation. m^* is the number of experimental points used. The last line shows the best fit performed.

the fit on ZEUS* data is acceptable for $n = 1.65$. We note that the Chauvenet's criterion was used only to have an indication of the possibility of changing the n-value. Therefore in this work we adopt

$$n = 1.65\,, \tag{2.29}$$

for all used data sets [24, 25, 27, 28] (see Tables 2.1, 2.2 and 2.5). By the analysis on collected data, it seems that n is independent on W. In this manner, the standard normalization factor becomes

$$\varepsilon_{_{Q^2}} = \frac{(Q^2_{dr})^{n_{dr}}}{(Q^2_s)^{n_s}} = \frac{(4)^{1.65}}{(8)^{1.65}} = 0.3186\,. \tag{2.30}$$

2.5.2 Rescaling of data collected at different Q^2-values

By a confront of the Eq. (2.2) with the Eq. (2.25), we note that the normalization factor for fixed Q^2 is given by

$$\varepsilon^{'}_{_{Q^2}} = \varepsilon_{_{Q^2}}\, W^{(\delta_s - \delta_{dr})}\,; \tag{2.31}$$

$\varepsilon_{_{Q^2}}$ is the standard normalization factor reported in Eq. (2.30), where $n = 1.65$. In order to test whether the factor $\varepsilon^{'}_{_{Q^2}}$ rescales well the data, we carry out a comparison between the values determined by the fits on data, i.e. between the characteristic parameters of fits performed by using the power-type function of Eq. (2.9). Therefore, we build a table which shows the values of fitting curves σ_s^{fit} and σ_{dr}^{fit}, respectively determined by the fits on Q_s^2 and Q_{dr}^2 data. Through the Eq. (2.25), we obtain the σ_r^{fit} curve rescaled by using the values given by the fits on Q_s^2 and Q_{dr}^2 data, i.e. σ_s^{fit} and σ_{dr}^{fit}. Following this procedure, we can rescale the H1 [25] data collected at $Q_{dr}^2 = 4\,\mathrm{GeV}^2$ to those at $Q_s^2 = 8\,\mathrm{GeV}^2$, by building contextually the Part (a) of Table 2.5.2. The values of δ are fixed by Eq. (2.19) for the Q_s^2 and Q_{dr}^2 energies. In the last column of the Table we report the values of the $\sigma_{r,standard}^{fit}$ curve, rescaled by applying the standard procedure and adopting the standard normalization factor according to Eq. (2.23), i.e. by multiplying the factor $\varepsilon_{_{Q^2}}^{standard} = 0.3439$ for σ_{dr}^{fit}. The parameters of the σ_r^{fit} curve are[8] $c_r^* = 0.2224$ and clearly $\delta_r^* = \delta_s = 0.6935$, which is fixed. The parameters of the σ_s^{fit} curve are $c_s = 0.1797 \pm 0.0093$ and the fixed value $\delta_s = 0.6935$ ($\chi^2/\mathrm{d.o.f.} = 0.1758$); those of the σ_{dr}^{fit} curve have been reported before ($c_{dr}^* = 0.6980 \pm 0.0211$ with $\delta_{dr} = 0.5948$ fixed). The Part (a) of Table 2.8 shows that the values of standard rescaled cross section $\sigma_{r,standard}^{fit}$ differ significantly from those σ_s^{fit} in scale. In order to get an optimal rescaling procedure the ratio c_s/c_r^* should be ~ 1, but in this case it gives the value $0.1797/0.2224 \simeq 0.8081$: this diversity implies that the values of rescaled cross section σ_r^{fit} are systematically higher than those σ_s^{fit}. By setting $n = 1.65$, it is clear that only the factor $W^{(\delta_s - \delta_{dr})}$, i.e. the difference $\delta_s - \delta_{dr}$, determines the adaptation of rescaled values to those in its scale. To improve the rescaling we follow the indications of Section 2.2 (see page 2.2) and we adopt the value

[8] The error on c is negligible because this parameter refers to curve directly rescaled by a fitting curve.

$\delta = \delta_s = 0.6935$ determined by Eq. (2.19) for $Q_s^2 = 8\,\mathrm{GeV}^2$. By varying[9] δ_{dr} up to a value for which σ_r^{fit} approximates well σ_s^{fit}, we obtain $\delta_{dr} \equiv \delta_s - 0.05 = 0.6435$, i.e. $\delta(Q^2 = 4\,\mathrm{GeV}^2) = 0.6435$. The Part (b) of Table 2.8 shows the values of fitting curves σ_{dr}^{fit} and σ_r^{fit} calculated respectively by imposing $\delta_{dr} = 0.6435$ and $\delta_r = \delta_s = 0.6935$. The parameters of the σ_r^{fit} curve are[8] $c_r = 0.1820$, with

Part (a)	$Q_s^2 = 8\,\mathrm{GeV}^2$, $\delta_s = \delta_r = 0.6935$; $Q_{dr}^2 = 4\,\mathrm{GeV}^2$, $\delta_{dr} = 0.5948$						
	W [GeV]	σ_s^{fit} [nb]	σ_{dr}^{fit} [nb]	$W^{(\delta_s - \delta_{dr})}$	ε'_{Q^2}	σ_r^{fit} [nb]	$\sigma_{r,standard}^{fit}$ [nb]
	45	2.52 ± 0.14	6.71 ± 0.21	1.46	0.46	3.12 ± 0.09	2.31 ± 0.07
	70	3.42 ± 0.18	8.73 ± 0.26	1.52	0.48	4.23 ± 0.13	3.00 ± 0.09
	90	4.07 ± 0.21	10.14 ± 0.30	1.56	0.50	5.04 ± 0.15	3.49 ± 0.11
	110	4.68 ± 0.25	11.42 ± 0.34	1.59	0.51	5.79 ± 0.18	3.93 ± 0.12
	130	5.26 ± 0.28	—	—	—	—	—
Part (b)	$Q_s^2 = 8\,\mathrm{GeV}^2$, $\delta_s = \delta_r = 0.6935$; $Q_{dr}^2 = 4\,\mathrm{GeV}^2$, $\delta_{dr} = 0.6435$						
	W [GeV]	σ_s^{fit} [nb]	σ_{dr}^{fit} [nb]	$W^{(\delta_s - \delta_{dr})}$	ε'_{Q^2}	σ_r^{fit} [nb]	$\sigma_{r,standard}^{fit}$ [nb]
	45	2.52 ± 0.14	6.62 ± 0.18	1.21	0.39	2.55 ± 0.07	2.31 ± 0.07
	70	3.42 ± 0.18	8.79 ± 0.24	1.24	0.39	3.47 ± 0.10	3.00 ± 0.09
	90	4.07 ± 0.21	10.34 ± 0.28	1.25	0.40	4.13 ± 0.11	3.49 ± 0.11
	110	4.68 ± 0.25	11.76 ± 0.32	1.27	0.40	4.74 ± 0.13	3.93 ± 0.12
	130	5.26 ± 0.28	—	—	—	—	—

Table 2.8: Table used to test the proposed rescaling procedure, applied on the data collected by H1 1996-2000 [25], and to define the behaviour of δ-parameter. The errors due to δ are neglected in estimate of cross sections.

$\delta_r = \delta_s = 0.6935$ fixed. In this case $c_s/c_r = 0.1797/0.1820 \simeq 0.9874 \sim 1$ for which the procedure introduced here is functional. We can appreciate graphically the effects of the procedure in the Fig. 2.14 where we have represented the fitting curves σ_s^{fit} and σ_r^{fit}, the data in scale and those rescaled by using the Eq. (2.25) and setting $\delta_r = \delta_s = 0.6935$, $\delta_{dr} = 0.6435$. The Fig. 2.15 shows the H1 [28] data collected at $Q^2 = 8\,\mathrm{GeV}^2$, $15.5\,\mathrm{GeV}^2$ and $25\,\mathrm{GeV}^2$. By adopting the power-type function of Eq. (2.22), two fits were performed on each data set: the first one was

[9] Here we choose to vary δ_{dr} because we note that in a neighborhood of $Q^2 = 8\,\mathrm{GeV}^2$ the δ function takes a value approximately constant, compatible to the experimental data within the errors (see Figure 2.7).

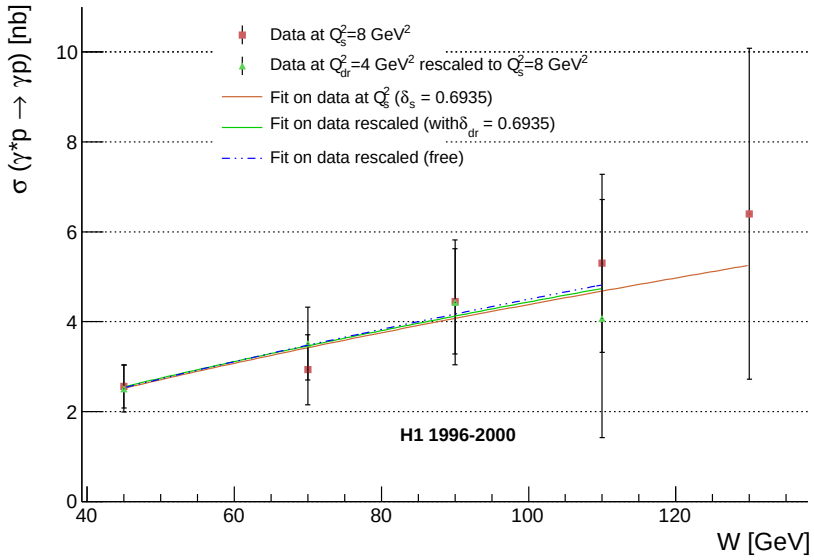

Figure 2.14: DVCS cross section $\sigma(\gamma^* p \longrightarrow \gamma p)$ as function of W for $Q^2 = 8\,\mathrm{GeV}^2$ ($|t| < 1.0\,\mathrm{GeV}^2$). The error bars represent the statistical and systematic uncertainties added in quadrature. The experimental data [25] collected at $Q^2 = 4\,\mathrm{GeV}^2$ have been rescaled to those collected at $Q^2 = 8\,\mathrm{GeV}^2$ using the normalization factor ε'_{Q^2} determined by Eq. (2.31), with $n = 1.65$, and the procedure reported in Subsection 2.5.2.

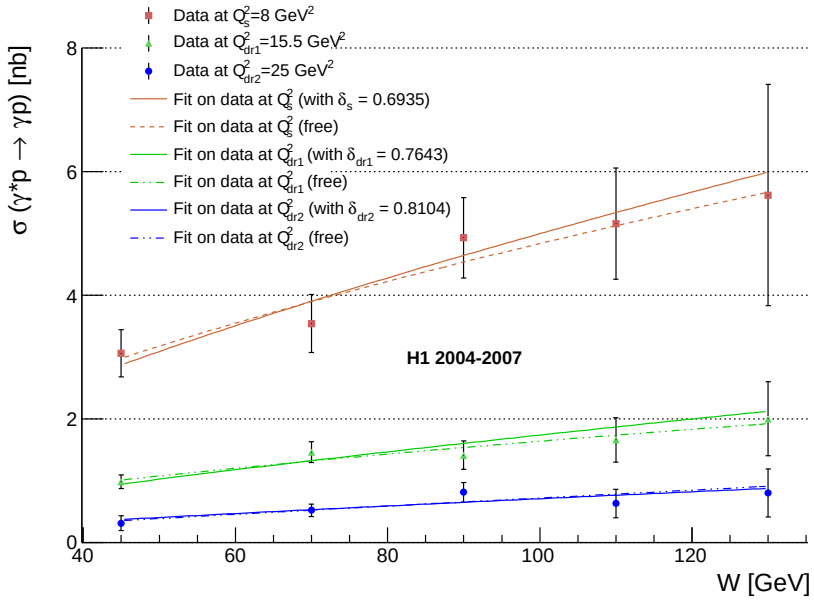

Figure 2.15: DVCS cross section $\sigma(\gamma^* p \longrightarrow \gamma p)$ as function of W for fixed values of Q^2 ($|t| < 1.0\,\mathrm{GeV}^2$). The error bars represent the statistical and systematic uncertainties added in quadrature. The experimental data are collected by the H1 Collaboration [28]. Two fits are performed on each data set by adopting the power-type function of Eq. (2.22), i.e. $\sigma(W) = c \times W^{\delta(Q^2)}$.

performed leaving free all parameters (dotted lines), the second one by setting δ-parameter to the value determined by the Eq. (2.19) (full lines). Below we consider to rescale the data collected at $Q^2 = 15.5\,\mathrm{GeV}^2$ and $Q^2 = 25\,\mathrm{GeV}^2$ to those collected at $Q^2 = 8\,\mathrm{GeV}^2$.

2.5.3 Rescaling of data collected at $Q^2_{dr} = 15.5\,\mathbf{GeV}^2$ to those at $Q^2_s = 8\,\mathbf{GeV}^2$

Following the same steps used above, we build the Part (a) of Table 2.5.3, which shows the values of fitting curves σ_s^{fit} and σ_{dr}^{fit} determined by the fits performed respectively on data collected at $Q^2_s = 8\,\mathrm{GeV}^2$ and those collected at $Q^2_{dr} = 15.5\,\mathrm{GeV}^2$. According to Eq. (2.19) $\delta_s = 0.6935$ and $\delta_{dr} = 0.7643$. By using the

	$Q^2_s = 8\,\mathrm{GeV}^2$, $\delta_s = \delta_r = 0.6935$; $Q^2_{dr} = 15.5\,\mathrm{GeV}^2$, $\delta_{dr} = 0.7643$						
Part (a)	W [GeV]	σ_s^{fit} [nb]	σ_{dr}^{fit} [nb]	$W^{(\delta_s-\delta_{dr})}$	ε'_{Q^2}	σ_r^{fit} [nb]	$\sigma_{r,standard}^{fit}$ [nb]
	45	2.87 ± 0.10	0.94 ± 0.04	0.76	2.27	2.15 ± 0.10	2.69 ± 0.10
	70	3.90 ± 0.14	1.32 ± 0.06	0.74	2.21	2.92 ± 0.13	3.66 ± 0.14
	90	4.64 ± 0.16	1.60 ± 0.07	0.73	2.17	3.47 ± 0.16	4.36 ± 0.17
	110	5.34 ± 0.19	1.87 ± 0.08	0.72	2.14	3.99 ± 0.18	5.01 ± 0.19
	130	5.99 ± 0.21	2.12 ± 0.10	0.71	2.11	4.48 ± 0.20	5.62 ± 0.22
	$Q^2_s = 8\,\mathrm{GeV}^2$, $\delta_s = \delta_r = 0.6935$; $Q^2_{dr} = 15.5\,\mathrm{GeV}^2$, $\delta_{dr} = 0.6935 = \delta_s$						
Part (b)	W [GeV]	σ_s^{fit} [nb]	σ_{dr}^{fit} [nb]	$W^{(\delta_s-\delta_{dr})}$	ε'_{Q^2}	σ_r^{fit} [nb]	$\sigma_{r,standard}^{fit}$ [nb]
	45	2.87 ± 0.10	0.97 ± 0.04	1.00	2.98	2.90 ± 0.11	2.69 ± 0.10
	70	3.90 ± 0.14	1.32 ± 0.05	1.00	2.98	3.94 ± 0.15	3.66 ± 0.14
	90	4.64 ± 0.16	1.57 ± 0.06	1.00	2.98	4.69 ± 0.18	4.36 ± 0.17
	110	5.34 ± 0.19	1.81 ± 0.07	1.00	2.98	5.39 ± 0.21	5.01 ± 0.19
	130	5.99 ± 0.21	2.03 ± 0.08	1.00	2.98	6.05 ± 0.23	5.62 ± 0.22

Table 2.9: Table used to test the proposed rescaling procedure, applied on the data collected by H1 2004-2007 [28], and to define the behaviour of δ-parameter. The errors due to δ are neglected in estimate of cross sections.

Eq. (2.25), we obtain the σ_r^{fit} curve rescaled by the values given by the fits and not by measurements. We note that the values of σ_r^{fit} do not approximate the values of σ_s^{fit}. In particular, the difference $\delta_s - \delta_{dr}$ means that the factor $W^{\delta_s-\delta_{dr}}$

changes, ranging from ~ 0.71 to ~ 0.76, and therefore there is a significant change in the factor ε'_{Q^2}. By varying[9] δ_{dr} so that $W^{\delta_s-\delta_{dr}} \simeq 1$, i.e. by setting $\delta_s - \delta_{dr} \simeq 0$, we have that σ_r^{fit} approximates σ_s^{fit} very well, as shown in Part (b) of Table 2.5.3. Hence the trend $\delta(Q^2)$ must be changed. We assume that the δ-parameter has a flattening already around at $Q^2 = 8\,\mathrm{GeV}^2$ and we suggest that $\delta(Q^2 = 15.5\,\mathrm{GeV}^2) \simeq \delta(Q^2 = 8\,\mathrm{GeV}^2) \simeq 0.6935$. In the last column of Table 2.9 we report the values of the $\sigma^{fit}_{r,standard}$ curve rescaled by applying the standard procedure and adopting the standard normalization factor according to Eq. (2.23), i.e. by multiplying the factor $\varepsilon^{standard}_{Q^2} = (15.5)^{1.54}/(8)^{1.54} \simeq 2.7692$ for σ^{fit}_{dr}. The parameters of the σ_r^{fit} curve are[8] $c_r = 0.2068$ with $\delta_r = \delta_s = 0.6935$ fixed; the characteristic parameters of the fit on data collected at $Q_s^2 = 8\,\mathrm{GeV}^2$ are $c_s = 0.2049 \pm 0.0073$ (χ^2/d.o.f. $= 0.3258$) with $\delta_s = 0.6935$ fixed. In this case $c_s/c_r = 0.2049/0.2068 \simeq 0.9908 \sim 1$ for which the procedure is optimal.

2.5.4 Rescaling of data collected at $Q^2_{dr} = 25\,\mathbf{GeV}^2$ to those at $Q^2_s = 8\,\mathbf{GeV}^2$

According to the Eq. (2.19) and previous considerations, we may assume the flattening of δ at high Q^2. Thereby, to rescale data collected at $Q^2_{dr} = 25\,\mathrm{GeV}^2$ to those collected at $Q^2_s = 8\,\mathrm{GeV}^2$, we expect that $\delta_{dr} \simeq \delta_s = 0.6935$. In this manner the factor $W^{\delta_s-\delta_{dr}} \simeq 1$ determines that the σ_r^{fit} curve is systematically lower compared to σ_s^{fit} curve, as the Part (a) of Table 2.5.5 shows. In particular, to improve the rescaling, the behavior of δ-parameter must be changed for high values of Q^2, so that with $W^{\delta_s-\delta_{dr}} > 1$ we obtain $\sigma_r^{fit} \simeq \sigma_s^{fit}$. By assuming $\delta_{dr} = \delta_s - 0.025$, i.e. $\delta(Q^2 = 25\,\mathrm{GeV}^2) = 0.6685$, σ_r^{fit} approximates well σ_s^{fit}, as shown in Part (b) of Table 2.5.5. In the last column we report the values of the $\sigma^{fit}_{r,standard}$ curve rescaled by applying the standard procedure and adopting the standard normalization factor according to Eq. (2.23), i.e. by multiplying the factor $\varepsilon^{standard}_{Q^2} = (25)^{1.54}/(8)^{1.54} \simeq 5.7819$ for σ^{fit}_{dr}. The parameters of the σ_r^{fit} curve are[8] $c_r = 0.2046$ with $\delta_r = \delta_s = 0.6935$ fixed; the characteristic parameters of the fit on data collected at $Q_s^2 = 8\,\mathrm{GeV}^2$ are $c_s = 0.2049 \pm 0.0073$ (χ^2/d.o.f. $=$ 0.3258) with $\delta_s = 0.6935$ fixed. In this case $c_s/c_r = 0.2049/0.2046 \simeq 1.0015 \sim 1$ for which the procedure is optimal. We can appreciate graphically the effects

of the procedure of proposed rescaling in Fig. 2.16, where we have represented the fitting curves σ_s^{fit} and σ_r^{fit}, reported in Parts (b) of Tables 2.5.3 and 2.5.5, and the data in scale and those rescaled by using the Eq. (2.25) and setting $\delta_s = \delta(Q^2 = 8\,\mathrm{GeV}^2) = 0.6935$, $\delta_{dr1} = \delta(Q^2 = 15.5\,\mathrm{GeV}^2) = \delta_s$ and $\delta_{dr2} = \delta(Q^2 = 25\,\mathrm{GeV}^2) = 0.6685$. We can compare the data presented in Fig. 2.16 with those in Fig. 2.17, where we have applied the rescaling according to standard procedure; we note that, using ε'_{Q^2} normalization factor and changing the δ-behaviour as indicated above, the new procedure, respect to standard, is more appropriate to rescale the data in a functional way to perform statistical analysis.

2.5.5 Rescaling of data collected at $Q^2_{dr} = 25\,\mathbf{GeV}^2$ to those at $Q^2_s = 15.5\,\mathbf{GeV}^2$

To test whether the values of δ determined above are compatible with other rescaling of data, we consider the case in which the data are rescaled from $Q^2_{dr} = 25\,\mathrm{GeV}^2$ to $Q^2_s = 15.5\,\mathrm{GeV}^2$. By setting $\delta_s = \delta(Q^2 = 15.5\,\mathrm{GeV}^2) = 0.6935$ and $\delta_{dr} = \delta(Q^2 = 25\,\mathrm{GeV}^2) = 0.6685$, we build the Table 2.11 which shows that the values of σ_r^{fit} curve approximate well the values of σ_s^{fit} curve. The parameters of the σ_r^{fit} curve are[8] $c_r = 0.0687$ with $\delta_r = \delta_s = 0.6935$ fixed; the characteristic parameters of the fit on data collected at $Q^2_s = 15.5\,\mathrm{GeV}^2$ are $c_s = 0.0694 \pm 0.0027$ ($\chi^2/\mathrm{d.o.f.} = 0.3321$) with $\delta_s = 0.6935$ fixed. In this case $c_s/c_r = 0.0694/0.0687 \simeq 1.0102 \sim 1$ for which the procedure is optimal. In the last column of Table 2.11 we report the values of the $\sigma^{fit}_{r,standard}$ curve rescaled by applying the standard procedure and adopting the standard normalization factor according to Eq. (2.23), i.e. by multiplying the factor $\varepsilon^{standard}_{Q^2} = (25)^{1.54}/(15.5)^{1.54} \simeq 2.0879$ for σ^{fit}_{dr}.

2.6 The δ-parameter

From considerations of Section 2.5 we can build the following Table 2.12. We can consider the behaviour of δ by comparing the data of Table 2.12 with the values experimentally obtained and listed in Table 2.3 of Section 2.4. It is highly probable that δ has a strongly growing behavior for low Q^2-values (i.e. for $Q^2 < 4\,\mathrm{GeV}^2$), constant for $8\,\mathrm{GeV}^2 < Q^2 < 15.5\,\mathrm{GeV}^2$ and slightly decreasing for $Q^2 >$

	$Q_s^2 = 8\,\mathrm{GeV}^2$, $\delta_s = \delta_r = 0.6935$; $Q_{dr}^2 = 25\,\mathrm{GeV}^2$, $\delta_{dr} = 0.6935 = \delta_s$						
Part (a)	W [GeV]	σ_s^{fit} [nb]	σ_{dr}^{fit} [nb]	$W^{(\delta_s - \delta_{dr})}$	ε'_{Q^2}	σ_r^{fit} [nb]	$\sigma_{r,standard}^{fit}$ [nb]
	45	2.87 ± 0.10	0.40 ± 0.03	1.00	6.55	2.57 ± 0.22	2.30 ± 0.19
	70	3.90 ± 0.14	0.53 ± 0.05	1.00	6.55	3.50 ± 0.30	3.09 ± 0.26
	90	4.64 ± 0.16	0.63 ± 0.05	1.00	6.55	$4.16 \pm 0,35$	3.66 ± 0.31
	110	5.34 ± 0.19	0.72 ± 0.06	1.00	6.55	4.78 ± 0.40	4.18 ± 0.35
	130	5.99 ± 0.21	0.80 ± 0.07	1.00	6.55	5.37 ± 0.45	4.67 ± 0.39
	$Q_s^2 = 8\,\mathrm{GeV}^2$, $\delta_s = \delta_r = 0.6935$; $Q_{dr}^2 = 25\,\mathrm{GeV}^2$, $\delta_{dr} = 0.6685$						
Part (b)	W [GeV]	σ_s^{fit} [nb]	σ_{dr}^{fit} [nb]	$W^{(\delta_s - \delta_{dr})}$	ε'_{Q^2}	σ_r^{fit} [nb]	$\sigma_{r,standard}^{fit}$ [nb]
	45	2.87 ± 0.10	0.40 ± 0.03	1.10	7.21	2.87 ± 0.24	2.30 ± 0.19
	70	3.90 ± 0.14	0.53 ± 0.05	1.11	7.29	3.89 ± 0.33	3.09 ± 0.26
	90	4.64 ± 0.16	0.63 ± 0.05	1.12	7.33	4.64 ± 0.39	3.66 ± 0.31
	110	5.34 ± 0.19	0.72 ± 0.06	1.13	7.37	5.33 ± 0.45	4.18 ± 0.35
	130	5.99 ± 0.21	0.80 ± 0.07	1.13	7.40	5.99 ± 0.50	4.67 ± 0.39

Table 2.10: Table used to test the proposed rescaling procedure, applied on the data collected by H1 2004-2007 [28], and to define the behaviour of δ-parameter. The errors due to δ are neglected in estimate of cross sections.

$Q_s^2 = 15.5\,\mathrm{GeV}^2$, $\delta_s = \delta_r = 0.6935$; $Q_{dr}^2 = 25\,\mathrm{GeV}^2$, $\delta_{dr} = 0.6685$						
W [GeV]	σ_s^{fit} [nb]	σ_{dr}^{fit} [nb]	$W^{(\delta_s - \delta_{dr})}$	ε'_{Q^2}	σ_r^{fit} [nb]	$\sigma_{r,standard}^{fit}$ [nb]
45	0.97 ± 0.04	0.40 ± 0.03	1.10	2.42	0.96 ± 0.08	0.83 ± 0.07
70	1.32 ± 0.05	0.53 ± 0.05	1.11	2.45	1.31 ± 0.11	1.12 ± 0.09
90	1.57 ± 0.06	0.63 ± 0.05	1.12	2.46	1.56 ± 0.13	1.32 ± 0.11
110	1.81 ± 0.07	0.72 ± 0.06	1.13	2.48	1.79 ± 0.15	1.51 ± 0.13
130	2.03 ± 0.08	0.81 ± 0.07	1.13	2.49	2.01 ± 0.17	1.69 ± 0.14

Table 2.11: Table used to test the proposed rescaling procedure, applied on the data collected by H1 2004-2007 [28], and to define the behaviour of δ-parameter. The errors due to δ are neglected in estimate of cross sections.

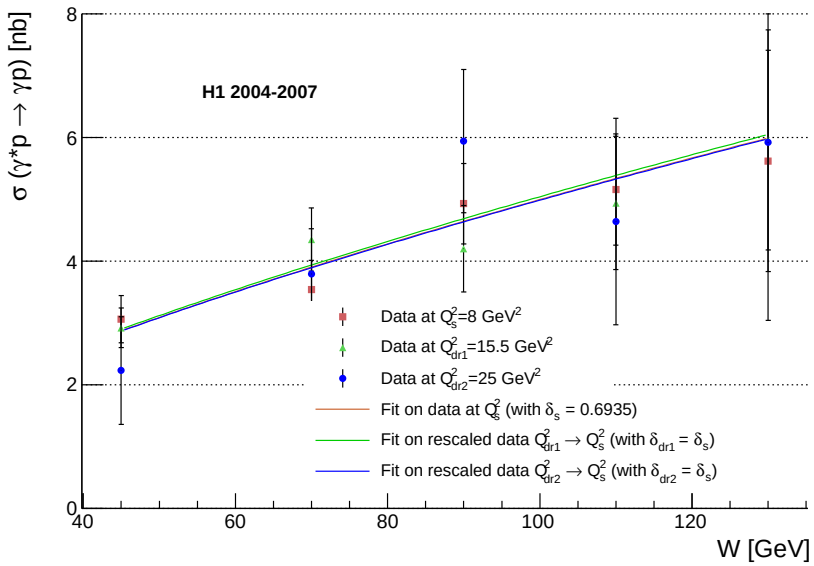

Figure 2.16: DVCS cross section $\sigma(\gamma^* p \longrightarrow \gamma p)$ as function of W for $Q^2 = 8\,\mathrm{GeV}^2$ ($|t| < 1.0\,\mathrm{GeV}^2$). The error bars represent the statistical and systematic uncertainties added in quadrature. The experimental data [28] collected at $Q^2 = 15.5\,\mathrm{GeV}^2$ and $Q^2 = 25\,\mathrm{GeV}^2$ have been rescaled to those collected at $Q^2 = 8\,\mathrm{GeV}^2$ using the normalization factor ε'_{Q^2} determined by Eq. (2.31), with $n = 1.65$, and the procedure reported in Subsections 2.5.3 and 2.5.4.

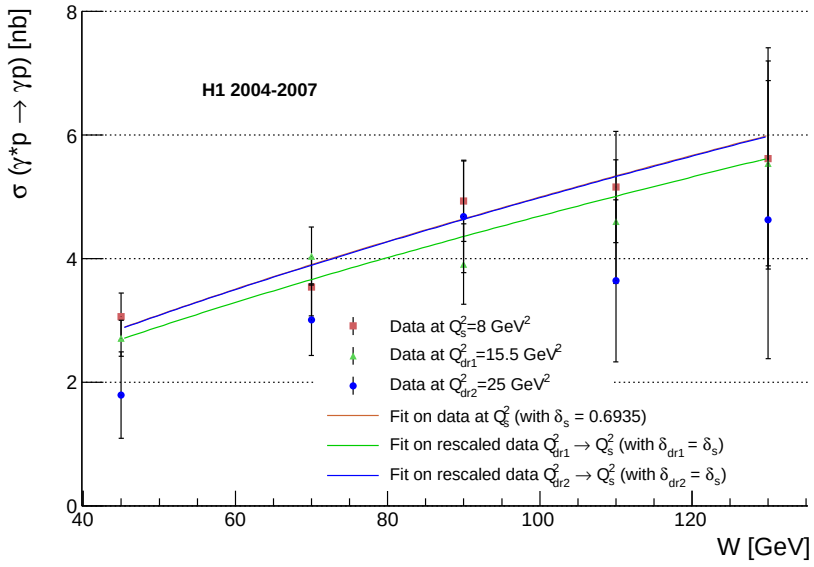

Figure 2.17: DVCS cross section $\sigma(\gamma^* p \longrightarrow \gamma p)$ as function of W for $Q^2 = 8\,\mathrm{GeV}^2$ ($|t| < 1.0\,\mathrm{GeV}^2$). The error bars represent the statistical and systematic uncertainties added in quadrature. The experimental data [25] collected at $Q^2 = 4\,\mathrm{GeV}^2$ have been rescaled to those collected at $Q^2 = 8\,\mathrm{GeV}^2$ using the standard rescaling procedure.

Q^2 [GeV^2]	δ	Subsec.
4	0.6435	2.5.2
8	0.6935	2.5.3
15.5	0.6935	2.5.4
25	0.6685	2.5.5

Table 2.12: The δ values determined by the analysis conducted in Section 2.5, by using the new *rescaling* procedure. The last column gives the references to Subsections where δ-values are calculated.

15.5 GeV^2. Such behavior may be attributed to a function like the following:

$$\delta(Q^2) = \delta_1^{'} \left(Q^2\right)^{-n'} e^{-\delta_2^{'}\left(Q^2\right)^{-n'}}, \tag{2.32}$$

where the constants $\delta_i^{'}$ $(i = 1, 2)$ and n' are calculated by performing a fit[10] on data of Table 2.12. By introducing Q_0^2 and putting $\delta_i^{'} = (Q_0^2)^{n'} \times \delta_i$ $(i = 1, 2)$, the expression of Eq. (2.32) can be reformulated in the following form:

$$\delta(Q^2) = \delta_1 \left(Q_0^2/Q^2\right)^{n'} e^{-\delta_2\left(Q_0^2/Q^2\right)^{n'}}, \tag{2.33}$$

where $Q_0^2 \equiv 0.025\,\text{GeV}^2$. In this case, a fit on data of Table 2.12 gives the values $\delta_1 = 18.9773 \pm 0.3238$, $\delta_2 = 9.9889 \pm 0.1654$ and $n' = 0.3784 \pm 0.0029$ (χ^2/d.o.f. $= 2.89 \times 10^{-7}$). Figure 2.18 shows the fitting curve obtained by form of Eq. (2.33). The *reduced chi-square* (on only experimental data shown in figure) returns a value of 0.0269, so the curve is well adapted to the experimental points. It is interesting to understand the behavior of the parameter δ as function of Q^2.

2.7 A picture for DVCS

In this Section we focus on the form dependent of W of the integrated cross section, reported in Eq. (2.1), i.e. we consider only the following factorized part:

$$\sigma(W) \propto W^{\delta(Q^2)}. \tag{2.34}$$

Denoted by p and q respectively the four-momenta of the incoming proton and the virtual photon, the energy of the center of mass of the proton-virtual photon

[10]The fit was performed with *GnuPlot* [34], which provides the values $\delta_1^{'} = 4.6986 \pm 0.0305$, $\delta_2^{'} = 2.4731 \pm 0.0149$ and $n' = 0.3784 \pm 0.0029$ (χ^2/d.o.f. $= 2.89 \times 10^{-7}$).

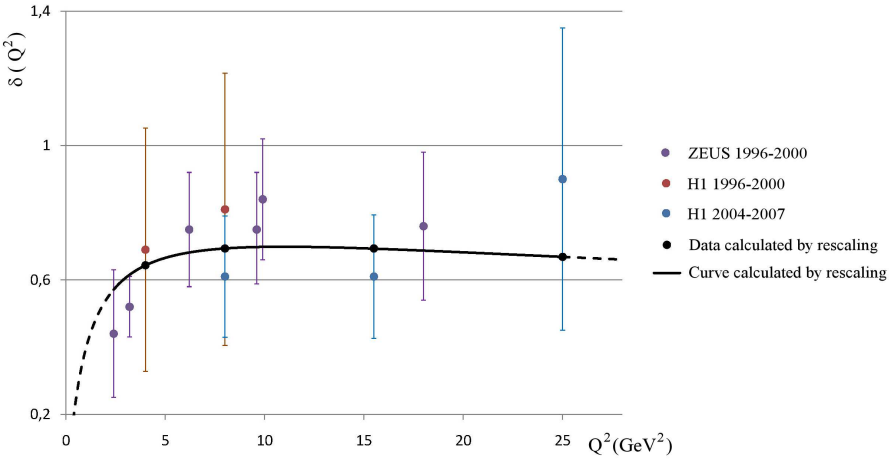

Figure 2.18: δ-parameter as function of Q^2. The experimental values are reported in Table 2.3. The black circles indicate the values calculated by new rescaling procedure and listed in Table 2.12. The black curve shows the function given by (2.33).

system is given by $W = p + q$. As already seen in the Section 1.6, also for the DVCS process the proton emerges with a value of its four-momentum slightly changed (t-small), while the electron receives a large transferred four-momentum, i.e. the values of virtuality $Q^2 = -q^2$ are not negligible respect to the squared four-momenta of the incoming and outgoing electrons. Denoted by $x = Q^2/(2p\cdot q)$ the Bjorken variable, we have that[11]

$$W^2 = (q+p)^2 \simeq 2\,p\cdot q + q^2 = 2\,p\cdot q - Q^2 = 2\,p\cdot q\,(1-x)\,; \tag{2.35}$$

by previous equation and considering that from the data collected by the various Collaborations $W^2 \gg Q^2$ for low Q^2-values specially, we have

$$2\,p\cdot q \simeq W^2 + Q^2 = W^2\left(1 + \frac{Q^2}{W^2}\right) \simeq W^2\,. \tag{2.36}$$

Therefore, the Eq. (2.35) and Eq. (2.36) give

$$x = \frac{Q^2}{2p\cdot q} \simeq \frac{Q^2}{W^2} \ll 1\,. \tag{2.37}$$

In the interaction the virtual photon γ^* does not act only as a point particle which couples directly to constituents of matter (*direct photon*), but γ^* can split into a quark-antiquark pair (*resolved photon*), who takes part in the hard subprocess (see Section 1.4). It's clear that for low Q^2 the virtual photon is not resolved

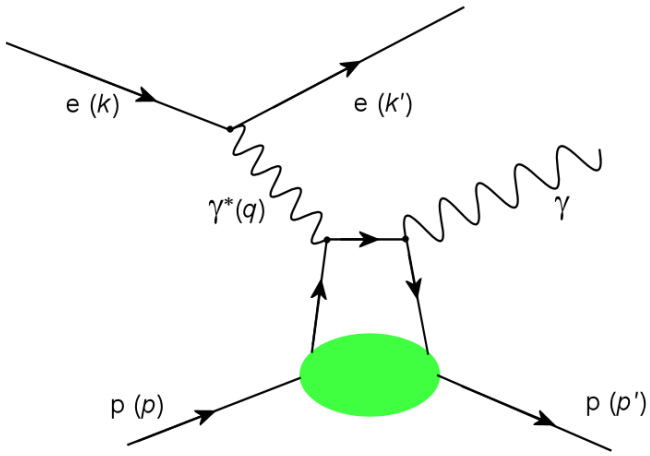

Figure 2.19: DVCS diagram $e(k)+p(p) \longrightarrow e(k')+\gamma(q')+p(p')$ in the QCD in LO (Q^2 very low).

and directly it probes a parton constituent the proton (see Figure 2.19). When Q^2 reaches a certain value (x not very small), the virtual photon fluctuates in a quark-antiquark pair (the so-called colour dipole), through whom it interacts with the partons by the emission/absorption of a pair of gluons (see Figure 2.20); through colour dipole, the virtual photon sees the pair of gluons with reduced momentum. By increasing further Q^2 ($x \geq 0.1$), the colour dipole not sees just a pair of gluons emitted from the proton, but also other secondary gluons (see Figure 2.21). At W fixed, the factorized part $\sigma(W)$, as function of Q^2, implies a strongly growing trend for $x \ll 1$, a flat trend for x not very small and a decreasing trend for $x \geq 0.1$. This behavior is in agreement with that of the structure function $F_2(x, Q^2)$ of the proton, whereby the trend of the δ-parameter is consistent with the *Parton Model* in QCD. In fact, in DIS the inelastic cross section takes the form[12]

$$\frac{d\sigma}{dxdQ^2} \propto \frac{4\pi\alpha^2}{xQ^4} F_2\left(x, Q^2\right) , \tag{2.38}$$

which mainly depends on F_2; experimentally it has been found that, for lowest values of x, F_2 increases with Q^2, while, for highest values of x, F_2 decreases. This trend is called *violation of scale invariance* (see Figure 2.22). Therefore, the behavior of $\sigma(W)$ is in agreement with that of F_2, justifying the trend of

[11] See Eq. (B.8) and the Appendix B.1.
[12] See Chapter 1 of [17].

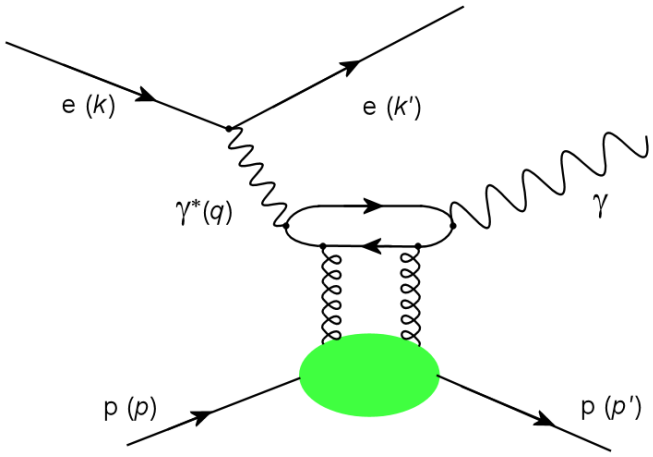

Figure 2.20: DVCS diagram $e(k)+p(p) \longrightarrow e(k')+\gamma(q')+p(p')$ in the QCD in NLO (Q^2 not very small).

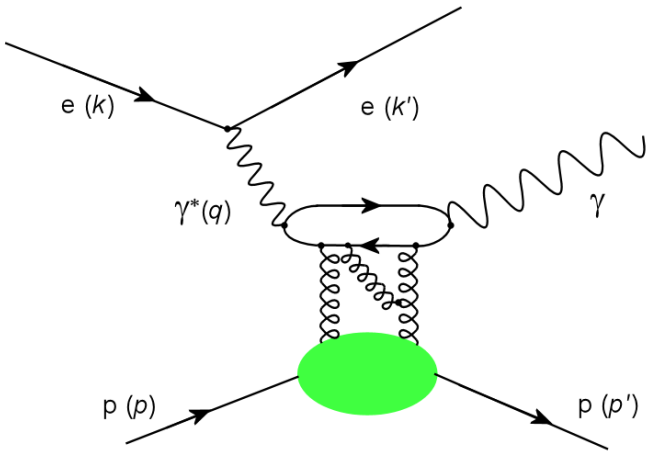

Figure 2.21: DVCS diagram $e(k)+p(p) \longrightarrow e(k')+\gamma(q')+p(p')$ with which it is outlined the possibility that, for Q^2 sufficiently high, the pair of primary gluons generates secondary gluons. The line of secondary gluon is representative of a multitude of secondary gluons.

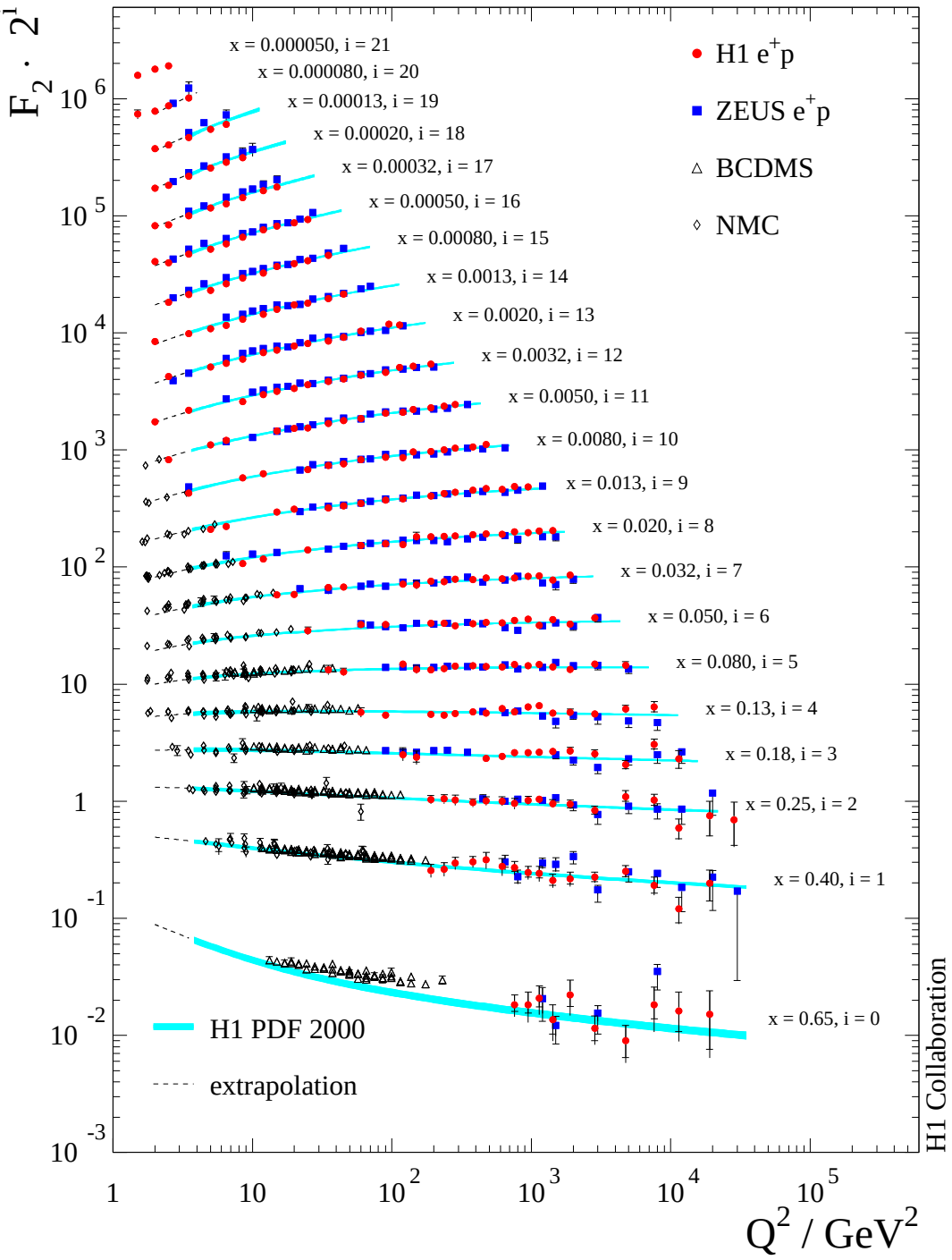

Figure 2.22: Trend of F_2 as function of Q^2 for different x-values. The data are compared with the results obtained in the framework of QCD [35].

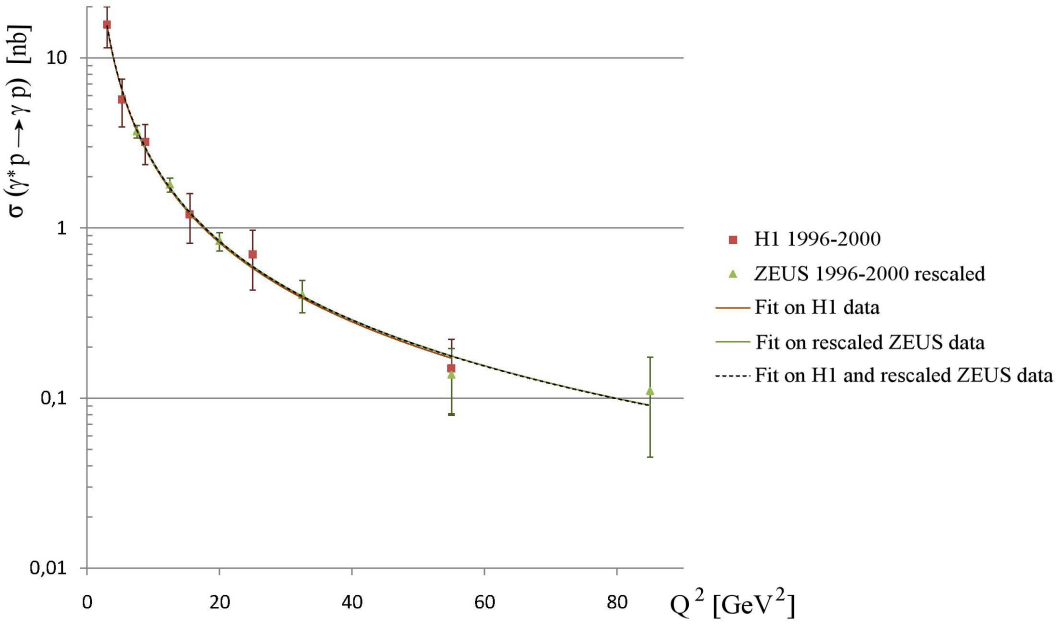

Figure 2.23: DVCS cross section $\sigma(\gamma^* p \longrightarrow \gamma p)$ as function of Q^2 for $W = 82\,\text{GeV}$ ($|t| < 1.0\,\text{GeV}^2$). The error bars represent the statistical and systematic uncertainties added in quadrature. The experimental data collected by the ZEUS Collaboration [24] have been rescaled to those collected by the H1 Collaboration [25] using the normalization factor $\varepsilon_W^{'}$, given by Eq. (2.21), and the form of Eq. (2.33) for δ-parameter.

δ-parameter proposed in this work.

2.8 Rescaling for W fixed

By using the form of Eq. (2.33) for $\delta(Q^2)$, the new normalization factor for fixed W, $\varepsilon_W^{'}$, well rescales ZEUS data [24] to those of H1 [25], as shown in Figure 2.23. By adopting the same power-type function $\sigma(Q^2) = a(1/Q^2)^n$ and leaving all parameters free, fits were performed on the H1 and rescaled ZEUS data and on overall data set. In particular, the fit on H1 data (brown curve) gives $a_s = 83.466 \pm 10.959$ and $n_s = 1.5437 \pm 0.0558$ (χ^2/d.o.f. $= 0.1455$), the fit on rescaled ZEUS data (green curve) gives $a_r = 83.349 \pm 9.5708$ e $n_r = 1.5361 \pm 0.0450$ (χ^2/d.o.f. $= 0.2087$), the fit on overall data (black dotted curve) gives $a = 83.344 \pm 6.3815$ e $n = 1.5369 \pm 0.0303$ (χ^2/d.o.f. $= 0.1432$).

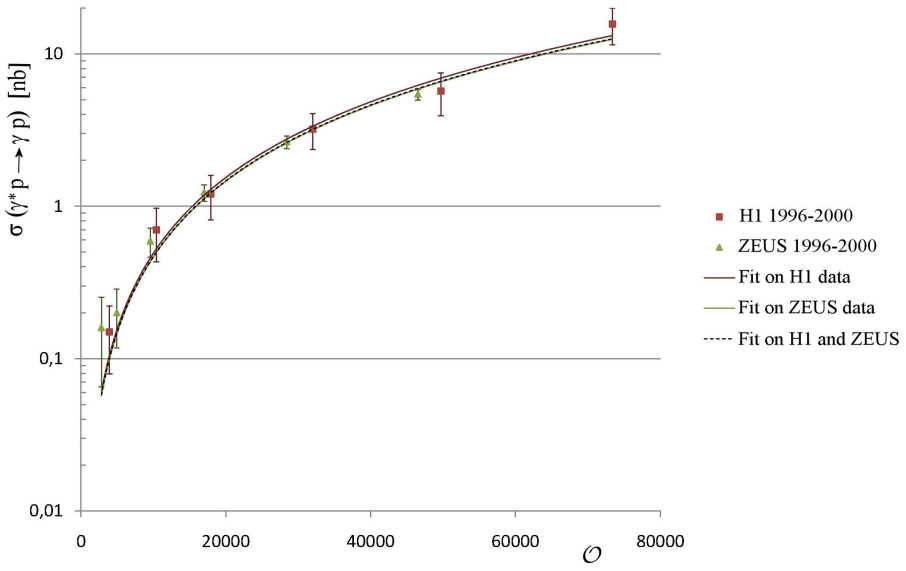

Figure 2.24: DVCS cross section $\sigma(\gamma^* p \longrightarrow \gamma p)$ [24, 25] as function of $\mathcal{O}$ (fixed W, $|t| < 1.0\,\mathrm{GeV}^2$). The error bars represent the statistical and systematic uncertainties added in quadrature.

2.9 A "normal" form for cross section

By introducing the variable

$$\mathcal{O} \equiv \frac{1}{Q^2}\, W^{\left[4+\delta(Q^2)\right]/n}\,, \tag{2.39}$$

the cross sections assume the following form for fixed W:

$$\sigma(\mathcal{O}) \equiv \mathcal{C}\,\mathcal{O}^n\,; \tag{2.40}$$

In Figure 2.24 the cross sections are presented as functions of the scale denoted by $\mathcal{O}$. By adopting the function of Eq. (2.40), a fit (with $n = 1.65$ fixed) was performed on H1 [25] and ZEUS [24] data and on overall data set. We obtain $a_s = (1.2338 \pm 0.0960) \times 10^{-7}$ (χ^2/d.o.f. $= 0.3476$) for H1 data, $a_{dr} = (1.1660 \pm 0.0607) \times 10^{-7}$ (χ^2/d.o.f. $= 0.9778$) for ZEUS data and $a = (1.1744 \pm 0.0451) \times 10^{-7}$ (χ^2/d.o.f. $= 0.6163$) for overall data set. From parameters calculated by the fits on H1 and ZEUS data, we have the ratio

$$\frac{\mathcal{C}_s}{\mathcal{C}_{dr}} \simeq 1.06 \sim 1\,, \tag{2.41}$$

i.e. $\mathcal{C}_{dr} \simeq \mathcal{C}_s$. Therefore the scale $\mathcal{O}$ normalizes the DVCS cross sections.

Chapter 3

Building a new Model

In this chapter we report the data used for the analysis conducted in order to construct a phenomenological model. By examining these data and taking into account the findings in the previous chapter, we determine the trends of the parameters here introduced.

3.1 The differential cross section for DVCS

As reported in Chapter 2, the Eq. (2.1) states that the DVCS cross section has been measured as a function of Q^2 and W, that are respectively the photon virtuality and the invariant mass of the γ^*p system. In Section 1.2, we have indicated that the cross-section has measured also as a differential function on t, that is the squared transferred four momentum at the nucleon vertex. The t-dependence of the DVCS cross section is found to be well approximated by the exponential form of Eq. (3.1), that we report here:

$$\frac{d\sigma}{dt} = \left.\frac{d\sigma}{dt}\right|_{t=0} e^{Bt}. \tag{3.1}$$

B is a parameter determined by fit on experimental data and therefore it is function of Q^2 and W; the multiplication factor $d\sigma/dt|_{t=0}$ can be dependent only on Q^2 and W. Since B has value $\gtrsim 5$ in the energy range considered and $|t|$ has a maximum value greater than 0 (close to unity) [24, 25, 26, 27, 28], the (integrated) cross section takes reasonably the form

$$\sigma = \frac{1}{B}\left.\frac{d\sigma}{dt}\right|_{t=0}. \tag{3.2}$$

We note that the Eq. (2.1) gives an idea of how the dependence on W can be introduced in differential cross section.

3.2 The B-parameter as function on W

At high values of s ($s = W^2$), in Regge Theory[1] the cross section expression is [2]

$$\frac{d\sigma}{dt} = F(t)\, W^{4\,(\alpha(t)-1)}\,. \tag{3.3}$$

$F(t)$ incorporate the residue function and the signature factor; $\alpha(t)$ is the exchanged Pomeron trajectory, which can be written linearly:

$$\alpha(t) = \alpha_{_0} + \alpha'\, t\,, \tag{3.4}$$

where $\alpha_{_0} = 1.096 \pm 0.003$ [36] and $\alpha' = 0.25\,\mathrm{GeV}^2$ [37] are accepted values for the trajectory. By comparing Eq. (3.3) with Eq. (3.1), we have

$$B \sim 4\,\alpha'\,\ln W\,. \tag{3.5}$$

This relation seems inconsistent with the experimental data collected [26, 28]. Indeed, we could advance the hypothesis of an almost constant trend of the B-slope when the W energy changes. Therefore it is necessary to introduce in Eq. (3.5) some functions that take into account of the constancy of $B(W)$, i.e.

$$B(W) = 4\,\alpha'\,\ln W + \tilde{b_{_1}}(W) + \tilde{b_{_2}}(W)\,, \tag{3.6}$$

where $\tilde{b_{_1}}$ is the function that removes the dependence on W, $\tilde{b_{_2}}$ the function that gives the constancy. Eq. (3.6) can be rewritten as follows

$$B(W) = 2\alpha'\left[b_{_2}^{^W} + 2\,\ln W\right] + 2\beta' b_{_1}(W)\,, \tag{3.7}$$

with β', $b_{_1}(W)$ and $b_{_2}^{^W}$ to be determined. In particular

$$b_{_1}(W) = -2\,\frac{\alpha'}{\beta'}\,\Theta\,\ln W\,, \tag{3.8}$$

where $\Theta = 1$ implies no dependence on W, and

$$b_{_2}^{^W} \sim (2\,\alpha')^{-1}\, B(W) \sim 10.8\,, \tag{3.9}$$

by putting $\alpha' = 0.25\,\mathrm{GeV}^2$ and noting that, for $Q^2 = 8\,\mathrm{GeV}^2$, $B \simeq 5.40\,\mathrm{GeV}^{-2}$ in a wide range of values of W [26, 28].

[1] Overview of the Regge Theory is in Appendix C.

3.3 A parameterization for B-slope

From Eq. (3.3) and Eq. (3.1) we have that

$$\frac{d\sigma}{dt} \sim \left[W^{-4}\, e^{Bt}\right]\, e^{4\alpha_0 \ln W}\,. \tag{3.10}$$

This result makes clear that we can introduce a form similar to Eq. (3.7) which takes into account the dependence on t. For large s, the differential cross section can be written as the Eq. (A.46) [2], i.e.

$$\frac{d\sigma}{dt} = \frac{1}{16\,\pi\, s^2}\,|\mathcal{M}|^2\,, \tag{3.11}$$

where $\mathcal{M}$ is the relativistic scattering amplitude. Therefore, from Eq. (3.10) and by wanting to preserve the form of Eq. (3.11), we have

$$\frac{d\sigma}{dt} = \frac{|\mathcal{M}_c|^2}{16\,\pi\, W^4}\, e^{2\,\chi} \equiv \frac{|\mathcal{M}_c|^2}{16\,\pi\, W^4}\, e^{2\,\chi_0}\, e^{Bt}\,, \tag{3.12}$$

where

$$\chi_0 = (b_{_2} + 2\,\ln W)\,\alpha_{_0} + b_{_1}\beta_{_0}\,, \tag{3.13}$$

$$B = 2\,(b_{_2} + 2\,\ln W)\,\alpha' + 2b_{_1}\beta'\,. \tag{3.14}$$

Obviously $b_{_1}$, $b_{_2}$ and $|\mathcal{M}_c|^2$ are functions of W and Q^2; $\alpha_{_0}$, $\beta_{_0}$, α' and β' constants. We note that $b_{_2}$ is costant on W.

3.3.1 Check of trends $b_{_1}(Q^2)$ and $b_{_2}(Q^2)$

In order to determine the behavior of B as a function of Q^2, we can introduce the function

$$\mathcal{F} = \frac{B(W, Q^2)}{2\,\alpha'} - 2\ln W\,. \tag{3.15}$$

As shown in the Figure 3.1, built from the data of H1 2005-06 [26], it appears that $\mathcal{F}$ tends to a limit, for fixed W, and it's a function inverse on Q^2. Therefore

$$\frac{\beta'}{\alpha'}\, b_{_1} + b_{_2} \simeq \mathcal{F}\left(\frac{1}{Q^2}\right)\,. \tag{3.16}$$

By comparing the determined B-values of H1 2005-06 [26] and H1 2004-07 [28], it is clear that in the case of data extracted from H1 2004-07 (see Table 3.1), we

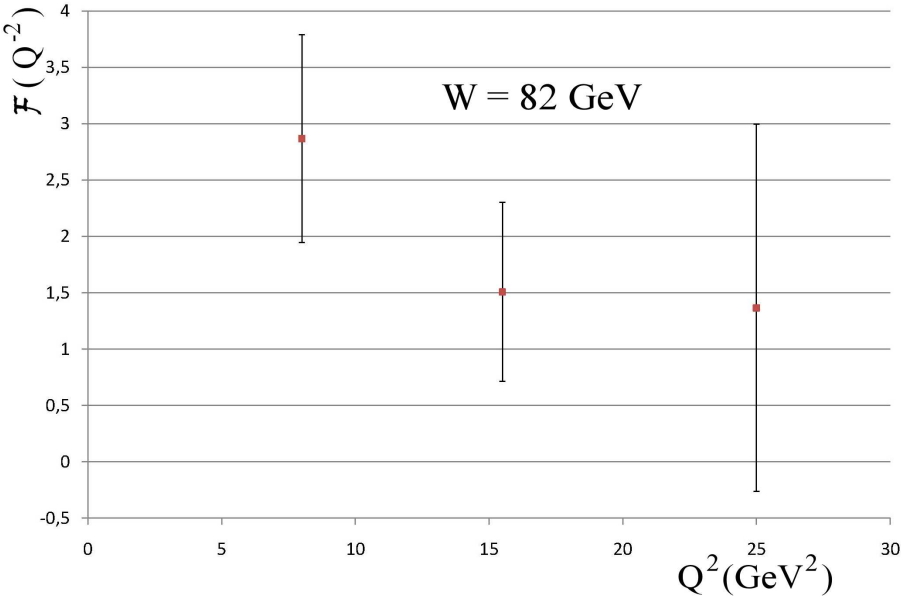

Figure 3.1: $\mathcal{F}$ as function of Q^2, with fixed W, calculated from the data of H1 2005-06 [26].

$W = 82\,\mathrm{GeV}$	$d\sigma/d\lvert t\rvert$ nb/GeV^2		
$\lvert t\rvert$ [GeV^2]	$Q_1^2 = 8\,\mathrm{GeV}^2$	$Q_2^2 = 15.5\,\mathrm{GeV}^2$	$Q_3^2 = 25\,\mathrm{GeV}^2$
0.1	$13.30 \pm 0.80 \pm 1.73$	$4.33 \pm 0.35 \pm 0.65$	$1.68 \pm 0.31 \pm 0.42$
0.3	$4.82 \pm 0.32 \pm 0.50$	$1.24 \pm 0.13 \pm 0.16$	$0.49 \pm 0.10 \pm 0.08$
0.5	$1.26 \pm 0.14 \pm 0.18$	$0.45 \pm 0.06 \pm 0.05$	$0.18 \pm 0.04 \pm 0.03$
0.8	$0.21 \pm 0.03 \pm 0.04$	$0.10 \pm 0.01 \pm 0.02$	$0.05 \pm 0.01 \pm 0.01$
B [GeV^{-2}]	$5.87 \pm 0.20 \pm 0.32$	$5.45 \pm 0.20 \pm 0.29$	$5.10 \pm 0.38 \pm 0.37$

Table 3.1: The differential cross section and the logarithmic slope, for fixed W (variable Q^2), extracted from Table 3 of [28]. The first errors are statistical, the second systematic.

cannot deduct the behaviour $\mathcal{F}(Q^{-2})$. It is necessary to develop a procedure to verify whether it is plausible the behavior of b_1 and b_2, determined by Eq. (3.16), also according the most recent data of H1. Let be

$$R^t_{Q^2_{i,i+1}} = \frac{1}{2} \ln \frac{d\sigma(Q^2_i)/d|t|}{d\sigma(Q^2_{i+1})/d|t|}\,, \tag{3.17}$$

i.e. by using Eq. (3.12)

$$R^t_{Q^2_{i,i+1}} = \chi(Q^2_i) - \chi(Q^2_{i+1})\,, \tag{3.18}$$

where the subscript i indicates the different Q^2 in the Table 3.1. Indicating with $|t|_1$ the value of $|t|$ appearing in the first row of the table and with the subscript j $(= 2, 3, 4)$ the values in other rows $(t = -|t|)$, we can introduce the quantity

$$\rho^{1,j}_{Q^2_{i,i+1}} \equiv \frac{t_j\, R^{t_1}_{Q^2_{i,i+1}} - t_1\, R^{t_j}_{Q^2_{i,i+1}}}{t_j - t_1}\,. \tag{3.19}$$

We note that $R^t_{Q^2_{1,3}} = R^t_{Q^2_{1,2}} + R^t_{Q^2_{2,3}}$, so in this analysis only the terms appearing in the sum are important. The data in Table 3.1 shows that $\rho^{1,j}_{Q^2_{i,i+1}}$ takes positive values (~ 0.5). From Eq. (3.18) we have that

$$\rho^{1,j}_{Q^2_{i,i+1}} = \rho^{1,j}_{Q^2_{i,i+1}}(\alpha_0) + \rho^{1,j}_{Q^2_{i,i+1}}(\beta_0) \tag{3.20}$$

$$= \left[b_2(Q^2_i) - b_2(Q^2_{i+1})\right]\, \alpha_0 + \left[b_1(Q^2_i) - b_1(Q^2_{i+1})\right]\, \beta_0\,. \tag{3.21}$$

Assuming[2] $\beta_0 > 0$, we obtain that $b_2(Q^2_i) > b_2(Q^2_{i+1})$ and $b_1(Q^2_i) > b_1(Q^2_{i+1})$, i.e., the two parameters b_1 and b_2 are monotone decreasing functions on Q^2.

3.3.2 Estimation of the constant Θ

In the same way as in the previous Subsection, for each $|t|$ reported in Table 3.2 (extracted from H1 2004-07 [28]), we can introduce the following quantity

$$R^t_{W_{i,i+1}} = \frac{1}{2} \ln \frac{d\sigma(W_i)/d|t|}{d\sigma(W_{i+1})/d|t|}\,, \tag{3.22}$$

[2]The Section 3.3.2 shows that the ratio β_0/β' is positive, so if $\beta' > 0$ then $\beta_0 > 0$. Actually β' should be *necessarily* positive, because, in case it was negative, the product $\beta' t$ would lead to a growth in cross section, proportional to $e^{|\beta'|\,|t|}$, inconsistent with the experimental data.

that, for Eq. (3.12), is equal to

$$\begin{aligned} R^{t}_{W_{i,i+1}} &= \chi(W_i) - \chi(W_{i+1}) = \\ &= 2\left[\alpha(t) - \frac{\alpha'}{\beta'}\,\Theta\,\beta(t)\right]\,\ln\left(\frac{W_i}{W_{i+1}}\right)\,, \end{aligned} \tag{3.23}$$

where the subscripts i $(=1,2)$ and $i+1$ indicate the different W values reported in Table 3.2. Denoted the different values of t by the subscripts j $(=1,2,3)$ and

$Q^2 = 10\,\mathrm{GeV}^2$	$d\sigma/d\lvert t\rvert$ [nb/GeV^2]		
$\lvert t\rvert$ [GeV^2]	$W_1 = 40\,\mathrm{GeV}$	$W_2 = 70\,\mathrm{GeV}$	$W_3 = 100\,\mathrm{GeV}$
0.1	$4.77 \pm 0.50 \pm 0.49$	$7.81 \pm 0.51 \pm 0.85$	$11.00 \pm 0.85 \pm 2.23$
0.3	$1.62 \pm 0.23 \pm 0.18$	$2.88 \pm 0.22 \pm 0.28$	$3.71 \pm 0.31 \pm 0.49$
0.5	$0.69 \pm 0.11 \pm 0.07$	$0.91 \pm 0.10 \pm 0.10$	$1.18 \pm 0.13 \pm 0.16$
0.8	$0.10 \pm 0.02 \pm 0.01$	$0.16 \pm 0.02 \pm 0.02$	$0.24 \pm 0.03 \pm 0.04$
B [GeV^{-2}]	$5.38 \pm 0.30 \pm 0.23$	$5.49 \pm 0.19 \pm 0.26$	$5.49 \pm 0.20 \pm 0.35$

Table 3.2: The differential cross section and the logarithmic slope, for fixed Q^2 (variable W), extracted from Table 3 of [28]. The first errors are statistical, the second systematic.

$j+1$ $(=2,3,4)$, it is possible define the expression

$$\Theta = 1 - \frac{1}{2\,\alpha'}\,\frac{R^{t_j}_{W_{i,i+1}} - R^{t_{j+1}}_{W_{i,i+1}}}{t_j - t_{j+1}}\,\ln\left(\frac{W_{j+1}}{W_j}\right)\,; \tag{3.24}$$

hence we can build the Table 3.3, which shows that the value $\Theta = 1$ is compatible with the experimental data.

Θ		
Δt [GeV^2]	calculated by data taken at W_1 and W_2	calculated by data taken at W_2 and W_3
$t_1 - t_2 = 0.2$	0.7697 ± 1.6162	1.1592 ± 1.1125
$t_2 - t_3 = 0.2$	1.8355 ± 1.8140	0.9883 ± 1.0879
$t_3 - t_4 = 0.3$	0.6395 ± 1.3893	0.8268 ± 0.8503
$\Theta = \Theta_0$	0.9826 ± 0.3525 (χ^2/d.o.f. = 0.1497)	0.9602 ± 0.0971 (χ^2/d.o.f. = 0.0286)

Table 3.3: The values of Θ-parameter, calculated by applying the Eq. (3.24) on data of Table 3.2. The last row gives the value calculated by performing a fit on the data obtained for different intervals Δt by using a constant function.

3.3.3 Estimation of the ratio β_0/β'

By using the Eq. (3.23) we can define

$$\rho^{1,j}_{W_{i,i+1}} = 2\left[\alpha_0 - \frac{\alpha'}{\beta'}\,\Theta\,\beta_0\right]\,\ln\left(\frac{W_i}{W_{i+1}}\right)\,, \tag{3.25}$$

where

$$\rho^{1,j}_{W_{i,i+1}} \equiv \frac{t_j\,R^{t_1}_{W_{i,i+1}} - t_1\,R^{t_j}_{W_{i,i+1}}}{t_j - t_1} \tag{3.26}$$

with $j = 2, 3, 4$ and $i = 1, 2$ clearly. From Eq. (3.25) we obtain

$$\frac{\beta_0}{\beta'}\,\Theta = \frac{\alpha_0}{\alpha'} - \frac{1}{\alpha'}\,\rho^{1,j}_{W_{i,i+1}}\,\ln\left(\frac{W_{i+1}}{W_i}\right)\,; \tag{3.27}$$

the average value of the second member of Eq. (3.27) is ~ 4; this value can be easily calculated by data in Table 3.2. Therefore

$$\frac{\beta_0}{\beta'} \sim \frac{4}{\Theta} \sim 4 \tag{3.28}$$

is a good approximation.

Chapter 4

Model for the DVCS process

In this Chapter, we define the values of parameters presented in the previous Chapter and we introduce a new phenomenological model for the DVCS process. The model is able to predict the values assumed by the logarithmic slope $B(W, Q^2)$ by varying W and Q^2 and it is compared with data collected from H1 [28].

4.1 The b_i parameters

In previous Chapter we have shown a new way to represent formally the squared amplitude of the DVCS process, by using the variable χ, determined by Eq. (3.13) and Eq. (3.14). By the parameterization of B, in order to remove the dependence on W, we have seen that it is necessary to introduce a further linear trajectory for the Pomeron: $\beta(t) = \beta_0 + \beta' t$; the Eq. (3.28) adjusts the ratio between β_0 and β'. In Section 3.3.1 we have shown that the parameters b_1 and b_2, which appear in the Equations (3.13) and (3.14), are monotone decreasing functions on Q^2, i.e.

$$b_1(Q^2) = b_1^{Q^2} + f_1(Q^2)\,, \tag{4.1}$$

$$b_2(Q^2) = b_2^{Q^2} + f_2(Q^2)\,, \tag{4.2}$$

where $b_i^{Q^2}$ and $f_i(Q^2)$, with $i = 1, 2$, are respectively constants and monotone decreasing functions on Q^2. By setting the *ansatz*

$$f_i(Q^2) = a_i \left(\frac{1}{Q^2}\right)^m, \qquad i = 1, 2\,, \tag{4.3}$$

b_i-parameters assume the following functional forms

$$b_1 = b_1^c - 2\,\frac{\alpha'}{\beta'}\,\Theta\,\ln W + a_1\left(Q^2\right)^{-m}\,, \tag{4.4}$$

$$b_2 = b_2^c + a_2\left(Q^2\right)^{-m}\,, \tag{4.5}$$

where $\Theta \simeq 1$ (see Subsection 3.3.2) and b_i, a_i $(i = 1, 2)$, m, β_0 and β' are constants to be determined. We set the parameters of exchanged Pomeron trajectory $\alpha(t)$ to values $\alpha_0 = 1.09$ [36] and $\alpha' = 0.25\,\mathrm{GeV}^2$ [37]. As stated in Section 3.1, the (integrated) cross section takes reasonably the form

$$\sigma = \frac{1}{B}\,\frac{d\sigma}{dt}\bigg|_{t=0} = \frac{|\mathcal{M}_c|^2}{16\,\pi\,W^4}\,\frac{e^{2\,\chi_0}}{B}\,. \tag{4.6}$$

By comparing Eq. (4.6) with Eq. (2.1), we obtain

$$\frac{e^{2\,\chi_0}}{B} \simeq e^{\left[\ln(Q^2)^{-n} + \delta(Q^2)\,\ln W\right]}\,, \tag{4.7}$$

4.1.1 The constants in b_i-parameters

By adopting the function

$$B = a \times \left(1/Q^2\right)^m\,, \tag{4.8}$$

we can calculate a and m-values for which the reduced chi-square, calculated on data of H1 Collaboration [25, 28], is minimal[1]:

$$a = 7.56428\,, \qquad m = 0.130676\,. \tag{4.9}$$

By comparing Eq. (3.14) with Eq. (4.8), we have

$$\begin{aligned} B\left(W, Q^2\right) &= 2\,\left[\left(b_2 + 2\,\ln W\right)\,\alpha' + b_1\beta'\right] \\ &= 2\,\left(a_1\,\beta' + a_2\,\alpha'\right)\,\left(\frac{1}{Q^2}\right)^m\,, \end{aligned} \tag{4.10}$$

i.e. $b_i^c = 0$ $(i = 1, 2)$ and

$$a = 2\,\left(a_1\,\beta' + a_2\,\alpha'\right)\,. \tag{4.11}$$

[1]The analysis to minimize chi-square was performed using *Mathematica* [38]. The used data were taken from [28, Table 3] and [25] for $Q^2 = 4\,\mathrm{GeV}^2$ and $W = 71\,\mathrm{GeV}$. The reduced chi-square, calculated for $7 - 2 = 5$ degrees of freedom available, is approximately 0.2265.

The Eq. (4.7) and Eq. (4.11) are satisfied by rewriting the parameters:

$$\begin{cases} b_1 = -2\,\dfrac{\alpha'}{\beta'}\,\Theta\,\ln W + a_1\left(Q^2\right)^{-m} + c_1 \ln\left(Q^2\right)^{-(n+m)} + d_1\,\delta\left(Q^2\right)\,\ln W\,, \\ b_2 = a_2\left(Q^2\right)^{-m} + c_2 \ln\left(Q^2\right)^{-(n+m)} + d_2\,\delta\left(Q^2\right)\,\ln W\,, \end{cases} \tag{4.12}$$

Clearly $\Theta = 1$ implies that B is independent on W. By using Eq. (4.12) in (4.7) and (4.10), we obtain

$$a_1\,\beta_0 + a_2\,\alpha_0 = 0\,, \tag{4.13}$$

$$c_1\,\beta' + c_2\,\alpha' = 0\,, \tag{4.14}$$

$$d_1\,\beta' + d_2\,\alpha' = 0\,, \tag{4.15}$$

Therefore, the b_i-parameters become

$$\begin{cases} b_1 = -\dfrac{\alpha_0}{\beta_0}\,a_2\left(Q^2\right)^{-m} - \dfrac{\alpha'}{\beta'}\,c_2 \ln\left(Q^2\right)^{-(n+m)} - \dfrac{\alpha'}{\beta'}\,\left[2\,\Theta\, + d_2\,\delta\left(Q^2\right)\right]\,\ln W\,, \\ b_2 = a_2\left(Q^2\right)^{-m} + c_2 \ln\left(Q^2\right)^{-(n+m)} + d_2\,\delta\left(Q^2\right)\,\ln W\,. \end{cases} \tag{4.16}$$

The a_2-constant is obtained from Eq. (4.11) and Eq. (4.13)

$$a_2 = \frac{a}{2\,\left[\alpha' - (\alpha_0/\beta_0)\;\beta'\right]}\,. \tag{4.17}$$

By using the Eq. (4.7), we have

$$\begin{aligned} 2\,\chi_0 &= 2\,\left[(b_2 + 2\,\ln W)\;\alpha_0 + b_1\beta_0\right] = \\ &= 2\,\left(\alpha_0 - \frac{\alpha'}{\beta'}\,\beta_0\right)\left(c_2 \ln\left(Q^2\right)^{-(n+m)} + d_2\,\delta\left(Q^2\right)\,\ln W\right) + \\ &\qquad + 4\,\left(\alpha_0 - \Theta\,\frac{\alpha'}{\beta'}\,\beta_0\right)\,\ln W \\ &= \ln(Q^2)^{-(n+m)} + \delta(Q^2)\,\ln W\,, \end{aligned} \tag{4.18}$$

for which

$$\alpha_0 - \Theta\,\frac{\beta_0}{\beta'}\,\alpha' \simeq 0 \qquad (\Theta = 1)\;, \tag{4.19}$$

due to the dependence of B on W, and the c_2 and d_2 constants are obtained by

$$c_2 = \frac{1}{2\,\left[\alpha_0 - (\alpha'/\beta')\;\beta_0\right]} = d_2\,. \tag{4.20}$$

We note that the Eq. (4.19) can be rewritten as

$$\beta_0/\beta' \simeq \alpha_0/\alpha' = 1.09/0.25 \simeq 4.36\,, \tag{4.21}$$

value consistent with that reported in Eq. (3.28). Obviously the equality $\beta_0/\beta' = \alpha_0/\alpha'$ produces a singularity in Eq. (4.20). Therefore, fixed the canonical values for α_0 and α', we must consider the values of β_0 and β' such that it's valid the following relation

$$W^{4\left[\alpha_0 - \Theta\,(\alpha'/\beta')\,\beta_0\right]} \simeq 1 \qquad (\Theta = 1) \tag{4.22}$$

in the range of considered energies. By putting

$$\beta_0 = 1.089999\,, \qquad \beta' = 0.25\,\mathrm{GeV}^{-2}\,, \tag{4.23}$$

we have

$$a_2 = -16490115.27\,, \tag{4.24}$$

and

$$c_2 = d_2 = 499999.99\,, \tag{4.25}$$

where the Eq. (4.9) was used. Once we have defined all the constants that characterize the parameters b_1 and b_2, we can plot the logarithmic slope $B(W, Q^2)$ as a function of W (fixed Q^2) or Q^2 (fixed W). As shown in Figures 4.1 and 4.2, the experimental data are approximated quite well with curves calculated by the new parametrization.

4.2 The $|\mathcal{M}_c|^2$ factor

We can consider the Tables 3.1 and 3.2 to find the $|\mathcal{M}_c|^2$-value. Denoted by $|t|_1$ the value of $|t|$ appearing in the first row of the table and by using the subscript j $(= 2, 3, 4)$ for the values in other rows $(t = -|t|)$, we can construct the quantity

$$L^{1,j} = \frac{1}{2}\ln\frac{d\sigma}{d|t|}\bigg|_{t_1} - \frac{1}{2}\ln\frac{d\sigma}{d|t|}\bigg|_{t_j} = \frac{1}{2}\,(t_1 - t_j)\,B\,. \tag{4.26}$$

An analogous quantity is calculated from differential cross sections obtained by the new parameterization

$$L^{1,j}_{\mathrm{th}} = \frac{1}{2}\ln\left[\frac{1}{|\mathcal{M}_c|^2}\,\frac{d\sigma}{d|t|}\bigg|_{t_1}\right]_{\mathrm{th}} - \frac{1}{2}\left[\frac{1}{|\mathcal{M}_c|^2}\,\frac{d\sigma}{d|t|}\bigg|_{t_j}\right]_{\mathrm{th}}\,. \tag{4.27}$$

Tables 4.1 and 4.2 compare the Eq. (4.26) with Eq. (4.27). $L^{1,j}_{th}$ takes values that approximate very well $L^{1,j}$, for different W and Q^2 energies. The Tables show also

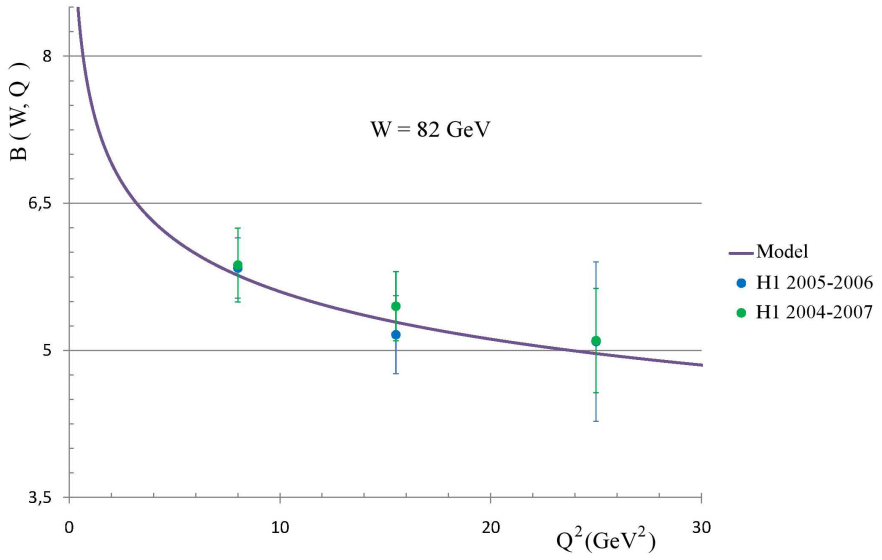

Figure 4.1: The logarithmic slope B as function of Q^2. The experimental data shown in figure are taken from H1 2005-2006 (blue circles) [26] and from H1 2004-2007 (green circles) [28].

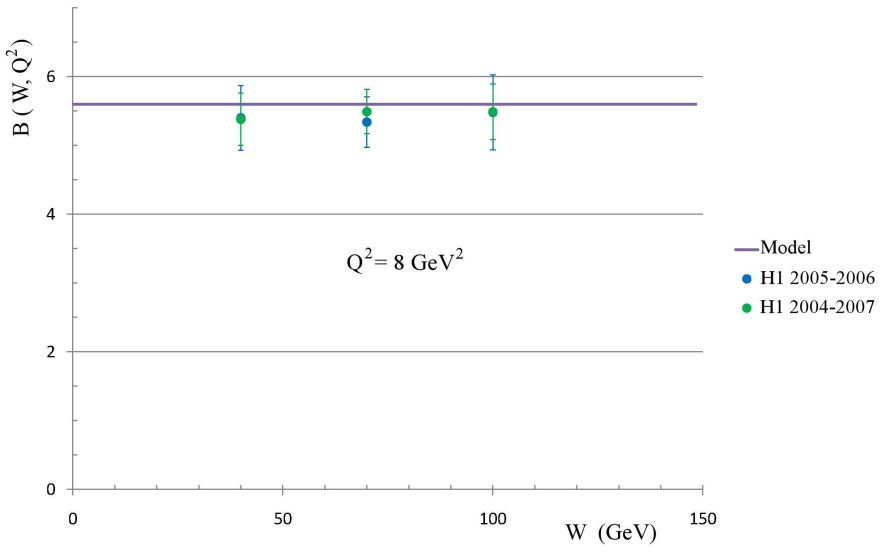

Figure 4.2: The logarithmic slope B as function of W. The experimental data shown in figure were taken from H1 2005-2006 (blue circles) [26]and from H1 2004-2007 (green circles) [28].

the quantity $(t_1 - t_j)\, B/2$, where values of B are taken from H1 2004-2007 [28]. $|\mathcal{M}_c|^2$ can be determined by ratio of the row-values of second column with those of the fifth. This procedure allows to normalize the theoretical data, reported in last column, to the experimental ones, reported in second column.

4.2.1 $|\mathcal{M}_c|^2$ as function on W

In two different series of Table 4.2 (fixed Q^2) the $|\mathcal{M}_c|^2$-values are different for at least an order of magnitude. So for each data set, considered at fixed Q^2, the average value $\langle |\mathcal{M}_c|^2 \rangle$ is calculated. By comparing the different average values, we note that the factor $|\mathcal{M}_c|^2$ significantly increases with W increasing. By assuming that this growth is due to a dependence of power-type as the following

$$\ln |\mathcal{M}_c|^2 = \ln |\mathcal{M}_c(Q^2)|^2 + m' \ln W \,, \tag{4.28}$$

we perform a fit on the average values of series. By this analysis we obtain $|\mathcal{M}_c(Q^2)|^2 = 1081 \pm 3$ and $m' = 4.1743 \pm 0.0044$, where the latter value is consistent with the Eq. (4.6) and Eq. (2.15). In fact, by setting $m' = 4$, the function of Eq. (4.28) gives a good fit with

$$|\mathcal{M}_c(Q^2)|^2 = 2340.7 \pm 9.9 \,. \tag{4.29}$$

In different series of Table 4.1 (fixed W) the $|\mathcal{M}_c|^2$-values are almost equal. Therefore it's reasonable to assume that $|\mathcal{M}_c|^2$ does not depend on Q^2 and has the constant value given in Eq. (4.29).

4.3 The cross sections

The differential and integrated cross section can be calculated from Eq. (3.12) and Eq. (4.6), by adopting the values of parameters here obtained. Figures 4.3 and 4.4 (4.5 and 4.6) show the experimental data collected by H1 2004-2007 [28] and curves of differential (integrated) cross sections obtained with the new parametrization. As shown in Figures, the curves fit very well[2] with experimen-

[2] In order to calculate the reduced chi square, we note that the degrees of freedom are equal to the number of experimental points, since the constants and parameters, previously identified, are fixed.

$W = 82\,\mathrm{GeV}$ $Q^2 = 8\,\mathrm{GeV}^2$								
$\lvert t\rvert$	$d\sigma/d\lvert t\rvert$	$(1/2)\,(t_1 - t_j)\,B$	$L^{1,j}$	$[\,\lvert\mathcal{M}_c\rvert^{-2}\,d\sigma/d\lvert t\rvert\,]_{\mathrm{th}}$	$L^{1,j}_{\mathrm{th}}$	$\lvert\mathcal{M}_c\rvert^2\,(\times 10^{11})$	$\eta^{1,j}$	$[\,d\sigma/d\lvert t\rvert\,]_{\mathrm{th}}$
0.1	13.30 ± 1.91	—	—	1.2968×10^{-10}	—	1.026 ± 0.147	—	13.7234 ± 0.0581
0.3	4.82 ± 0.59	-0.5870 ± 0.0377	-0.5075 ± 0.1332	4.0942×10^{-11}	-0.5764	1.177 ± 0.150	1.148 ± 0.306	4.3328 ± 0.0183
0.5	1.26 ± 0.23	-1.1740 ± 0.0755	-1.1783 ± 0.1521	1.2927×10^{-11}	-1.1529	0.975 ± 0.176	0.950 ± 0.308	1.3680 ± 0.0058
0.8	0.21 ± 0.05	-2.0545 ± 0.1321	-2.0742 ± 0.2095	2.2932×10^{-12}	-2.0175	0.916 ± 0.218	0.893 ± 0.341	0.2427 ± 0.0010
$W = 82\,\mathrm{GeV}$ $Q^2 = 15.5\,\mathrm{GeV}^2$								
$\lvert t\rvert$	$d\sigma/d\lvert t\rvert$	$(1/2)\,(t_1 - t_j)\,B$	$L^{1,j}$	$[\,\lvert\mathcal{M}_c\rvert^{-2}\,d\sigma/d\lvert t\rvert\,]_{\mathrm{th}}$	$L^{1,j}_{\mathrm{th}}$	$\lvert\mathcal{M}_c\rvert^2\,(\times 10^{11})$	$\eta^{1,j}$	$[\,d\sigma/d\lvert t\rvert\,]_{\mathrm{th}}$
0.1	4.33 ± 0.74	—	—	4.1763×10^{-11}	—	1.037 ± 0.177	—	4.4196 ± 0.0187
0.3	1.24 ± 0.21	-0.5450 ± 0.0352	-0.6252 ± 0.1684	1.4506×10^{-11}	-0.5287	0.855 ± 0.142	0.824 ± 0.278	1.5352 ± 0.0065
0.5	0.45 ± 0.08	-1.0900 ± 0.0705	-1.1320 ± 0.1699	5.0387×10^{-12}	-1.0574	0.893 ± 0.155	0.861 ± 0.296	0.5332 ± 0.0023
0.8	0.10 ± 0.02	-1.9075 ± 0.1233	-1.8841 ± 0.1986	1.0315×10^{-12}	-1.8505	0.970 ± 0.217	0.935 ± 0.369	0.1092 ± 0.0005
$W = 82\,\mathrm{GeV}^2$ $Q^2 = 25\,\mathrm{GeV}^2$								
$\lvert t\rvert$	$d\sigma/d\lvert t\rvert$	$(1/2)\,(t_1 - t_j)\,B$	$L^{1,j}$	$[\,\lvert\mathcal{M}_c\rvert^{-2}\,d\sigma/d\lvert t\rvert\,]_{\mathrm{th}}$	$L^{1,j}_{\mathrm{th}}$	$\lvert\mathcal{M}_c\rvert^2\,(\times 10^{11})$	$\eta^{1,j}$	$[\,d\sigma/d\lvert t\rvert\,]_{\mathrm{th}}$
0.1	1.68 ± 0.52	—	—	1.6531×10^{-11}	—	1.016 ± 0.316	—	1.7495 ± 0.0074
0.3	0.49 ± 0.13	-0.5100 ± 0.0530	-0.6161 ± 0.2860	6.1218×10^{-12}	-0.4967	0.800 ± 0.209	0.788 ± 0.451	0.6479 ± 0.0027
0.5	0.18 ± 0.05	-1.0200 ± 0.1061	-1.1168 ± 0.2696	2.2670×10^{-12}	-0.9934	0.794 ± 0.221	0.781 ± 0.460	0.2399 ± 0.0010
0.8	0.05 ± 0.01	-1.7850 ± 0.1856	-1.7573 ± 0.2803	5.1088×10^{-13}	-1.7384	0.979 ± 0.277	0.963 ± 0.572	0.0541 ± 0.0002

Table 4.1: The values of the differential cross section and logarithmic slope were extracted from Table 3 of [28] (see Table 3.1). The experimental errors were obtained from the sum in quadrature of statistical and systematic errors. The units of measurement are not given for convenience of writing. For each series we have calculated the ratio $\eta^{1,j} = |\mathcal{M}_c|^2_j/|\mathcal{M}_c|^2_1$, $j = 2, 3, 4$.

$Q^2 = 10\,\mathrm{GeV}^2$ $W = 40\,\mathrm{GeV}$								
$\lvert t\rvert$	$d\sigma/d\lvert t\rvert$	$(1/2)\,(t_1 - t_j)\,B$	$L^{1,j}$	$[\,\lvert\mathcal{M}_c\rvert^{-2}\,d\sigma/d\lvert t\rvert\,]_{\mathrm{th}}$	$L^{1,j}_{\mathrm{th}}$	$\lvert\mathcal{M}_c\rvert^2\,(\times 10^{9})$	$\eta^{1,j}$	$[\,d\sigma/d\lvert t\rvert\,]_{\mathrm{th}}$
0.1	4.77 ± 0.70	—	—	9.6763×10^{-10}	—	4.930 ± 0.723	—	5.7982 ± 0.0245
0.3	1.62 ± 0.29	-0.5380 ± 0.0378	-0.5400 ± 0.1635	3.1580×10^{-10}	-0.5599	5.130 ± 0.925	1.041 ± 0.340	1.8923 ± 0.0080
0.5	0.69 ± 0.13	-1.0760 ± 0.0756	-0.9667 ± 0.1846	1.0306×10^{-10}	-1.1198	$6.695 \pm 0.1.265$	1.358 ± 0.456	0.6176 ± 0.0026
0.8	0.10 ± 0.02	-1.8830 ± 0.1323	-1.9325 ± 0.2063	1.9216×10^{-11}	-1.9596	$5.204 \pm 0.1.164$	1.056 ± 0.391	0.1151 ± 0.0005
$Q^2 = 10\,\mathrm{GeV}^2$ $W = 70\,\mathrm{GeV}$								
$\lvert t\rvert$	$d\sigma/d\lvert t\rvert$	$(1/2)\,(t_1 - t_j)\,B$	$L^{1,j}$	$[\,\lvert\mathcal{M}_c\rvert^{-2}\,d\sigma/d\lvert t\rvert\,]_{\mathrm{th}}$	$L^{1,j}_{\mathrm{th}}$	$\lvert\mathcal{M}_c\rvert^2\,(\times 10^{10})$	$\eta^{1,j}$	$[\,d\sigma/d\lvert t\rvert\,]_{\mathrm{th}}$
0.1	7.81 ± 0.99	—	—	1.5252×10^{-10}	—	5.121 ± 0.650	—	8.5715 ± 0.0363
0.3	2.88 ± 0.36	-0.5490 ± 0.0322	-0.4988 ± 0.1253	4.9775×10^{-11}	-0.5599	5.786 ± 0.715	1.130 ± 0.283	2.7974 ± 0.0118
0.5	0.91 ± 0.14	-1.0980 ± 0.0644	-1.0749 ± 0.1395	1.6245×10^{-11}	-1.1198	5.602 ± 0.871	1.094 ± 0.309	0.9130 ± 0.0039
0.8	0.16 ± 0.03	-1.9215 ± 0.1127	-1.9440 ± 0.16613	3.0287×10^{-12}	-1.9596	5.283 ± 0.934	1.032 ± 0.313	0.1702 ± 0.0007
$Q^2 = 10\,\mathrm{GeV}^2$ $W = 100\,\mathrm{GeV}$								
$\lvert t\rvert$	$d\sigma/d\lvert t\rvert$	$(1/2)\,(t_1 - t_j)\,B$	$L^{1,j}$	$[\,\lvert\mathcal{M}_c\rvert^{-2}\,d\sigma/d\lvert t\rvert\,]_{\mathrm{th}}$	$L^{1,j}_{\mathrm{th}}$	$\lvert\mathcal{M}_c\rvert^2\,(\times 10^{11})$	$\eta^{1,j}$	$[\,d\sigma/d\lvert t\rvert\,]_{\mathrm{th}}$
0.1	11.00 ± 2.39	—	—	4.6980×10^{-11}	—	2.341 ± 0.508	—	10.9965 ± 0.0465
0.3	3.71 ± 0.58	-0.5490 ± 0.0403	-0.5434 ± 0.1866	1.5332×10^{-11}	-0.5598	2.420 ± 0.378	1.033 ± 0.386	3.5888 ± 0.0152
0.5	1.18 ± 0.21	-1.0980 ± 0.0806	-1.1162 ± 0.1655	5.0039×10^{-12}	-1.1198	2.358 ± 0.412	1.007 ± 0.394	1.1713 ± 0.0050
0.8	0.24 ± 0.05	-1.9215 ± 0.1411	-1.9125 ± 0.1915	9.3294×10^{-13}	-1.9596	2.573 ± 0.536	1.099 ± 0.467	0.2184 ± 0.0009

Table 4.2: The values of the differential cross section and logarithmic slope were extracted from Table 3 of [28] (see Table 3.2). The experimental errors were obtained from the sum in quadrature of statistical and systematic errors. The units of measurement are not given for convenience of writing. For each series we have calculated the ratio $\eta^{1,j} = |\mathcal{M}_c|^2_j/|\mathcal{M}_c|^2_1$, $j = 2, 3, 4$.

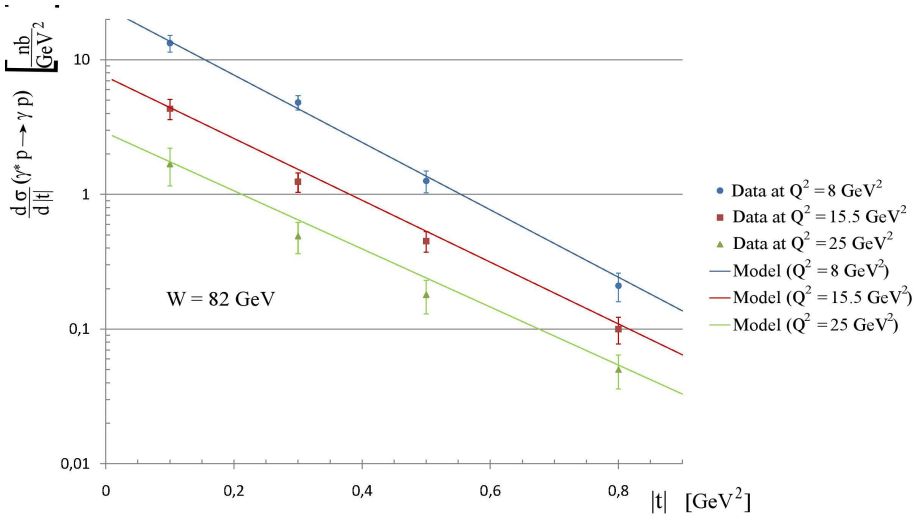

Figure 4.3: The experimental data are collected by H1 2004-2007 [28] (first two columns of Table 4.1).

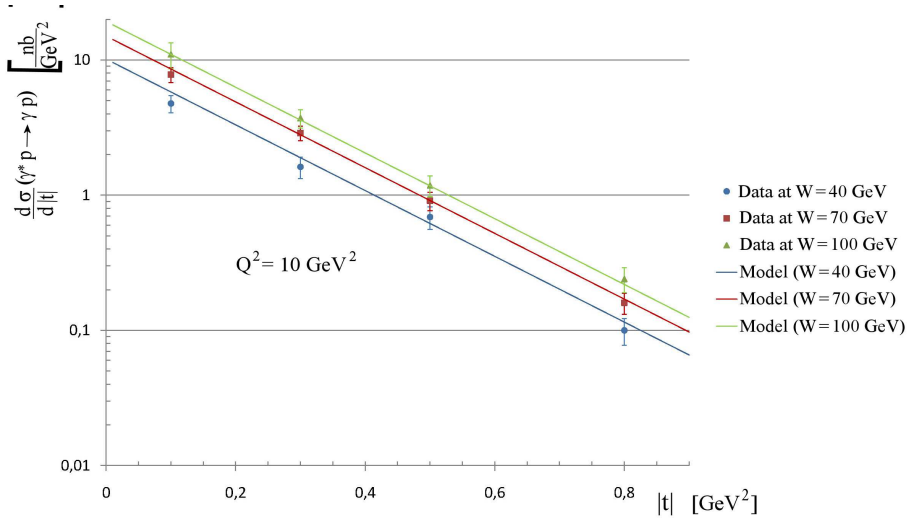

Figure 4.4: The experimental data are collected by H1 2004-2007 [28] (first two columns of Table 4.2).

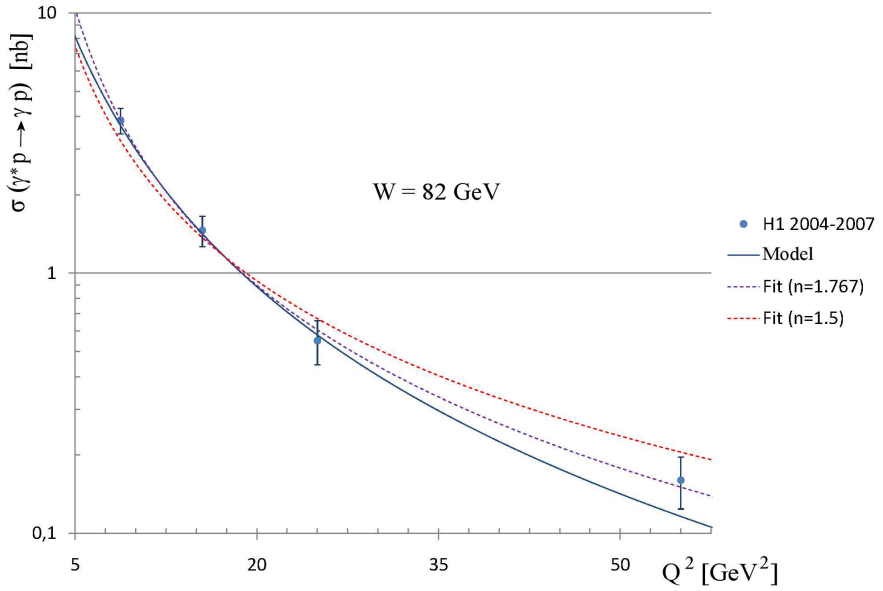

Figure 4.5: The experimental data are collected by H1 2004-2007 [28]. The full curve is obtained by the new parameterization. The dotted lines show the fits, of power-type $\sigma(Q^2) = c \times (Q^2)^{-n}$, performed on experimental data and by setting the n-parameter free (red dotted line) and to value determined by [25] and [24], i.e. $n \simeq 1.5$ (violet dotted line).

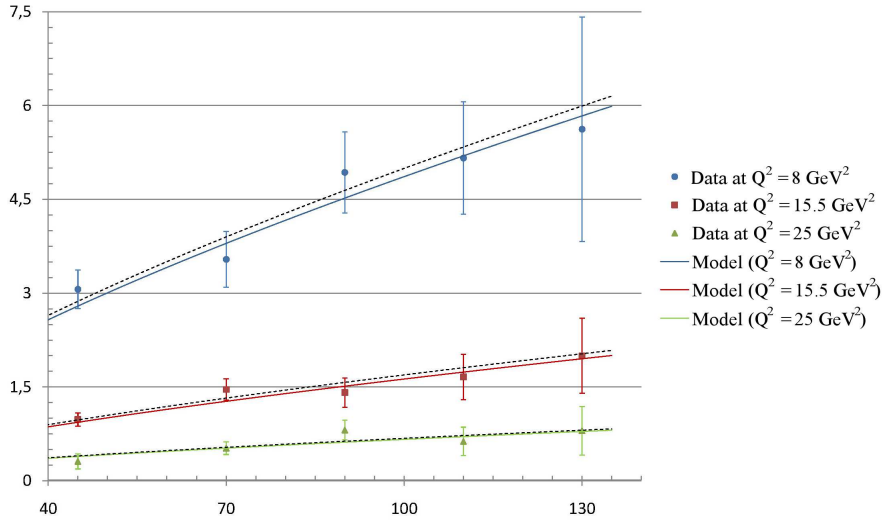

Figure 4.6: The experimental data are collected by H1 2004-2007 [28]. The full curves are obtained by the new parameterization. The dotted lines show the fit, of power-type $\sigma(W) = c' \times W^{\delta(Q^2)}$, performed on experimental data and by setting the δ-parameter to values determined by Eq. (2.33).

tal data.

4.4 Comparison with other parameterizations

To check the validity of the new parametrization, it is necessary to compare the values calculated for the parameter B (denoted by $B_{_{th}}$) with experimental measures provided by different Collaborations (see Table 4.3). All calculated values approximate well the measured data with the exception of that obtained for $Q^2 = 3.2\,\mathrm{GeV}^2$ and $W = 104\,\mathrm{GeV}$. By adopting the function of Eq. (3.1), we perform a fit on data collected by ZEUS 1999-2000 [27], whereby we obtain[3]

$$\left.\frac{d\sigma}{dt}\right|_{t=0} = (74.42 \pm 30.24)\,\mathrm{nb}\,, \tag{4.30}$$

with $\chi^2/\mathrm{d.o.f.} = 1.04$ and $B = (4.55 \pm 1.52)\,\mathrm{GeV}^{-2}$ which is consistent with the value provided by ZEUS Collaboration [27]. By putting $B \equiv B_{_{th}} = 6.50$, the fit makes $\chi^2/\mathrm{d.o.f.} = 1.22$ and

$$\left.\frac{d\sigma}{dt}\right|_{t=0} = (109.90 \pm 22.76)\,\mathrm{nb}\,, \tag{4.31}$$

which is also compatible with the theoretical value

$$\left.\frac{d\sigma}{dt}\right|_{t=0} = \frac{|\mathcal{M}_c|^2}{16\,\pi\,W^4}\,e^{2\,\chi_0} = 102.3104\,\mathrm{nb}\,. \tag{4.32}$$

calculated by setting $Q^2 = 3.2\,\mathrm{GeV}^2$ and $W = 104\,\mathrm{GeV}$. So, in our analysis, the B-value provided by the ZEUS Collaboration can be replaced with that calculated. We can also conduct a comparison with other functional forms for B, reported in other works. For example, Table 4.3 shows the parameterizations proposed by H1 2005-06 [26] and H1 2004-07 [28]. For H1 2005-06 the parametrization is [26]

$$B(Q^2) = A\,\left[1 - B'\log\left(\frac{Q^2}{2\,\mathrm{GeV}^2}\right)\right]\,, \tag{4.33}$$

where $A = (6.98 \pm 0.54)\,\mathrm{GeV}^{-2}$ e $B' = 0.12 \pm 0.03$; for H1 2004-07 the parametrization is [28]

$$B(W, Q^2) = B_0 + 2\alpha'\,\ln\left(\frac{1}{x}\right)\,, \tag{4.34}$$

[3]The fit was performed with *Origin Pro* [32].

Q^2	W	x $(\times 10^{-4})$	B	B_{th}	B from [26]	B from [28]	Reference
25	82	37.18	$5.10 \pm 0.38 \pm 0.37$	4.9670	6.06	5.10	H1 2004-2007 [28]
10	40	62.50	$5.38 \pm 0.30 \pm 0.23$	5.5988	6.39	4.84	H1 2004-2007 [28]
8	82	11.90	$5.87 \pm 0.20 \pm 0.32$	5.7644	6.48	5.67	H1 2004-2007 [28]
4	71	7.94	$6.66 \pm 0.54 \pm 0.43$	6.3109	6.73	5.87	H1 1996-1997 [25]
3.2	104	2.96	$4.50 \pm 1.30 \pm 0.40$	6.4977	6.81	6.37	ZEUS 1999-2000 [27]
2.6	32.25	25.00	6.70 ± 0.06	6.6764	6.88	5.30	BNL 1999-2000 [39]

Table 4.3: Values of the logarithmic slope B at different energies Q^2 and W. The fourth column shows B-values measured by several Collaborations (where there are two errors, the firsts are statistical and the seconds systematic) reported in the last column. The fifth column shows B_{th}-values calculated with new parametrization. The sixth and seventh columns report the values calculated from the parametrized forms given by Eq. (4.33) and Eq. (4.34). The units of measurement are not given for convenience of writing.

where $x \simeq Q^2/W^2$ is the variable of Bjorken, $\alpha' = 0.25\,\mathrm{GeV}^{-2}$ [37] and B_0 can be computed from an experimental value[4]. We note that none of the H1 parameterizations fits well with experimental data, unlike the new parametrization here proposed.

It is interesting to note that the DVCS logarithmic slope highlights a similar behavior in the case of diffractive processes (see Figure 1.10 bearing in mind that the point 'LPS DVCS ZEUS' must be led to the value 6.50). This evidence means that DVCS and diffractive processes can generally be described in the same way.

[4]For example, by value on the first row of Table 4.3, we can put $B_0 = 2.30275\,\mathrm{GeV}^{-2}$.

Conclusion

In this work we presented a new phenomenological model for the DVCS process, based on framework of the Regge Theory.

In particular, by considering that the standard procedure of rescaling does not rescale in an effective manner the data collected at different energies, we developed a further method to rescale data and this seems much more functional in order to conduct statistical analysis on the overall data set. These analyzes showed a dependence of δ-parameter on Q^2, whereby the factorized part of integrated cross section, expressed as $W^{\delta(Q^2)}$, varies on Q^2 in the same manner of the structure function of proton.

By the factorization of the differential cross section through the adoption of two exponential factors, we developed the model that is based on a new parametrization for DVCS cross section and slope parameter, denoted by B. The used exponential factors are dependent by two linear trajectories, $\alpha(t)$ and $\beta(t)$, of the exchanged Pomeron and two parameters, denoted by b_i $(i = 1, 2)$, which are functions of Q^2 and W energies. We noted that a experimental datum of the logarithmic slope B may be changed to a value close to that determined by the phenomenological model here proposed, without to a significant worsening of the reduced chi-square. This observation implies that the B-trend is compatible with all the collected experimental values. Therefore the behaviour of B for the DVCS processes is similar to that for the diffractive processes, whereby we hypothesize that the two processes occur analogously.

As shown in the Chapter 4, the curves of the model fit very well with the latest published experimental values.

Appendix A

Unitarity and Optical Theorem

The fundamental operator to describe a scattering process is the matrix $\mathcal{S}$. With its matrix elements we can define physical observables, such example, the cross section.

This Appendix[1] shows the main properties of the matrix $\mathcal{S}$, used in the theory of scattering.

A.1 The Mandelstam invariants

A generic scattering process with two initial particles and two final particles is

$$1(k) + 2(p) \longrightarrow 3(k') + 4(p')\,; \tag{A.1}$$

where we indicated in parentheses the four-momenta of the particles. The kinematics of the process can be described through three *variables of Mandelstam*

$$s = (k+p)^2 = (k'+p')^2\,, \tag{A.2a}$$

$$t = (k-k')^2 = (p-p')^2\,, \tag{A.2b}$$

$$u = (k-p')^2 = (p-k')^2\,. \tag{A.2c}$$

The utility of these variables derives from the fact that they are invariant under Lorentz transformations. From the law of conservation of four-momentum,

$$k + p = k' + p'\,, \tag{A.3}$$

[1]For more details, see [2].

we derive the following relationship which links s, t, u with the masses m_i (i = 1, 2, 3, 4) of the 4 particles

$$s + t + u = k^2 + p^2 + k'^2 + p'^2 = \sum_{i=1}^{4} m_i^2 \,, \tag{A.4}$$

which implies that only two of three Mandelstam invariants are independent. s e t are used usually as independent variables.

The Mandelstam variables here introduced define the process in the *s channel*. In this channel, s is the square of the incoming (or outgoing) total four-momentum, t is the square of the transferred four-momentum. It is possible to study the process in different reference frames.

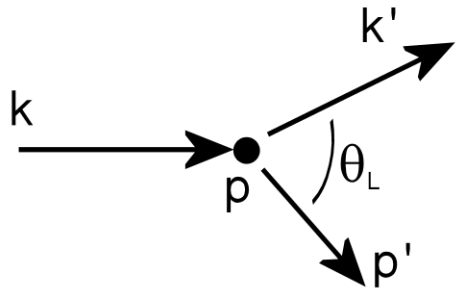

Figure A.1: The scattering process of Eq. (A.1) in the reference frame of laboratory (LAB).

In the reference frame of laboratory (LAB) the initial four-momenta (see Figure A.1) are

$$k = (E, \vec{k}\,) \,, \qquad\qquad p = (m_2, 0) \;, \tag{A.5}$$

where the energy E is given by

$$E = \sqrt{m_1^2 + |\vec{k}|^2} \,, \tag{A.6}$$

and s is

$$s = m_1^2 + m_2^2 + 2m_2\, E \,. \tag{A.7}$$

In the reference frame of center of mass (CM) we have (see Figure A.2)

$$\vec{k} + \vec{p} \,=\, \vec{k}\,' + \vec{p}\,' = 0 \,, \tag{A.8}$$

whereby the initial and final four-momenta are given respectively by

$$\begin{aligned} k &= (E, \vec{k})\,, & p &= (E_p, -\vec{k})\,, \\ k' &= (E', \vec{k}')\,, & p' &= (E_p{}', -\vec{k}')\,, \end{aligned} \tag{A.9}$$

and therefore we obtain

$$E = \sqrt{m_1^2 + |\vec{k}|^2}\,, \qquad E_p = \sqrt{m_2^2 + |\vec{k}|^2}\,, \tag{A.10a}$$

$$E' = \sqrt{m_1^2 + |\vec{k}'|^2}\,, \qquad E_p{}' = \sqrt{m_2^2 + |\vec{k}'|^2}\,. \tag{A.10b}$$

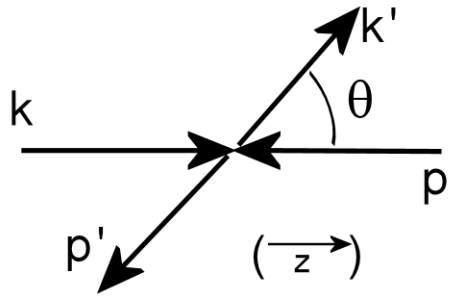

Figure A.2: The scattering process of Eq. (A.1) in the reference frame of the center of mass (CM).

By the Eq. (A.9) we obtain

$$s = (k + p)^2 = (E + E_p)^2\,. \tag{A.11}$$

The Eq. (A.11)shows that, in the CM frame, s is the square of the total energy. Equations (A.9)-(A.11) give the following expressions of the energies of the particles in the CM frame:

$$E = \frac{1}{2\sqrt{s}}\left[s + m_1^2 - m_2^2\right], \qquad E_p = \frac{1}{2\sqrt{s}}\left[s + m_2^2 - m_1^2\right], \tag{A.12a}$$

$$E' = \frac{1}{2\sqrt{s}}\left[s + m_3^2 - m_4^2\right], \qquad E_p{}' = \frac{1}{2\sqrt{s}}\left[s + m_4^2 - m_3^2\right]. \tag{A.12b}$$

Finally we obtain the following relations between $\vec{k}$, $\vec{k}'$ and s:

$$\vec{k}^{\,2} = \frac{1}{4s}\,\Delta(s, m_1^2, m_2^2)\,, \tag{A.13}$$

$$\vec{k}'^{\,2} = \frac{1}{4s}\,\Delta(s, m_3^2, m_4^2)\,, \tag{A.14}$$

where Δ is the "triangle function", i.e.

$$\Delta(x,y,z) = x^2 + y^2 + z^2 - 2xy - 2xz - 2yz\,. \tag{A.15}$$

At high energies ($s \longrightarrow \infty$) the differences between the masses of particles become negligible and, therefore, we may assume that all masses are equal. In those circumstances, the Mandelstam invariants s e t,

$$s = (k+p)^2 = 2\,m^2 + 2\,E\,E_p - 2\,\vec{k}\cdot\vec{p}, \tag{A.16}$$

$$t = (k-k')^2 = 2\,m^2 - 2\,E\,E' + 2\,\vec{k}\cdot\vec{k}'\,, \tag{A.17}$$

in the CM frame assume, respectively, the following formulas

$$s = 4\,(\vec{k}^{\,2} + m^2)\,, \tag{A.18}$$

$$t = -2\,\vec{k}^{\,2}\,(1-\cos\theta)\,, \tag{A.19}$$

where θ is the angle between the two vectors $\vec{k}$ e $\vec{k}'$. In this case, by using Eq. (A.4), we have that

$$u = -2\,\vec{k}^{\,2}\,(1+\cos\theta)\,. \tag{A.20}$$

We note also that, for $s \longrightarrow \infty$, i.e. when the masses of particles may be negligible, the Equations (A.12) become

$$E\,,\,E_p\,,\,E'\,,\,E_p{}'\ \overset{s\to\infty}{\simeq}\ \frac{\sqrt{s}}{2}\,. \tag{A.21}$$

Likewise, the Equations (A.10) become

$$|\vec{k}|, |\vec{k}'|\ \overset{s\to\infty}{\simeq}\ \frac{\sqrt{s}}{2}\,. \tag{A.22}$$

By the Eq. (A.18) and Eq. (A.19), for $s \longrightarrow \infty$ and t fixed, we obtain

$$\cos\theta = 1 + \frac{2t}{s-4m^2}\ \overset{s\to\infty}{\simeq}\ 1 + \frac{2t}{s}\,, \tag{A.23}$$

whereby we derive the interesting relationship

$$t = -2\,\vec{k}^{\,2}\,\frac{1-\cos^2\theta}{1+\cos\theta} = -\frac{2\,\vec{k}_\perp{}^2}{1+\cos\theta}\ \overset{s\to\infty}{\simeq}\ -\vec{k}_\perp{}^2\,. \tag{A.24}$$

In addition to the process in the s channel, indicated by Eq. (A.1), we can consider the following process

$$1 + \bar{3} \longrightarrow \bar{2} + 4\,, \tag{A.25}$$

where $\bar{2}$ and $\bar{3}$ are the antiparticles[2] of the particles 2 and 3. In this case the Mandelstam invariant t becomes

$$t = (k + k')^2\,,$$

which is the square of total energy of CM frame. Therefore it is said that the process occurs in the t channel. Similarly for the process

$$1 + \bar{4} \longrightarrow \bar{2} + 3\,, \tag{A.26}$$

the Mandelstam invariant u is the the square of total energy of CM frame:

$$u = (k + p')^2\,,$$

In this case it is said that the process occurs in the u channel.
For the process in the s channel of Eq. (A.1), by Equations (A.18)-(A.20) we have

$$s \geq 4\,m^2\,, \qquad t \leq 0\,, \qquad u \leq 0\,.$$

This is the physical region of the s channel in the Mandelstam plan.
Similarly, for the processes of Eq. (A.25) and Eq. (A.26), the physical regions in the t channel and u channel are the followings

$$\begin{aligned} &t \geq 4\,m^2\,, \qquad s \leq 0\,, \qquad u \leq 0\,, \\ &u \geq 4\,m^2\,, \qquad s \leq 0\,, \qquad t \leq 0\,. \end{aligned}$$

As shown in Figure A.3, in the case of particles of equal mass, the physical domains of the three channels, s, t and u, are different and non-overlapping. It is

[2]We observe that $\bar{2}$ and $\bar{3}$ have the changed sign of momenta with respect to the particles 2 and 3.

said that the *crossing symmetry* connects the three processes, of Equations (A.1), (A.25) and (A.26), to the respective reverse processes, which are

$$\bar{3} + \bar{4} \longrightarrow \bar{1} + \bar{2} \qquad s \text{ channel} \tag{A.27a}$$

$$2 + \bar{4} \longrightarrow \bar{1} + 3 \qquad t \text{ channel} \tag{A.27b}$$

$$2 + \bar{3} \longrightarrow \bar{1} + 4 \qquad u \text{ channel}\,. \tag{A.27c}$$

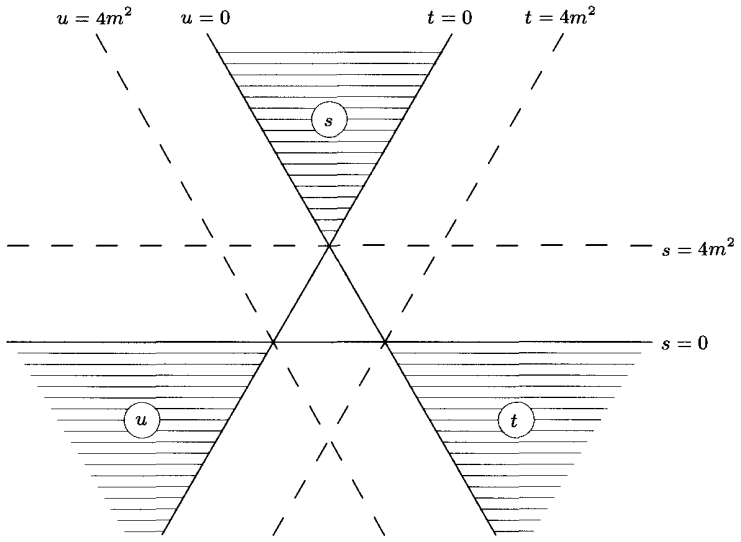

Figure A.3: The representation of the physical regions of the three channels, s, t and u (in case of equal masses) on Mandelstam plan.

A.2 The $\mathcal{S}$-matrix and cross section

The $\mathcal{S}$-matrix in a linear operator which in the scattering process transforms the initial state $|i\rangle$ in the final state $|f\rangle$:

$$\mathcal{S}\,|i\rangle = |f\rangle\ . \tag{A.28}$$

The $|i\rangle$ and $|f\rangle$ states are defined, respectively, to the times $-\infty$ and ∞, so that the particles of the physical system can be considered free. $\mathcal{P}_{fi}$ is the probability that, starting from the $|i\rangle$ state and after the scattering, the system is in the $|f\rangle$ state; it is given by

$$\mathcal{P}_{fi} = \left|\, \langle f|\, \mathcal{S}\, |i\rangle \,\right|^2 . \tag{A.29}$$

We note that the linearity of the $\mathcal{S}$ matrix reflects the superposition principle of quantum mechanics. $\mathcal{S}$ must also be relativistically invariant, i.e. its matrix elements have to depend on Lorentz-invariant combinations of the kinematic variables.
Three important properties of the $\mathcal{S}$ matrix are:

- unitarity,
- analyticity,
- crossing.

These properties will be described later.

We note that the $\mathcal{S}$-matrix may be written in the following form

$$\mathcal{S} = \mathbb{1} + \imath\,\mathcal{T}\,, \tag{A.30}$$

where the *matrix of transition*, $\mathcal{T}$, describes the scattering, i.e. $\mathcal{T}$ is the part of $\mathcal{S}$-matrix which does not leave the final state unchanged compared to the initial state. Therefore the elements of the $\mathcal{S}$ matrix are given by

$$\mathcal{S}_{fi} = \langle f|\,\mathcal{S}\,|i\rangle = \delta_{fi} + \imath\,\langle f|\,\mathcal{T}\,|i\rangle = \delta_{fi} + \imath\,\mathcal{T}_{fi}\,. \tag{A.31}$$

For a process like this:

$$a\,(p_a) + b\,(p_b) \to c_1{}'\,(p_1{}') + c_2{}'\,(p_2{}') + \cdots + c_n{}'\,(p_n{}') = \sum_{j=1}^{n} c_j{}'\,(p_j{}')\,, \tag{A.32}$$

Eq. (A.31) may be written by imposing explicitly the conservation of four-momentum, $p_a + p_b = \sum_j p_j{}'$, in the scattering process and we have

$$\mathcal{S}_{fi} = \delta_{fi} + \imath\,(2\pi)^4\,\delta^4\left(p_a + p_b - \sum_{j=1}^{n} p_j{}'\right)\mathcal{M}_{fi}\,; \tag{A.33}$$

where the matrix element $\mathcal{M}_{fi}$ is the Lorentz-invariant scattering amplitude. The differential cross section is expressed as

$$d\sigma = \frac{1}{\Phi}\,|\mathcal{M}_{fi}|^2 d\Pi_n\,. \tag{A.34}$$

where $d\Pi_n$ indicates the number of available states (per unit volume), in the phase space, for the final system. In the case of n final particles with momenta $p_j{}'$ $(j = 1, 2, \ldots, n)$, we have

$$d\Pi_n = \prod_{j=1}^{n} \frac{d^3\vec{p}_j{}'}{(2\pi)^3 2E_j{}'} \, (2\pi)^4 \, \delta^4 \left(p_a + p_b - \sum_{j=1}^{n} p_j{}' \right) . \tag{A.35}$$

In Eq. (A.34) Φ indicates the invariant flux of the incident particles and it is given by

$$\Phi = 2E_a \, 2E_b |\vec{v}_a - \vec{v}_b| \, , \tag{A.36}$$

where $\vec{v}_a$ and $\vec{v}_b$ are respectively the speeds of the incident particles a and b. The incident flux may be written as

$$\Phi = 4 \left[(p_a \cdot p_b)^2 - m_a^2 m_b^2 \right]^{1/2} . \tag{A.37}$$

By considering that $s = m_a^2 + m_b^2 + 2\, p_a \cdot p_b$ and using the triangle function Δ of Eq. (A.15), the flux factor becomes

$$\Phi = 2 \left[(2\, p_a \cdot p_b)^2 - 4\, m_a^2 m_b^2 \right]^{1/2} = 2\, \Delta^{1/2}(s, m_a^2, m_b^2) \, ; \tag{A.38}$$

for $s \longrightarrow \infty$, the masses are negligible and we have

$$\Phi \overset{s\to\infty}{\simeq} 2\, \Delta^{1/2}(s, 0, 0) = 2\, s \, . \tag{A.39}$$

Therefore, by including the Eq. (A.35) and Eq. (A.38) in Eq. (A.34), we obtain

$$d\sigma = \frac{1}{2\, \Delta^{1/2}(s, m_a^2, m_b^2)} \prod_{j=1}^{n} \frac{d^3\vec{p}_j{}'}{(2\pi)^3 2E_j{}'} \times (2\pi)^4 \, \delta^4 \left(p_a + p_b - \sum_{j=1}^{n} p_j{}' \right) |\mathcal{M}_{fi}|^2 \, . \tag{A.40}$$

In the case of processes of Eq. (A.1), the differential cross section becomes

$$d\sigma = \frac{1}{2\, \Delta^{1/2}(s, m_1^2, m_2^2)} \frac{d^3\vec{k}\,' \, d^3\vec{p}\,'}{(2\pi)^3 2E' \, (2\pi)^3 2E_p{}'} \times (2\pi)^4 \, \delta^4(k + p - k' - p') \, |\mathcal{M}(12 \longrightarrow 34)|^2 \, . \tag{A.41}$$

By performing the integration of $d^3\vec{p}\,'$ and taking into account that $d^3\vec{k}\,' = \vec{k}\,'^{\,2}\, d|\vec{k}\,'|\, d\Omega$, we have

$$\frac{d\sigma}{d\Omega} = \frac{1}{2\,\Delta^{1/2}(s, m_1^2, m_2^2)}\,\frac{1}{(2\pi)^3}\int \frac{\vec{k}\,'^{\,2}\, d|\vec{k}\,'|}{2E'\,2E_p{}'}\,\times \\ \delta(E + E_p - E' - E_p{}')\,|\mathcal{M}(12 \longrightarrow 34)|^2\,. \tag{A.42}$$

By the Eq. (A.9) and Eq. (A.10b), in the CM frame the integration of $|\vec{k}\,'|$ leads to

$$\frac{d\sigma}{d\Omega} = \frac{1}{32\,\pi^2\,\Delta^{1/2}(s, m_1^2, m_2^2)}\,\frac{|\vec{k}\,'|}{E' + E_p{}'}\,|\mathcal{M}(s,t)|^2\,, \tag{A.43}$$

which, for the Eq. (A.11) and Eq. (A.14), becomes

$$\frac{d\sigma}{d\Omega} = \frac{\Delta^{1/2}(s, m_1^3, m_2^4)}{64\,\pi^2\,s\,\Delta^{1/2}(s, m_1^2, m_2^2)}\,|\mathcal{M}(s,t)|^2\,. \tag{A.44}$$

For $s \longrightarrow \infty$, the masses in Δ function may be negligible and the Eq. (A.44) assumes the form

$$\frac{d\sigma}{d\Omega} \overset{s\to\infty}{\simeq} \frac{1}{64\,\pi^2\,s}\,|\mathcal{M}(s,t)|^2\,. \tag{A.45}$$

We note that the last equation also applies in the case of equal masses.
If the scattering amplitude does not depend on the azimuthal angle ϕ, by using the Eq. (A.23) the cross section may be expressed as a function of the t variable; Hence we have

$$\frac{d\sigma}{dt} \overset{s\to\infty}{\simeq} \frac{1}{16\,\pi\,s^2}\,|\mathcal{M}(s,t)|^2\,. \tag{A.46}$$

A.3 Unitarity and Optical Theorem

The unitarity of the $\mathcal{S}$ matrix,

$$\mathcal{S}^\dagger\mathcal{S} = \mathcal{S}\mathcal{S}^\dagger = \mathbb{1}\,, \tag{A.47}$$

follows directly from the conservation of probability. By substituting the Eq. (A.30) in Eq. (A.47), we obtain

$$(\mathbb{1} - \imath\,\mathcal{T}^\dagger)(\mathbb{1} + \imath\,\mathcal{T}) = \mathbb{1} - \imath\,\mathcal{T}^\dagger + \imath\,\mathcal{T} + \mathcal{T}^\dagger\mathcal{T} = \mathbb{1}\,,$$

which implies

$$\imath\,(\mathcal{T}^\dagger - \mathcal{T}) = \mathcal{T}^\dagger\mathcal{T}\,. \tag{A.48}$$

The Eq. (A.48) expresses the condition of unitarity in terms of the transition matrix $\mathcal{T}$. If we consider the matrix element calculated between the initial $|i\rangle$ and final $|f\rangle$ states of the scattering process, the previous formula leads to

$$\imath\,\langle f|\,(\mathcal{T}^\dagger - \mathcal{T})\,|i\rangle = \langle f|\,\mathcal{T}^\dagger\mathcal{T}\,|i\rangle\ . \tag{A.49}$$

By inserting in the second side of Eq. (A.49) a complete set of intermediate states $|n\rangle$, we obtain

$$2\,\mathbb{I}\mathrm{m}\,\mathcal{T}_{fi} = \sum_{\{n\}} \mathcal{T}^*_{nf}\,\mathcal{T}_{ni}\,. \tag{A.50}$$

In Eq. (A.50) the symbol $\sum_{\{n\}}$ indicates the integration on four-momenta of the various particles and the sum over all discrete quantum numbers. If the states $|n\rangle$ represent systems of n particles with spin 0, the symbol $\sum_{\{n\}}$ is

$$\sum_{\{n\}} = \sum_n \int \prod_{j=1}^{n} \frac{d^3\,\vec{p}_j}{(2\,\pi)^3\,2E_j}\,. \tag{A.51}$$

In the case, the Eq. (A.50) becomes

$$2\,\mathbb{I}\mathrm{m}\,\mathcal{T}_{fi} = \sum_n \int \prod_{j=1}^{n} \frac{d^3\,\vec{p}_j}{(2\,\pi)^3\,2E_j}\ \langle f|\,\mathcal{T}^\dagger\,|n\rangle\,\langle n|\,\mathcal{T}\,|i\rangle = \sum_{\{n\}} \mathcal{T}^*_{nf}\,\mathcal{T}_{ni}\,, \tag{A.52}$$

The Equations (A.50) form a set of nonlinear coupled integral equations which incorporate the whole information about unitarity of the $\mathcal{S}$-matrix.
If we make explicit the conservation of total four-momentum, the Eq. (A.50) may be expressed in terms of scattering amplitudes $\mathcal{M}_{fi}$, and we have

$$2\,\mathbb{I}\mathrm{m}\,\mathcal{M}_{fi} = \sum_n \int d\Pi_n\,\mathcal{M}^*_{nf}\,\mathcal{M}_{ni}\,, \tag{A.53}$$

where $d\Pi_n$ is the n-particle phase space measure and it is given by the Eq. (A.35). The unitarity equations (A.53), or (A.50), are graphically represented in Figure A.4.

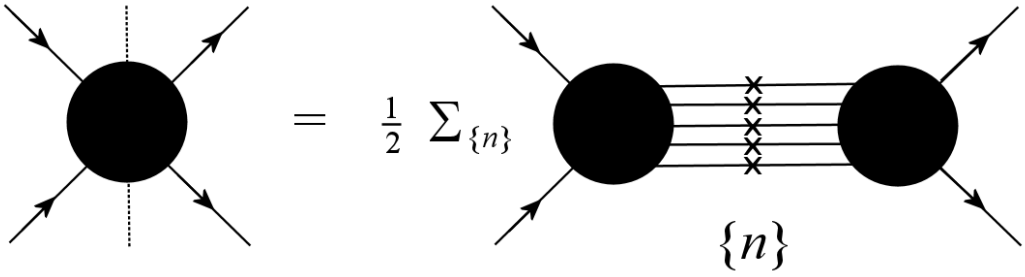

Figure A.4: Graphical representation of the unitarity equations (A.53), or (A.50). The cut on the left-hand side denotes the discontinuity of the amplitude. The crosses on the right-hand side denote particles on shell.

In the case of *forward elastic scattering* i.e. the $1+2 \longrightarrow 1+2$ process, where the initial and final states are identical, $|\, i\rangle = |\, f\rangle$, the Eq. (A.53) becomes

$$2\,\mathbb{I}\mathrm{m}\,\mathcal{M}_{\mathrm{el}}(s, t=0) = \sum_n \int d\Pi_n\, |\mathcal{M}_{ni}|^2\,. \tag{A.54}$$

We note that we obtain the total cross section by integrating the differential cross section given by Eq. (A.34):

$$\sigma_{\mathrm{tot}} = \frac{1}{\Phi} \sum_n \int d\Pi_n |\mathcal{M}_{ni}|^2\,. \tag{A.55}$$

By comparing the last equation with Eq. (A.54), we obtain

$$\sigma_{\mathrm{tot}} = \frac{2}{\Phi}\,\mathbb{I}\mathrm{m}\,\mathcal{M}_{\mathrm{el}}(s, t=0)\,, \tag{A.56}$$

which, for large s (i.e. for $s \longrightarrow \infty$) and by using the Eq. (A.39), gives

$$\sigma_{\mathrm{tot}} \overset{s\to\infty}{\simeq} \frac{1}{s}\,\mathbb{I}\mathrm{m}\,\mathcal{M}_{\mathrm{el}}(s, t=0)\,. \tag{A.57}$$

The Eq. (A.57) expresses the formulation of the *optical theorem* for the relativistic elastic scattering. This theorem states that the total cross section (i.e. the cross section for the process $1+2 \longrightarrow$ *anything*) is given by the imaginary part of the amplitude for elastic scattering $1+2 \longrightarrow 1+2$ in the forward direction. The optical theorem is expressed graphically in Figure A.5.

A.4 Analyticity and Crossing

The properties of *analyticity* and *crossing* of the matrix $\mathcal{S}$ are not derived from first principles, unlike the unitarity which is a consequence of the conservation of probability. They are postulated by perturbative quantum field theory.

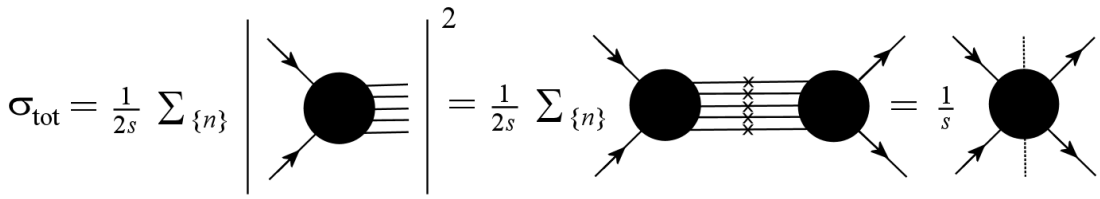

Figure A.5: Graphical representation of the optical theorem.

The analyticity principle states that the $\mathcal{S}$-matrix elements, i.e. the scattering amplitudes, are analytic functions of the kinematic variables, when these are continued to complex values.

The physical amplitudes are obtained in the limit where these analytic functions tend to real values, under the restrictions expressed in Subsection A.1. This assumption implies that the only singularities, which are present in the scattering amplitudes, are those deductible by unitarity. The singularities are simple poles (and branch points), which can be associated to the exchange of physical particles.

In order to introduce the properties of 'crossing', we consider the principle of relativistic field theory according to which, in a given scattering process, a particle incoming (outgoing) of four-momentum p may be considered as an antiparticle outgoing (incoming) of four-momentum $-p$.

The crossing property states that the same amplitude describes the two groups of three processes, connected by 'symmetry crossing':

$$\begin{aligned} 1+2 &\longrightarrow 3+4 && \text{canale } s \\ 1+\bar{3} &\longrightarrow \bar{2}+4 && \text{canale } t \\ 1+\bar{4} &\longrightarrow \bar{2}+3 && \text{canale } u\,, \end{aligned}$$

$$\begin{aligned} \bar{3}+\bar{4} &\longrightarrow \bar{1}+\bar{2} && \text{canale } s \\ 2+\bar{4} &\longrightarrow \bar{1}+3 && \text{canale } t \\ 2+\bar{3} &\longrightarrow \bar{1}+4 && \text{canale } u\,. \end{aligned}$$

The second group of three processes is obtained from the first by the CPT (Charge conjugation, Parity, Time reversal) Symmetry. In other terms, the same function

of the Mandelstam variables, s, t and u, can describe the six different physical processes above listed in the different domains of these variables (domains described in Subsection A.1), by assuming that the function analytically continues from a channel to another.

The properties of analyticity and crossing allow to obtain significant results on the behavior of the cross section; the most important are those obtained in the theorems of Froissart-Martin [40] and Pomeranchuk [16]. According to the first theorem, the growth of the total cross section at high energies has an upper limit:

$$\sigma_{\rm tot} \leq C \, \ln^2 s \,, \qquad \text{per} \;\; s \longrightarrow \infty \,, \tag{A.58}$$

where C is a constant. In its original formulation, the Pomeranchuk theorem states that if at high energies the total cross-sections for particle-particle (ab) and particle-antiparticle ($a\bar{b}$) scattering tend to constant values, then they tend to the same value

$$\sigma_{\rm tot}(ab) \stackrel{s\to\infty}{\simeq} \sigma_{\rm tot}(a\bar{b}) \,. \tag{A.59}$$

A more recent version of the Pomeranchuk theorem [41] shows that even when the total cross section increases with the energy the ratio between $\sigma_{\rm tot}(ab)$ and $\sigma_{\rm tot}(a\bar{b})$ tends to unity:

$$\frac{\sigma_{\rm tot}(ab)}{\sigma_{\rm tot}(a\bar{b})} \xrightarrow{s\to\infty} 1 \,. \tag{A.60}$$

Appendix B

The kinematics of DIS

The *Deep Inelastic Scattering* (*DIS*) is the process with which we can investigate the structure of hadrons (particularly the *baryons*, such as protons and neutrons), by using the scattering with *leptons*, in particular electrons, which may be considered pointlike.

In *ep* scattering, the electron interacts with the proton; there are two types of processes: the first one at neutral current (NC), the second one at charge current (CC). The NC processes imply the exchange of a virtual photon γ^* or a Z^0 boson; the CC processes imply the exchange of bosons $W^{\pm}$, whereby the lepton 'flavor' does not preserve and the outgoing lepton is a neutrino. For low transferred momenta, the electron-proton (ep) interaction occurs basically through the exchange of a virtual photon. Moreover, since the electromagnetic coupling constant is much smaller than 1, $\alpha \approx 1/137$, the corrections of higher order in the perturbative development of the scattering amplitude can be neglected.

In the Figure B.1 we report a diagram of a DIS *ep* process, where we have indicated the following four-momenta[1]:

$$k = (E, \vec{k}), \quad p = (E_p, \vec{p}), \quad k' = (E', \vec{k}'), \quad p' = (E_p', \vec{p}');$$

these ones represent respectively the four-momenta of incident electron and proton and scattered particles.
We note that in the final state a hadronic system X, consistent of one or more jet, might be detected in addition to lepton. In fact, the exchanged photon 'probes'

[1]In this work we used the system of natural units ($\hbar = c = 1$).

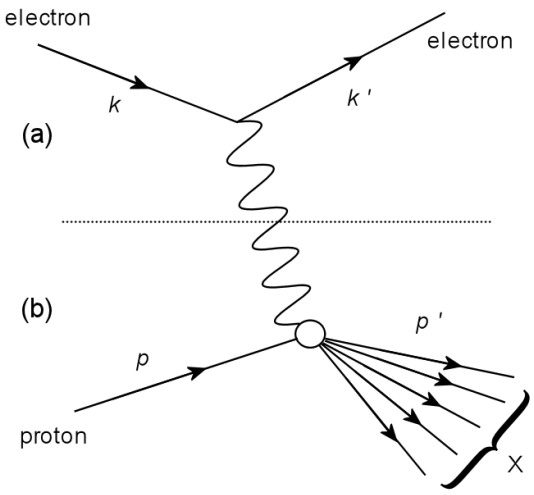

Figure B.1: Schematic representation of a typical *ep* inelastic process, where the *hadrons* are generated and the mechanisms of exchange with more photons are neglected. The dashed line shows the two regions (a) and (b), which refer respectively to the lepton vertex and proton vertex.

the structure of proton and, for resolving individual quarks inside the proton, it is necessary a high transferred four-momentum so that the photon wavelength is very small compared to the proton amplitude. In this region the inelastic scattering is dominated by processes such as the one shown in Figure B.2, i.e. by phenomena for which first an elastic scattering

$$e + q \longrightarrow e + q$$

can occur on a quark q content in the proton and then a 'fragmentation' process which converts in quark the scattered hadrons and the remaining constituents of the proton.

B.1 The kinematic variables

In this Section we define the kinematic variables which can characterize the *ep* scattering. These are chosen as relativistic invariant, i.e. quantities which remain unchanged when they are considered in the passage from one reference frame to another. These invariants are given by the scalar product of four vectors.

The kinematic variables are:

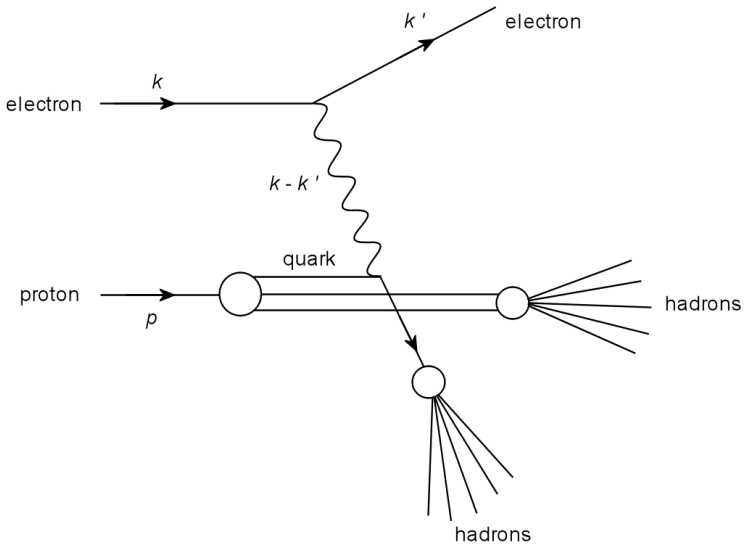

Figure B.2: Schematic representation of a typical process of *fragmentation*.

1. The *Mandelstam varables*[2] s and t, given respectively by

   - the total invariant mass, which is the squared sum of four-momenta of the incident electron (with mass m) and proton (with mass M):

   $$s = (k + p)^2 = m^2 + M^2 + 2\,EE_p - 2\,\vec{k} \cdot \vec{p}. \tag{B.1}$$

   In the reference frame of center of mass (CM), we have

   $$s = m^2 + M^2 + 2\,EE_p + 2\,|\vec{k}||\vec{p}|. \tag{B.2}$$

   At high energy, the masses are neglected and we obtain

   $$s \approx 4\,EE_p\,. \tag{B.3}$$

   - the square of the four-momentum transferred by electron to incident proton:

   $$t = q^2 = (k - k')^2\,. \tag{B.4}$$

2. The *virtuality* Q^2, given by

   $$Q^2 = -t\,. \tag{B.5}$$

[2]The Mandelstam varables and their properties are discussed in Appendix A.

This latter, in terms of four-momentum exchanged at lepton vertex, becomes

$$\begin{aligned} Q^2 &= -q^2 = -(k-k')^2 = -2m^2 + 2\,k\cdot k' \simeq \\ &\simeq 2\,k\cdot k' = 2\left(EE' - |\vec{k}||\vec{k}'|\cos\theta\right) = 4\,EE'\sin^2\frac{\theta}{2}\,, \end{aligned} \tag{B.6}$$

where we have used the relativistic limit:

$$E = \sqrt{m^2 + k^2} \approx |\vec{k}| \qquad \text{per} \quad E \gg m\,.$$

3. The ν parameter, which is the energy transferred by electron to proton in the reference frame of laboratory (LAB), where the proton is considered at rest; this parameter indicates the energy of virtual photon:

$$\nu = \frac{p\cdot q}{M} = \frac{(M,\vec{0}\,)\cdot(E-E',\vec{q}\,)}{M} = E - E'\,. \tag{B.7}$$

4. The invariant mass of final hadronic system, which is given by the squared sum of four-momenta of exchanged boson and incident proton:

$$W^2 = (p+q)^2 = M^2 + 2\,p\cdot q + q^2 = M^2 + 2\,p\cdot q - Q^2\,. \tag{B.8}$$

5. The adimensiona variables of Bjorken scale x and y, which represent respectively the measure of inelasticity of the scattering [42, page 87] and the ratio between the transferred energy and energy of incident electron in the LAB:

$$x = \frac{-q^2}{2\,p\cdot q} = \frac{Q^2}{2\,M\nu}\,, \tag{B.9}$$

$$y = \frac{p\cdot q}{p\cdot k} = \frac{E-E'}{E} = \frac{\nu}{E}\,. \tag{B.10}$$

B.2 Relations between the kinematic variables

In the relativistic case, where we can neglect the masses of the incident particles ($s \approx 2\,p\cdot q$), we have

$$x = \frac{Q^2}{2\,p\cdot q} = \frac{Q^2}{y\;(2\,p\cdot k)} \approx \frac{Q^2}{y\,s} \geq 0\,. \tag{B.11}$$

In the relativistic case $W > M$, by the Eq. (B.8) we obtain

$$2\,p \cdot q - Q^2 = W^2 - M^2 > 0\,,$$

whereby

$$0 \leq x < 1\,;$$

by the relation $|\vec{k}\,'|^2 \leq |\vec{k}|^2$ and the Eq. (B.10), we obtain

$$y = \frac{p \cdot q}{p \cdot k} = 1 - \frac{p \cdot k\,'}{p \cdot k} \leq 1\,.$$

Therefore, we have also that

$$0 < y \leq 1\,.$$

Appendix C

The Regge approach to diffraction

The Regge Theory[1] [43] was born in the framework of quantum mechanics and was later extended to the treatment of scattering at high energies. The idea, from which the whole treatment is developed, is the possibility to analytically continue the scattering amplitude to complex values of the angular momentum.
The development of partial waves (in the s channel) for the scattering amplitude is

$$\mathcal{M}(s,z) = \sum_{\ell=0}^{\infty} (2\ell+1)\mathcal{M}_\ell(s)\, P_\ell(z)\,, \tag{C.1}$$

where the sum is extended to all possible values of the angular momentum ℓ and P_ℓ is the Legendre polynomial containing the angular dependence, denoted by $z = \cos\theta$.

The partial-wave amplitude $\mathcal{M}_\ell(s)$ may be continued to complex values of ℓ whereby we can construct an interpolating function $\mathcal{M}(\ell, s)$ which reduces to $\mathcal{M}_\ell(s)$ for real integer ℓ. we suppose that

- $\mathcal{M}(\ell, s)$ has only isolated singularities in the complex ℓ plane,
- $\mathcal{M}(\ell, s)$ is holomorphic for $\mathbb{R}\mathrm{e}\,\ell > L$,
- $\mathcal{M}(\ell, s) \longrightarrow 0$ as $|\ell| \longrightarrow \infty$, per $\mathbb{R}\mathrm{e}\,\ell > 0$.

[1] For more details, see [2].

Under these conditions it's possible to show that the Eq. (C.1) becomes

$$\mathcal{M}(s,z) = \sum_{l=0}^{N-1} (2\ell+1)\mathcal{M}_\ell(s)\, P_\ell(z) - \frac{1}{2\imath}\int_C (2\ell+1)\mathcal{M}(\ell,s)\,\frac{P_\ell(-z)}{\sin(\pi\ell)}\,d\ell\,, \quad \text{(C.2)}$$

where N is the first integer greater than L and C is the contour shown in Figure C.1 (it avoids all singularities of $\mathcal{M}(\ell,s)$).

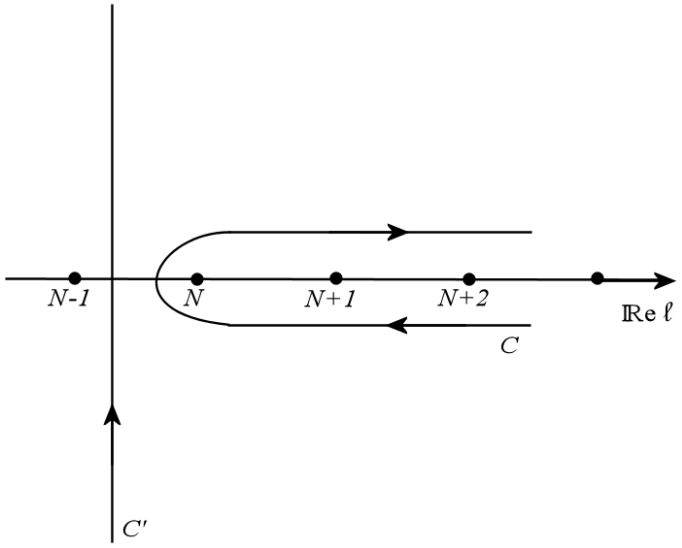

Figure C.1: The integration contour for the Watson-Sommerfeld representation of the scattering amplitude. C avoids all singularities of $\mathcal{M}(\ell,s)$. We note that C' is to right of all singularities of $\mathcal{M}(\ell,s)$. With the deformation from C to C', in Eq. (C.2) $\int_{a-\imath\infty}^{a+\imath\infty}$ will replace $\int_C$. It is understood that the paths are closed to infinity.

In the method developed by Regge, the path C is deformed in the path $C' = (a-\imath\infty, a+\imath\infty)$, a line parallel to the imaginary ℓ axis that leaves to the right all the singularities of amplitude $\mathcal{M}(\ell,s)$ in the complex plan [2] ℓ (see Figure C.1). By moving C' to smaller values of $\mathbb{R}\mathrm{e}\,\ell$ we obtain contributions from the residues of the poles of $\mathcal{M}(\ell,s)$ (for example, the circles 1 and 2 in Figure C.2). If we impone that C' intersects the axis $\mathbb{R}\mathrm{e}\,\ell$ within the region $-1/2 \leq \mathbb{R}\mathrm{e}\,\ell < 0$, the Eq. (C.2) may be written in the Watson-Sommerfeld representation:

$$\mathcal{M}(s,z) = -\sum_i (2\,\alpha_i(s)+1)\;\pi\beta(\alpha_i,s)\frac{P_{\alpha_i}(-z)}{\sin\pi\,\alpha_i} - \frac{1}{2\imath}\int_{c-\imath\infty}^{c+\imath\infty}(2\ell+1)\mathcal{M}(\ell,s)\,\frac{P_\ell(-z)}{\sin(\pi\ell)}\,d\ell\,, \quad \text{(C.3)}$$

[2] In our simplified analysis we do not take account of possible cuts or branch points.

where $\alpha_i(s)$ (called *Regge poles*) are the poles of $\mathcal{M}(\ell, s)$ in the complex plan ℓ, and $\beta(\alpha_i, s)$ are the residues calculated in the poles (see Figure C.2).

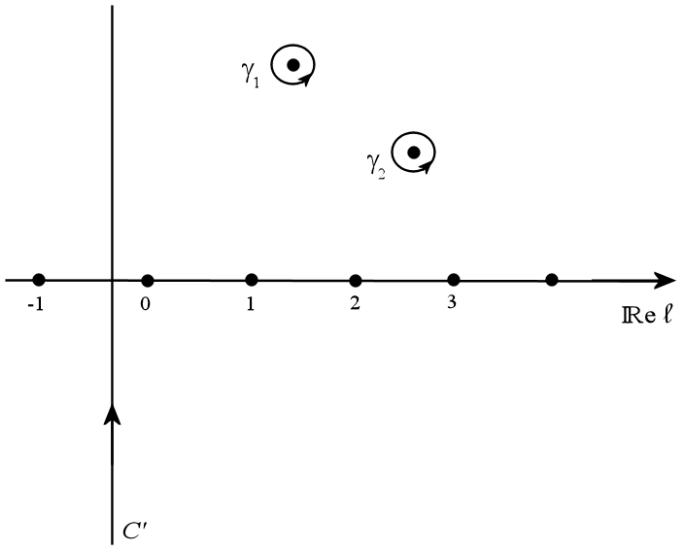

Figure C.2: The deformed integration contour for the Watson-Sommerfeld representation of the scattering amplitude.

For the large-t, i.e. for the large z by the Eq. (A.23), and by $\mathbb{R}\mathrm{e}\,\ell \geq -1/2$ we have

$$P_\ell(z) \overset{|z|\to\infty}{\sim} z^\ell\,; \tag{C.4}$$

the integral in Eq. (C.3) behaves as $|z|^{-\frac{1}{2}}$ and it is negligible at large-z. Therefore the scattering amplitude is given only by the sum on residues,

$$\mathcal{M}(s,z) \overset{|z|\to\infty}{\simeq} -\sum_i \left[\,(2\,\alpha_i(s)+1)\;\pi\beta(\alpha_i,s)\right] \frac{(-z)^{\alpha_i(s)}}{\sin\pi\,\alpha_i(s)}\,, \tag{C.5}$$

and the dominant contribution is given by the Regge pole with largest real part which, denoted by $\alpha(s)$, is called *Regge trajectory*. Hence the behavior of the scattering amplitude for large values of t and fixed s is

$$\mathcal{M}(s,t) \overset{t\to\infty}{\sim} -\beta(s)\,\frac{t^{\alpha(s)}}{\sin\pi\,\alpha(s)} \equiv C(s)\,t^{\alpha(s)}\,, \tag{C.6}$$

where $\beta(s)$ includes all constants and factors s-dependent which appear in Eq. (C.5), $C(s)$ indicates a factor dependent only on s. If, instead of considering the expansion of Eq. (C.1) in the s channel, we consider the partial-wave expansion in the

t-channel, we have a formula similar to previous:

$$\mathcal{M}(s,t) \overset{s\to\infty}{\sim} -\beta(t)\,\frac{s^{\alpha(t)}}{\sin\pi\,\alpha(t)} \equiv C(t)\,s^{\alpha(t)}\,. \tag{C.7}$$

The Eq. (C.7) shows that, at high energies ($s \longrightarrow \infty$), the scattering amplitude is dominated by the leading singularity in t channel in the complex plan. In the case of relativistic regime, we obtain a relation, similar to Eq. (C.7), that may be formally obtained from this by replacing

$$s^{\alpha(t)} \longrightarrow s^{\alpha(t)} + \xi(-s)^{\alpha(t)} = \left(1 + \xi e^{-\imath\,\pi\alpha(t)}\right) s^{\alpha(t)}\,, \tag{C.8}$$

which sums the s and u-channel contributions and where the *signature* ξ is a quantum number which may assume two values, $\xi = \pm 1$. Therefore in relativistic regime we have

$$\mathcal{M}(s,t) \overset{s\to\infty}{\sim} -\beta(t)\,\frac{1+\xi e^{-\imath\pi\alpha(t)}}{\sin\pi\,\alpha(t)}\,s^{\alpha(t)} = \beta(t)\,\eta(t)\,s^{\alpha(t)}\,, \tag{C.9}$$

where $\eta(t)$ is the *signature factor*. In the *Regge limit* ($s \longrightarrow \infty$ for fixed t) it is shown that, in presence of a Regge pole, the partial-wave amplitude $\mathcal{M}_\ell(s)$ behaves as

$$\mathcal{M}(\ell,t) \overset{\ell\to\alpha(t)}{\sim} \frac{\beta(t)}{\ell - \alpha(t)}\,. \tag{C.10}$$

The trajectory $\alpha(t)$ takes integer values of ℓ at some non-physical value of t (i.e., for $t > 0$) in the s-channel. These Regge poles correspond to resonances or bound states, which have angular momentum $\ell = \alpha(t)$. $\alpha(t)$ is a Regge trajectory (or *Reggeon*) interpolating such resonances (or bound states). Reggeons are often collectively denoted by the symbol $I\!R$. The s-channel asymptotic behavior of Eq. (C.9) is due to the exchange of a family of resonances in the crossed channel. Therefore the Regge intuition binds the scattering at s-large to the exchange of these families of resonances in the t-channel.

A simple way to visualize the Regge trajectories for low t is to expand a in power series around $t = 0$ and to truncate it to first terms:

$$\alpha(t) = \alpha(0) + \alpha'\,t + \ldots\,, \tag{C.11}$$

where $\alpha(0)$ and α' indicate the *intercept* and the *slope*, respectively, of the trajectory. The expansion of Eq. (C.11), which is justified only for small t, holds

actually for rather large values of t, when interpolating resonances with the same quantum numbers (other than the spin). In this context we note that we obtain the proportionality between the angular momentum and the squared mass ($m^2 = t$) of the resonance. The basic idea of Regge Theory is that sequences of hadrons of mass m_i and spin j_i lie on trajectories $\alpha(t)$ such that $\alpha(m_i^2) = j_i$. Therefore the observed hadrons lie on approximately linear trajectories which are parallel with each other, i.e. the hadrons, which have the same quantum numbers, except the spin, and different mass, lie on a same trajectory[3] $\alpha_{I\!R}(t)$.

The Regge trajectories, with the largest intercept are those corresponding to the mesons ρ, f_2, a_2 and ω, with $\alpha(0) \simeq 0.5$ (and $\alpha' \approx 1\,\mathrm{GeV}^{-2}$). The Eq. (C.9) shows that most the intercept assumes a high value and most important is its contribution to s increasing.

The trajectory, considered to explain the data of the total hadronic cross section[4] at high energies, presents the quantum numbers of vaccum, as the f_2-trajectory, but it has an intercept[5] $\alpha(0) \geq 1$. This trajectory is named *Pomeron* ($I\!P$), which does not correspond to any known particle. By analysis of data of the elastic scattering we have that the trajectory $I\!P$ is much flatter than the others ($\alpha'_{I\!P} \simeq 0.25\,\mathrm{GeV}^{-2}$).

In the Regge context, by using the optical theorem, Eq. (A.56), and starting from Eq. (C.9), we easily obtain the formula relating the total cross section due to the contribution of a single pole:

$$\sigma_{\mathrm{tot}} \overset{s\to\infty}{\simeq} \frac{1}{s}\,\mathrm{Im}\mathcal{M}(s, t=0) \overset{s\to\infty}{\sim} \beta\, s^{\alpha(0)-1}\,, \tag{C.12}$$

where we omit the signature factor for simplicity. If more than one pole contributes the total cross section is given by a sum of terms of the form of Eq. (C.12):

$$\sigma_{\mathrm{tot}} \overset{s\to\infty}{\sim} \sum_i \beta_i\, s^{\alpha_i(0)-1}\,. \tag{C.13}$$

[3]We note that, before the formulation of QCD, the strong interactions were regarded as essentially due to the exchange of complete trajectories of particles.

[4]These cross sections, as a function of s, are rather flat around $\sqrt{s} \sim 10 \div 20\,\mathrm{GeV}$ and increase at higher energies.

[5]Originally it was thought that the cross sections were asymptotically constant at high energies, therefore it was introduced a Pomeron with [16].

It is found that the experimental data of the total, elastic and differential hadronic cross sections are well described (for small $|t|$-values) if the trajectory of the Pomeron is [37]

$$\alpha_{I\!P}(t) \simeq 1.08 + 0.25\, t\,. \tag{C.14}$$

A value of $\alpha_{I\!P}(0)$ greater than 1 is in contrast to the theorem of Froissart-Martin ($\sigma_{\rm tot} \sim s^{0.08}$) but it is necessary if we want to explain the growth of $\sigma_{\rm tot}$ at high energies.

The limit Froissart-Martin could be safeguarded by the fact that at the achieved energies we might be still far from the asymptotic region of energies provided in Regge Theory; therefore the increase of energy could trigger a mechanism able to respect the imposed limit on the cross section.

In this simplified discussion of the theory of Regge, only the contributions from the Regge poles are considered, because, as we have reported in the footnote on page 87, it has been neglected the presence of possible cuts and branch points (which are usually present) in the analytical scattering amplitude. These terms could have a dampening effect on growth of $\sigma_{\rm tot}$, allowing to respect the limit of Froissart-Martin also in case where there are contributions due to Pomeron.

We not yet know in detail the connection between the Regge theory, which has a great success in describing the processes fluffy, and the QCD, more fundamental than the previous. Very likely the exchange of Pomerons primarily derives from the exchange of a state with two gluons, while the above meson trajectories (ρ, f_2, a_2 ed ω) correspond to bound states formed of the quark-antiquark [44].

Bibliography

[1] P. Collins, An Introduction to Regge Theory and High-Energy Physics, Cambridge University Press, Cambridge, 1977.

[2] V. Barone, E. Predazzi, High-Energy Particle Diffraction, Springer, 2002.

[3] J. Collins, D. Soper, G. Sterman, Nucl. Phys. B 261 (1985) 104.

[4] E. Leader, E. Predazzi, An Introduction To Gauge Theories and the "'New Physics"', Cambridge University Press, 1982.

[5] K. Goulianos, Phys. Rept. 101 (1983) 169.
S. Fazio, Misura delle sezioni d'urto $d\sigma/dQ^2$, $d\sigma/dW$ e $d\sigma/dt$ in processi diffrattivi di Deeply Virtual Compton Scattering, Tesi di Laurea, Università della Calabria (2004).

[6] M. Arneodo, M. Diehl, Diffraction for non-believers, contributo ai Proceedings of the Workshop on HERA and the LHC, DESY and CERN, 2004-2005.

[7] P. Palazzi, Diffusione di adroni da deuterio: una misura della sezione d'urto differenziale $\pi^- D \longrightarrow \pi^- D$ a 1000 MeV/c, Tesi di Laurea, Università degli Studi di Trieste (1968).

[8] ZEUS Collaboration, M. Derrick, et al., Phys. Lett. B 315 (1993) 481.

[9] ZEUS Collaboration, Phys. Lett. B 332 (1994) 228.
ZEUS Collaboration, Z. Phys. C 68 (1995) 569.
ZEUS Collaboration, Eur. Phys. J. C 1 (1998) 81.
ZEUS Collaboration, Eur. Phys. J. C 6 (1999) 43.

[10] H1 Collaboration, T. Ahmed, et al., Nucl. Phys. B 429 (1994) 477.

[11] H1 Collaboration, Phys. Lett. B 348 (1995) 681.
H1 Collaboration, Z. Phys. C 69 (1995) 27.
H1 Collaboration, Nucl. Phys. B 472 (1996) 3.
H1 Collaboration, Z. Phys. C 75 (1997) 607.

[12] H1 Collaboration, Z. Phys. C 76 (1997) 613.

[13] G. Alberi, G. Goggi, Phys. Rep. 74 (1981) 1.
K. Goulianos, Phys. Rep. 101 (1983) 169.

[14] G. Chew, S. Frautschi, Phys. Rev. Lett. 8 (1962) 41.

[15] V. Gribov, Sov. Phys. JETP 14 (1962) 478.

[16] I. Pomeranchuk, Sov. Phys. JETP 7 (1958) 499.

[17] G. Ciappetta, Modelli Teorici per la Diffusione Compton Profondamente Anelastica, Tesi di Laurea, Università della Calabria (2009).

[18] H1 Collaboration, C. Adloff, et al., Zeit. Phys. C 74 (1994) 221.

[19] J. Sakurai, Phys. Rev. Lett. 22 (1969) 981.

[20] H1 Collaboration, C. Adloff, et al., Zeit. Phys. C 76 (1997) 613.
H. Abramowicz, Diffraction and the pomeron, contributo alla 19th International Symposium on Lepton and Photon Interactions at High-Energies (LP 99), Stanford, California, 1999.
ZEUS Collaboration, S. Chekanov, et al., Eur. Phys. J. C 24 (2002) 345.

[21] G. Bruni, et al., Leading proton production in ep and pp experiments: how well do high-energy physics Monte Carlo generators reproduce the data?, contributo ai Proceedings of the Workshop on HERA and the LHC, DESY and CERN, 2004-2005.

[22] ZEUS Collaboration, S. Chekanov, et al., Eur. Phys. J. C 38 (2004) 43.

[23] S. Fazio, Exclusive Diffraction at HERA and Beyond, contributo ai School-Seminar Proceedings, Gomel, 2009.

[24] ZEUS Collaboration, S. Chekanov, et al., Phys. Lett. B 573 (2003) 46.

[25] H1 Collaboration, A. Aktas, et al., Eur. Phys. J. C 44 (2005) 1.

[26] H1 Collaboration, F. Aaron, et al., Phys. Lett. B 659 (2008) 796.

[27] ZEUS Collaboration, S. Chekanov, et al., JHEP05 (2009) 108.

[28] H1 Collaboration, F. Aaron, et al., Phys. Lett. B 681 (2009) 391.

[29] V. Guzey, M. V. Polyakov, Eur. Phys. J. C 46 (2006) 151.

[30] John R. Taylor, An Introduction to Error Analysis, 2nd edition, Sausalito, California, University Science Books, 1997.

[31] G. Ciappetta, Results in Physics 4 (2014) 75–78.

[32] OriginLab Corporation, Northampton, MA 01060, USA.
URL `http://originlab.com/`

[33] H1 Collaboration, C. Adloff, et al., Eur. Phys. J. C 13 (2000) 371.

[34] GnuPlot Version 4.4
URL `http://gnuplot.info/`

[35] P. Newman, Int. J. Mod. Phys. A 19 (2004) 1061.

[36] J. R. Cudell, K. Kang, S. Kim, Phys. Lett. B 395(1997) 311.

[37] A. Donnachie, P. Landshoff, Nucl. Phys. B 231 (1984) 189.

[38] Mathematica Wolfram Research
URL `http://www.wolfram.com/`

[39] E. Aschenauer, Current GPD Results and Future Prospects, BNL Event: RHIC & AGS Annual Users' Meeting, 2010.

[40] M. Froissart, Phys. Rev. 123 (1961) 1053.
A. Martin, Phys. Rev. 129 (1963) 1432.
M. Martin, F. Cheung, Analyticity properties and bounds of the scattering amplitudes, Gordon and Breach Science Publisher, 1970.

[41] G. Grunberg, T. Truong, Phys. Rev. Lett. 31 (1973) 63.

[42] B. Povh, K. Rith, C. Scholz, F. Zetsche, Particles and Nuclei, Springer, 4rd Ed., 2003.

[43] T. Regge, Nuovo Cimento 14 (1959) 951.
T. Regge, Nuovo Cimento 18 (1960) 947.
P. Collins, Phys. Rep. C 4 (1971) 103.

[44] M. Wusthoff, A. D. Martin, J. Phys. G 25 (1999) R309

Acknowledgements

I would like to express my deep gratitude to Professor Roberto Fiore, my research supervisor, for many reasons. The main one is for introducing me to the study of the DVCS processes. I am grateful to him because he continually encouraged me to do more and better; in this manner I was able to find again the physicist that the dark years of my life almost irretrievably had deleted from my memory.

I would also like to thank Professor Alessandro Papa for being always available to discuss the most diverse topics in which it was requested his support and for giving me the opportunity to 'get my hands in the dough', as it was proposed during the exam-talk of access to the PhD course in 'Physics and Quantum Technologies', University of Calabria.

I would also like to extend my thanks to complete staff of the Department of Physics, University of Calabria, for its friendly hospitality during the months of the PhD course.

My grateful thanks are also extended to Dr. Petra Stoeber, Dr. Gaetano Nicastro and Dr. Valentino Pingitore for their help in preparation of the present manuscript and to Dr. Ivano Selvaggi for his assistance, especially during the last period.

I wish to thank my family for their support and encouragement throughout my study.

I would like to express my deep gratitude to my parents. I thank my father, $\mathcal{P}ietro$, for the example given. In the black periods that characterized his life, he pursued the streets of happiness that have conducted him until my mother, who has always sacrificed herself for her children and husband. I thank my mother, $\mathcal{O}lga$, for the example given. She has always supported me and encouraged me to go ahead, to trust that even after the darkest night the sun rises and warms

us again.

I thank my wife, Carmen, because she is my lifeline and taught me to believe in my abilities. I thank her for having recovered the man who is writing the present and made him regain some of his lost certainties. For all this and much more, there are no words to express my love for her.